IMPROVING ELECTRON BEAM INDUCED CURRENT ANALYSIS OF CDTE DEVICES THROUGH PRINCIPAL COMPONENT ANALYSIS

by

Sean Michael Jones

A thesis submitted to the Faculty and the Board of Trustees of the Colorado School of Mines in partial fulfillment of the requirements for the degree of Doctor of Philosophy (Material Science).

Golden, Colorado

Date _____

Signed: _____

Sean Michael Jones

Signed: _____

Dr. Brian Gorman
Thesis Advisor

Golden, Colorado

Date _____

Signed: _____

Dr. Ivar Reimanis
Department Head Title
Department of Metallurgical and Materials Engineering

ABSTRACT

The development of modern photovoltaic devices requires the ability to correlate uncontrolled micro-structure growth with changes in the electronic properties of the device. While Electron Beam Induced Current (EBIC) characterization should be well positioned to lead this analysis, its interpretation has proven difficult in thin film devices.

In this document, we present improvements to two methods reducing interpretation ambiguity in EBIC analysis. First we demonstrate voltage-biased EBIC on a low short-circuit current device. Device choice allowed us to obtain high resolution voltage dependent collection maps. We combine these collection maps with simulation and principal component analysis to experimentally demonstrate low correlation between short circuit collection and voltage response as well as a method for identifying regions with similar voltage responses.

Next we demonstrate variable beam-current injection dependent EBIC. We expanded on the single study that had previously demonstrated this technique, combining it with principal component analysis. From this we developed the ability to differentiate regions of similar collection efficiency so as to identify barriers to collection.

This dissertation serves to demonstrate how much additional information can be obtained through the variation of imaging conditions. Through the combination of variable imaging conditions and principal component analysis, we are able to decrease characterization ambiguity with no additional investment for the tool owner. We are able to two forms of lateral grain boundaries in CdTe devices. These techniques are able to definitively show the role grain boundaries play in short circuit collection efficiencies.

TABLE OF CONTENTS

ABSTRACT iii

LIST OF FIGURES vi

LIST OF TABLES xi

ACKNOWLEDGMENTS xii

CHAPTER 1 INTRODUCTION 1

CHAPTER 2 EXPERIMENTAL SETUP 7

CHAPTER 3 EBIC FORMALISM 15

3.1 Initial Collection Function 15

3.2 Establishing Boundary Conditions 16

3.3 Relaxing Low Injection Assumptions 16

3.4 Relaxing Short Circuit Assumptions to allow for Voltage Bias 17

CHAPTER 4 APPLICATION OF PCA TO SIMULATED COLLECTION FUNCTIONS 19

4.1 Applications to an Idealized 1D simulation 19

4.2 Applications to a 1D simulation containing a grain boundary 24

CHAPTER 5 EXPERIMENTAL RESULTS SMALL AREA DEVICE VOLTAGE SERIES 31

5.1 Applications of voltage bias to Small Area Devices 31

5.2 Effects of Beam Damage 35

CHAPTER 6 LINE PROFILE INJECTION DEPENDENCE 38

6.1 Introduction 38

6.2 Accelerating Voltage Variation 38

6.3 Beam Current Variation 40

6.4 Injection Dependent Line Profile Evolution 41

6.5 Results 43

6.6 Conclusion 45

CHAPTER 7 2D PCA-ENHANCED EBIC ANALYSIS CDSE/CDTE 46

7.1 Introduction . . . 46
7.2 CdSe/CdTe device . . . 46
7.3 Conclusion . . . 53
CHAPTER 8 2D PCA-ENHANCED ANALYSIS OF BILAYER CDSETE DEVICES . . . 54
8.1 Introduction . . . 54
8.2 Experiment . . . 55
8.3 Conclusion . . . 59
CHAPTER 9 CONCLUSION . . . 62
REFERENCES . . . 64
APPENDIX A PRINCIPAL COMPONENT ANALYSIS . . . 71
A.1 Application of PCA to Images . . . 71
APPENDIX B MODEL DETAILS . . . 73
APPENDIX C SESAME 1D IDEALIZED SIMULATION-PYTHON . . . 74
C.1 Sesame 1D Lateral Grain Boundary Simulation-Python . . . 78
C.2 Matlab Import Code . . . 82
C.3 Matlab Analysis Code . . . 84

LIST OF FIGURES

Figure 1.1 Literature example of APT decomposition of a grain boundary. The analysis shows Chlorine aggregation at a grain boundary as well as at the interface between CdTe and CdS layers. Chlorine is added to CdTe solutions to passivate grain boundaries. 3

Figure 1.2 Cross Section EBIC collection maps of a MZO/CdTe device (left) and MZO/CdSeTe/CdTe device (right). Images show both the 2D Collection Map as well as an overlayed collection profile. Under normal device operation, light passes through the glass superstrate before reaching the absorber. Because light intensity decays exponentially with respect to distance travelled through a medium, high collection efficiency near the glass superstrate results in greater short circuit current. Increasing the selenium content near the front contact was expected to create a band-gap gradient through the device and increase the collection efficiency. The abrupt transition in collection efficiency seen in the collection maps demonstrate that microstructure plays a key role in reducing the collection efficiency near the front contact. 4

Figure 1.3 This figure shows an overview of possible measurements which can be obtained using an electron beam incident on a photovoltaic sample. Each measured process requires an additional detector. In this publication, Figure Credit: ephemeron labs inc. 5

Figure 2.1 NREL 7600 imaging setup. Each monitor is applied to an independent computer. The ammeter allows for beam current measurements. The function generator, lock-in amplifier and beam blanker are used for traditional voltage-bias EBIC measurements. The source meter can be used for 4 probe voltage bias measurements as well as in-situ J-V measurements. The operational amplifier is used for standard EBIC imaging. The low-pass filter is used to reduce high frequency electronic noise in the EBIC imaging acquisition. 7

Figure 2.2 NREL EBIC setup during standard EBIC acquisition. Each monitor is connected to an independent computer. The SEM computer is used for standard SEM functions including imaging alignment. The EBIC monitor uses mightyEBIC software for simultaneous SEM and EBIC image acquisition. The CL monitor has its own independent software for only CL acquisition. 8

Figure 2.3 Configuration used for mechanically polishing cross section samples 9

Figure 2.4 An extreme case of in situ Ion Mill results. The ion shield acts as a sacrificial layer to prevent damage to the sample. The milled region is a roughly gaussian distribution caused both by the sputtered ion trajectories as well as the sample rocking procedure which reduces mill curtaining effects. 10

Figure 2.5 Ion Mill Through Non-Uniform Back Contact demonstrates the non-uniform milling, or curtaining of the cross-section surface. These effects can result in non-uniform generation, which in cause artifacts in the EBIC collection map. 10

Figure 2.6 Ion Mill Electrode during cleaning. Metallic shards from the ion shields are attracted to the electric field of the electrode. The electrode operates with an electrode shield in place, however should a metallic shard fall between the electrode shield and electrode, it can short the electrode and stop the milling procedure. An example of such an arrangement is seen in the picture 11

Figure 2.7 Experimental Apparatus of Mechanical EBIC Probe Configuration. This is a 3D rendered reconstruction of the apparatus created highlight features of the custom built apparatus. While 4-probe acquisition is possible with this construction, we used 3 probes for the majority of our acquisitions. 3 probes allow for a standard 2-probe EBIC acquisition which completes the photovoltaic circuit while also allowing in-situ beam current measurements without changing imaging conditions. 12

Figure 2.8 Alternate angle of Experimental Apparatus. False colors are used to accentuate the polished region of the sample because the dimensions of the polished regions are so small as to be difficult to see for most samples. The sample is mechanically fastened to the isolated stage using carbon tape. All probes were isolated from the stage with plastic screws and washers while a spring and plastic screw provided a vertical degree of freedom. The use of springs in this way increases the force tolerance of the application of a probe to the sample without causing mechanical damage and potentially shorting the device. 13

Figure 2.9 An image of the designed EBIC mount being used in the the SEM imaging chamber . . . 14

Figure 4.1 A 3D plot of the collection rate using generation position and applied bias as independent variables. A standard EBIC collection map contains the data of the black line while injection dependent or spectral photocurrent measurements integrate along the generation position, weighted by intensity, and plot this integrated photocurrent against the applied bias. Regions near the 0um position which demonstrate relatively uniform collection are frequently referred to as the depletion region, in which free charge carriers are removed by a strong electric field. 20

Figure 4.2 JV response of each pixel in the device. This plot is analogous to a 2D view of figure 4.2. Systematically increasing shunt resistance is due to increased minority recombination probability with increased distance from the front contact. 21

Figure 4.3 A comparison of the spatial and voltage functions of the first two modes. Regions of the spatial function with high amplitude are strongly influenced by the voltage function of the same mode. 22

Figure 4.4 First results are grouped based on trends in correlation of the first two eigenvector values. Then these groups are superimposed on a zero bias collection bias. Then we weight the sum of the voltage function by the average collection function value for each region to create a decomposed voltage response. Note that since we primarily care about changes to voltage response with respect to the collected current at $V_A = 0$, we use that value to center our results, which is why all voltage responses intersect at the origin. The black functions in each plot represent all results regardless of region. 23

Figure 4.5 A 3D plot of the collection rate using generation position and applied bias as independent variables. A standard EBIC collection map contains the data of the black line while injection dependent or spectral photocurrent measurements integrate in the generation position while and plot along photocurrent against the applied bias. Region 1, which exists between x=0 and 1, demonstrates non-linear collection behavior. 24

Figure 4.6 JV response of 100 representative pixels in the simulation. This demonstrates systematic changes which are more difficult to identify than those of figure 4.2. 25

Figure 4.7 Here we demonstrate using PCA correlations to further subdivide results based on electrical properties rather than position with respect to the grain boundary. This is a corrolary to Figure 4.4 and shows non-ideal collection profiles. 26

Figure 4.8 Decomposed JV response of 100 representative pixels. The 5 regions each contain non-linearities which evolve systematically, as compared to the structural decomposition of figure 4.6 . . . 27

Figure 4.9 A plot of the electric field strength in the grain boundary. This plot shows two regions of strong electric field pointing in the same direction while the electric field at the grain boundary has low strength and may point in the opposite direction . . . 28

Figure 4.10 A plot of the electric field strength in the grain boundary. Positive biases contain an electric field acting against the two fields in figure 4.12, while negative biases contain a field in the same direction. . . . 29

Figure 4.11 A comparison of the carrier currents near the JV inflection point of region 1. This diagram demonstrates a homojunction who's position shifts with bias within this region. At more positive biases, region 1 is primarily p-type while at more negative biases, region 1 is primarily n-type. Because the grain boundary acts as a strong collection barrier, region 1 behaves as an npn transistor while region 2 behaves more like a diode. The process of scanning region 1 with an electron beam is comparable to applying a voltage to the transistor gate, which changes the voltage response of this region during imaging. . . . 29

Figure 4.12 Three equivalent circuit diagrams which would result in the npnp divisions as well as the JV response observed in this simulation. The three diode model provides an accurate model for a photovoltaic device. The diode-transistor model best expresses the non-idealities of the device while allowing for injection from generation based characterization. The thyristor model provides the most abbreviated equivalent circuit model while allowing for mid-absorber generation . . . 30

Figure 5.1 Correlated Eigenvectors with 6 regions identified. Pixels which fall within correlation value of 1e-4 of a line are considered part of that group. These groups do not contain all pixels, but were chosen to highlight systematic trends in the changes in collection. . . . 32

Figure 5.2 A comparison of the 0V CdTe J-EBIC collection map and secondary electron image with each of the 6 groups spatially correlated. The spatially correlated groups demonstrate some grid-like visual artifacts which are not indicative of systematically omitted results. . . . 33

Figure 5.3 This violin plot shows the frequency of correlation between each of the six identified regions and the injection normalized collection seen in figure 5.2a. The width variation of each data set is reflective of a smoothed histogram with increased width corresponding with increased frequency of occurrence. . . . 34

Figure 5.4 Average JV response characteristics of all 6 regions of the collection map. The y values are the inverted coefficient of the exponential voltage coefficient. These values are proportional to the ideality factor, n. . . . 35

Figure 5.5 JV response of each of the 6 regions. The regions of the left plot show a systematic change to ideality. The regions in the right plot showed greatly increased shunt resistance in figure 5.4. . . . 36

Figure 5.6 Effect of beam damage on unbiased collection efficiencies for each pre-defined region. The left plot shows the average collected values while the right plot shows the net change in each region. . . . 37

Figure 6.1 Simulated carrier scattering in CdTe as a function of beam voltage. Each line represents the lateral resolution of a given beam current through the cumulative radial energy deposition. Simulations were conducted using CASINO with 1 million simulated electron trajectories per beam setting and with the electrons interacting with a uniform CdTe volume 39

Figure 6.2 A demonstration of the decrease in lateral image resolution as a function of beam voltage. While there are changes to the average line profile seen in the left of both images, changes in lateral resolution cannot be isolated from changes in injection conditions. 39

Figure 6.3 Evolution of injection dependent EBIC compared with the KPFM electric field measurements. EBIC measurements were taken with a 5kV beam voltage while KPFM measurements were taken with a sample bias of -1.5V. The peak collection position demonstrates changes consistent with imaging under high injection conditions. Under these conditions, we expect that reductions in beam current would lead the peak collection to asymptotically approach the peak field position. 42

Figure 6.4 Line Profile Evolution of average collection with respect to beam current. This evolution shows an increase in collection efficiency as well as a shift in maximum electron collection as beam current is reduced. The x-axis origin is the start of the CdTe layer, as determined by the secondary electron image. 43

Figure 6.5 Collection peak position evolution as a function of beam current. Based on the assumption of previous publications, we expect the peak to asymptotically approach the back contact with increases to the beam current. 44

Figure 7.1 Secondary electron image of the region of interest 47

Figure 7.2 EBIC Collection Map of the Region of interest. 47

Figure 7.3 Evolution of average collection vs position from the junction as a function of injection. Decreased collection efficiency is expected as the internal fields are screened, however this sample does not show the same shifting maximum collection position as we saw in chapter 6. 48

Figure 7.4 Eigenvectors, $F(x_b)$, and coefficients, $G(I_b)$, for the first 4 modes of change in the injection series. This shows strong contrast near the grain boundary which is visible in the secondary electron image of figure 7.1. The first mode shows average change in collection across the device while other modes show deviations to this change. 49

Figure 7.5 Three regions identified from changes in collection contrast with respect to injection. These regions are superimposed on a density map correlating the first two eigenimages. Intensity is placed on a logarithmic scale. 50

Figure 7.6 The spatial positions of 3 PCA-identified regions overlayed onto the EBIC collection map seen in Figure 7.2. These regions are spatially isolated which supports the selection criteria of Figure 7.5. 50

Figure 7.7 Average collection efficiency in each region as a function of beam current. From this, we can see large variation in the collection in region 3, lower collection variation in region 2, and no discern-able change in collection for region 1. Region 1 appears to represent pixels where the electron beam was not in contact with the absorber, which acts as a proof of the null hypothesis. Region 1 appears near the low beam current collection peak and is presumed to be at or near the junction. Most of the pixels representing region 2 are deep in the absorber and appear to be strongly influenced by the presence of a grain boundary. There is also a population of pixels in region 2 which appear beneath pixels of region 1 and may indicate a barrier to collection near the front contact. . 51

Figure 7.8 This process uses higher order eigenvectors to identify populations which exhibit similar responses to varying injection. (a) shows the spatial location of each pixel which was found through the eigenvector correlation plot seen in (b). The response of each population to varied beam current is then shown in figure (c) with 1 σ bars included. Five regions were identified using correlations between eigenvector 3 and 4. These five regions were contrasted with the previously defined region 1 from figure 7.6. . . 52

Figure 8.1 Line profile evolution of $CdSe_xTe_{1-x}$ as a function of Se content. Data was collected at 5kV beam voltage with beam currents of 0.43 ± 0.03 nA. 54

Figure 8.2 Effect of Se content on EBIC contrast for devices with the illustrated bilayer structure. The five samples contain 0 (a), 10 (b), 20 (c), 30 (d), and 40(e) percent selenium in each image. Images were collected with electron beam currents of 0.43 ± 0.03 nA and accelerating voltages of 5kV 55

Figure 8.3 Comparison of the Secondary Electron (a), EBIC (b), and PCA identified region representations (c) of the region of interest. This demonstrates a region of interest with some curtaining, an atypical collection map with microstructure dependencies, and two identified regions of pixels obtained using PCA. 56

Figure 8.4 Differentiating factors of the first two regions. The regions were first identified using the density map in (a). From there we can show their change in collection as a function of beam current (b) which can be further divided into a difference in average collection across all beam currents (c), and the deviations with respect to that average threshold (d). 1 standard deviation error bars are included in figures b-d. 57

Figure 8.5 Comparison of the Secondary Electron (a), EBIC (b), and PCA identified regional representations (c) of the region of interest. 58

Figure 8.6 Deconstruction of 5 identified regions using the modified PCA procedure. The regions were identified through high density regions outlined in the eigenvector correlation density map of (a). From there we show their change in collection as a function of beam current (b) which can be further divided into a difference in average collection across all beam currents (c), and the deviations with respect to that average threshold (d). 1 standard deviation error bars are included in figures b-d. 59

Figure 8.7 Correlation between STEM-EDS measurements. From this, we see strong correlation between the EBIC peak-position and the EDS selenium gradient. 60

Figure B.1 Model Property Summary Page 73

LIST OF TABLES

Table 3.1 Variable Definition Table 15

ACKNOWLEDGMENTS

I would like to thank and acknowledge Brian Gorman for his extensive advising, I'd like to thank Harvey Guthrey, John Moseley, Mowafak Al-jassim for their constant support in both experiment and simulation work. I'd like to thank CS Jiang for his insight into KPFM and the experimental results. I would also like to thank Lincoln Carr for my introduction to PCA. Finally I'd like to thank my wife and family for their evergreen support and encouragement.

CHAPTER 1

INTRODUCTION

Characterization is a key part of photovoltaic development. Most photovoltaic devices are iteratively developed with characterization informing how processing changes impact a device's structure and performance. In this way, characterization aims to allow for manufacturers to understand how and why changes in the manufacturing process affect the end product. Unfortunately characterization of devices which have complex materials and properties can be slow and costly. Cost-effective photovoltaic devices have complex 3 dimensional micro-structures which include grain boundaries, multiple dopant types, and composition gradients in conjunction with the standard p-n junction of a diode [1–7]. The number of variables during production which affect these complex structures have led to multivariate growth processes. These growth processes quickly outpace traditional characterization processes. If the traditional iterative development process is to continue for photovoltaic devices, characterization techniques must be improved to allow for the greater interpret-ability of stand-alone processes.

Photovoltaic thin film devices, specifically CdTe, have left traditional characterization at a loss. These devices demonstrate collection which is strongly affected by microstructure but also have increased their growth complexity through the introduction of additional features such as electron reflector layers near back contacts [5] and band gap gradients produced by multiple absorber materials deposited sequentially [3, 4, 8, 9]. For example, Selenium has been shown to passivate bulk defects and lower the band gap of CdTe from 1.5 to 1.4eV[4, 8]. Selenium can either be introduced through the deposition of a thin CdSe layer[8] or through the deposition of a thicker CdSeTe alloyed layer between the n-type window layer and the more traditional p-type CdTe absorber[3]. In either device structure, the gradient is subsequently smoothed through diffusion of Selenium into the pure CdTe layer upon annealing. The introduction of Selenium to CdTe devices has provided a path for continued device improvement, but it has also lead to an explosive increase in the number of variables to be optimized in the course of device development. This is because this process introduces another anneal step, it changes grain equilibrium size[10], and it it believed to vary the diffusion of both dopants and grain boundary passivation treatment [1].The increased growth parameter complexity requires more detailed characterization to identify growth parameter dependencies and optimize device performance. In evaluating the ability for characterization techniques to aid in growth optimization, we will first address commonly used techniques and their limitations before we move to discuss how these techniques may be changed.

The first group of characterization techniques are those which quickly categorize performance in a non-destructive manner. These techniques largely provide performance information but fail to provide the mechanisms for changes which frequently comes from structural data. Examples of these techniques include the Current-Voltage (JV)[11, 12], Capacitive-Voltage (CV) [12], and Time Resolved Photo-Luminescence (TRPL) [4, 12–16] characterization. Each of these techniques provide key information for average device properties and allows for better comparison of similar devices. JV measurements can provide key performance information including max-power points, short-circuit currents, and device ideality. CV provides information pertaining to carrier concentration and active dopants. TRPL provides valuable information pertaining to carrier lifetimes with some lateral spatial resolution. The greatest advantage of these techniques is that they are non-destructive and require relatively little sample preparation which allows for high throughput. These characterization results have proven vital in understanding devices with small microstructure-induced collection variability [12, 17]. However the characterization of thin film devices requires the specificity gained from correlating variations in performance with micro-structure. For example, a recent study of CdSeTe-CdTe devices indicated that a meta-stable roll-over effect which may have otherwise been attributed to the formation of a schottky barrier at the back contact was instead caused by a charged front contact barrier and a buried junction [7].

Previous studies have demonstrated that a thin resistive layer placed near the front contact of a device may result in a "roll-over" effect in which the JV response demonstrates two inflection points [18]. This shows that the increased barrier resulted in an increased roll-over effect at high forward biases. In CdTe, similar roll-over effects have been attributed to a schottky barrier forming between at the back contact [12, 19], a collection barrier forming at the front contact [18], a buried junction in the absorber [7], and crystallographic phase change in some grains of the p-type absorber layer[20]. These material problems all result in similar JV non-linearities yet require different production changes in order to mitigate them. Therefore characterization methods which do not resolve spatial non-uniformities suffer from ambiguous interpretations and frequently require more in-depth characterization to understand.

There are also photovoltaic characterization methods such as Transmission Electron Microscopy(TEM) [20, 21], Scanning Probe techniques [7, 22], Atom Probe Tomography (APT) and Mass Spectrometry processes [10, 21, 23], which can provide local structural information but not performance information. TEM can provide high resolution structural information, Mass spectrometry techniques provide composition information, and APT provides both types of information in a much smaller area. Figure 1.1 shows the diffusion of chlorine through planar defects as was measured through correlated APT [10]. $CdCl_2$ is frequently used to passivate grain boundaries [24]. APT that under certain conditions, Chlorine can diffuse through CdTe grain boundaries into the boundary between CdTe and CdS layers. This

information is interesting, the APT study analyzes less than 4e-16cm^{-3} of the sample [25]. This limited size decreases the statistical relevance of the results unless multiple grain boundaries are similarly analyzed. Therefore the technique struggles to provide statistical information on the behavior of grain boundaries in the cell. Each of these techniques also requires cross-correlation with another technique in order to relate the measured structure and composition to device performance.

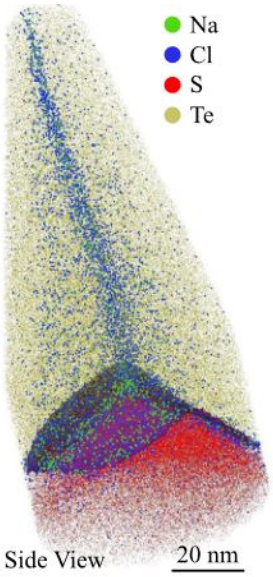

Figure 1.1 Literature example of APT decomposition of a grain boundary. The analysis shows Chlorine aggregation at a grain boundary as well as at the interface between CdTe and CdS layers. Chlorine is added to CdTe solutions to passivate grain boundaries. [10]

Scanning probe techniques can provide local electrical properties such as potential, through Kelvin Probe Force Microscopy (KPFM) [26] or carrier concentration through Scanning Capacitive Microscopy (SCM) [27]. KPFM measures local work function while SCM measures local sample capacitance. Both techniques must use their probes also for Atomic Force Microscopy (AFM) measurements of the region in order to partially deconvolve surface roughness from electrical measurements, but the AFM measurements requires surface passivation [28]. Because of this, sample preparation typically involves a low temperature (250 C) anneal [7, 28]. This process creates an oxide layer on the imaging surface, but it may also encourage dopant migration. These concerns are exacerbated by changes in dopant diffusivity caused by selenium concentration in CdSeTe devices[1]. This selenium-dependent diffusivity in the presence of a selenium concentration gradient non-uniformly affects the composition of the sample.

Finally there is a class of characterization techniques which provide information of both the microstructure and electrical properties of the device. These techniques include Electron Beam Induced Current (EBIC) [29] and Cathodoluminescence (CL) [30, 31]. These techniques use a Scanning Electron

Microscope (SEM) to locally characterize electrical properties of photovoltaic devices and do not require imaging surface passivation. Because these processes require the use of an SEM, they can simultaneously obtain the microstructural information traditionally obtained through either Secondary or Backscatter electron imaging. On top of this, these characterization techniques allow for a much greater sample size than most other microstructure characterization techniques, providing greater statistical information with regard to the performance of a given device. This allows for a faster turnaround with more statistically robust sample sizes. Both processes require a modified scanning electron microscope, which is cheaper in both acquisition and maintenance than many of the other listed techniques. In fact, these EBIC and CL are complementary techniques as they both provide insight into recombination and collection processes in photovoltaic devices and may be collected simultaneously [32].

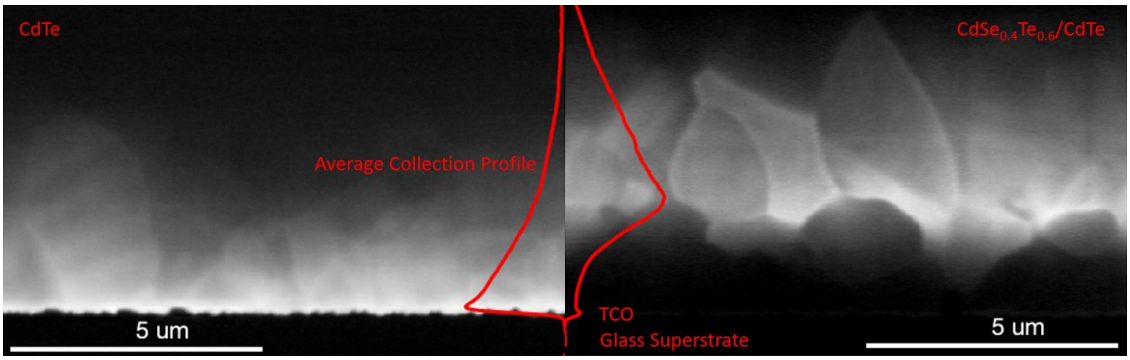

Figure 1.2 Cross Section EBIC collection maps of a MZO/CdTe device (left) and MZO/CdSeTe/CdTe device (right). Images show both the 2D Collection Map as well as an overlayed collection profile. Under normal device operation, light passes through the glass superstrate before reaching the absorber. Because light intensity decays exponentially with respect to distance travelled through a medium, high collection efficiency near the glass superstrate results in greater short circuit current. Increasing the selenium content near the front contact was expected to create a band-gap gradient through the device and increase the collection efficiency. The abrupt transition in collection efficiency seen in the collection maps demonstrate that microstructure plays a key role in reducing the collection efficiency near the front contact.

Cathodoluminescence measures the radiative recombination of a device from a given generation position. It also benefits from wavelength sensitive detectors, allowing for estimates of both the probability of radiative recombination as well as regional defect energy levels. EBIC provides the probability of collecting carriers given a population of generated carrierss centered around a rastering beam position. EBIC can also provide defect energy levels through the variation of temperature during image acquisition [33], however this is both costly and requires imaging the device outside of its normal operating conditions. Because EBIC provides only current collection rates within a device, its use and applicability have not progressed at the same rate as CL in the past two decades. Should EBIC continue to be a relevant technique, it is necessary to increase the amount of useful information gathered with this technique.

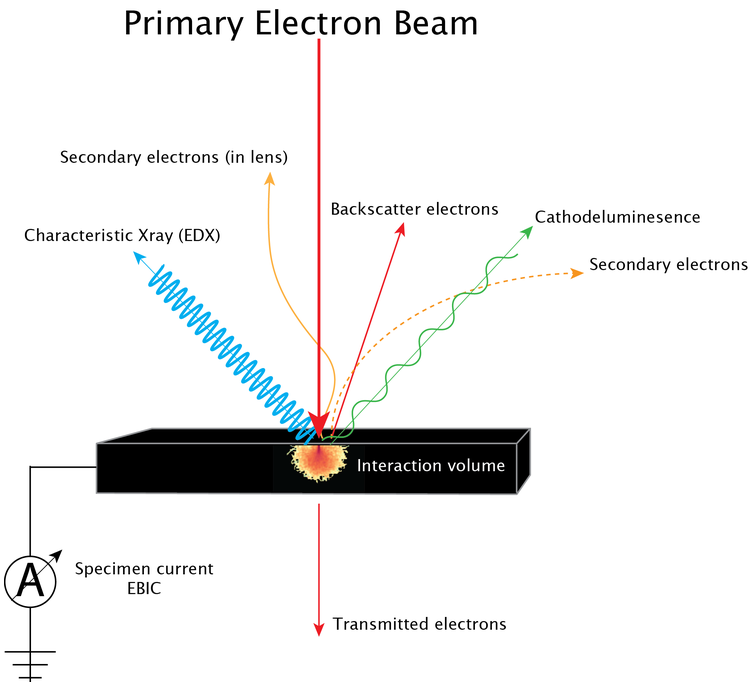

Figure 1.3 This figure shows an overview of possible measurements which can be obtained using an electron beam incident on a photovoltaic sample. Each measured process requires an additional detector. In this publication, Figure Credit: ephemeron labs inc.

The low amount of relevant information obtained during standard EBIC acquisition results in the interpretation ambiguity[34]. For example, increased collection rates have been observed while generation is focused on a grain boundary [34, 35]. This has led to a debate as to whether or not charged grain boundaries are beneficial to device performance. One interpretation of these results is that the charged grain boundaries separate carriers, resulting in conduction pathways with low recombination rates[35]. An alternative interpretation is that when carriers are generated on grain boundaries, they screen the fields which typically act as barriers to collection which would also produce the observed results[36, 37]. In this way, EBIC has failed to identify the structural information which results in these specific electrical properties.

One collection of methods to gain more information from EBIC images is Junction-EBIC (J-EBIC) [38, 39]. These processes vary imaging conditions while collecting EBIC collection maps of a photovoltaic device under cross-section orientation. Previous imaging variables used for J-EBIC have included heating the sample, cooling the sample, varying beam current, varying beam voltage, and applying a voltage bias across the contacts of the device[40]. Varying temperature is one method to change the fermi energy level and in doing so identify defects and estimate their energy level [41]. This is a well established technique which has been extensively used to identify dislocations in Silicon devices, but it is comparatively slow and

costly. Varying beam voltage is a method used to identify injection dependence and surface recombination velocity but as we will discuss in later chapters, it is difficult to quantify results. Variable beam current imaging is a technique which may identify local series resistances, however it requires multiple images at relatively high beam currents, which may create damage the sample through defect formation. Finally voltage biased EBIC is a process which has been written about extensively over the past decade.

One down side to voltage biased EBIC characterization comes from from the sheer amount of information obtained. For each pixel on an EBIC image, a full JV curve is obtained. One paper highlighted 6 pixels for cross section voltage-Biased EBIC despite a standard image containing 1e5-1e7 pixels[42]. Another process to make this information tractable is by examining line profiles across the device[43]. This process is more simple to understand under certain conditions, but still fails to represent the role microstructure plays on variation in collection.

Another method of increasing the amount of useful EBIC information acquired is through measuring collection while varying generation rates through changes to either the accelerating voltage or current of the incident electron beam. The process of systematically screening internal electric fields and then measuring the corresponding change in collection can allow for a greater understanding of the internal fields of a photovoltaic device [44, 45]. This process is much less established, but it does not suffer from the same drawbacks as voltage-biased EBIC.

Both EBIC techniques have the drawback of requiring multiple electron beam scans of the same region of interest, which can cause electron beam damage [46]. This damage may be mitigated by using low electron beam energies and fast acquisition time. Electron beam damage may be quantified through imaging under the same conditions multiple times during the acquisition of a data set.

In this dissertation, we explore methods of gathering additional information by comparing multiple EBIC images collected with different imaging conditions through Principal Component Analysis. This process allows for the systematic identification of distinct populations in a polycrystalline device while also providing statistical representation of how each population reacts to the imaging conditions. Varied imaging conditions include both the application of a voltage across the photovoltaic device during the imaging process and a change in the electron beam current.

CHAPTER 2

EXPERIMENTAL SETUP

EBIC imaging requires a completed circuit which includes a current measurement device, sample, and electron microscope. Our measurement device was a mightyEBIC scan controller and acquisition system. This system was created by ephemeron labs and we used model numbers 001 and 002 at NREL with software versions 2.0. This system enables the acquisition of both EBIC and standard SEM images, such as Secondary Electron or Backscatter electron, simultaneously. It correlates the multiple images acquired simultaneously. Software version 2.0, released in 2019, allows the scan controller to also create a DC voltage bias which simplified voltage bias studies.

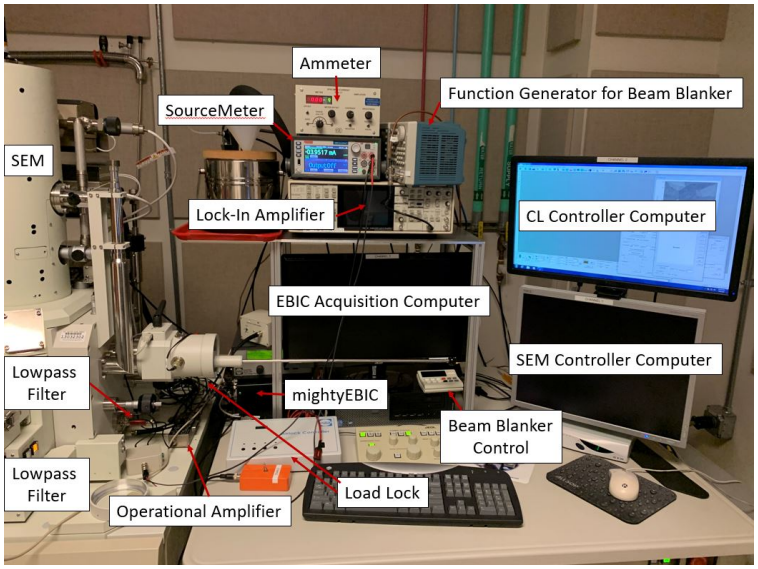

Figure 2.1 NREL 7600 imaging setup. Each monitor is applied to an independent computer. The ammeter allows for beam current measurements. The function generator, lock-in amplifier and beam blanker are used for traditional voltage-bias EBIC measurements. The source meter can be used for 4 probe voltage bias measurements as well as in-situ J-V measurements. The operational amplifier is used for standard EBIC imaging. The low-pass filter is used to reduce high frequency electronic noise in the EBIC imaging acquisition.

This mightyEBIC system was used in conjunction with a modified JEOL 7600 Scanning Electron Microscope and an operational amplifier. The microscope was modified to have metal feed throughs which allowed the transmission of 4 signals from the inside. An illustration of the experimental system is shown in Figures 2.1 and 2.2. These images demonstrates the complexity which may come from such studies. Standard EBIC imaging requires the SEM, operational amplifier, the mightyEBIC system, the EBIC acquisition computer, and the SEM controller computer. Standard voltage-dependent EBIC requires all

standard EBIC equipment as well as the beam blanker, function generator, lock-in amplifier, source meter, and a basic transformer. Small-area voltage bias EBIC requires standard EBIC equipment as well as either a source meter or an updated mightyEBIC system, and it benefits from a MHz low pass filter to reduce electronic noise in low-signal images. Injection dependent EBIC measurements require the equipment for the standard EBIC as well as an ammeter. Each of these studies may be conducted in conjunction with the attached CL system.

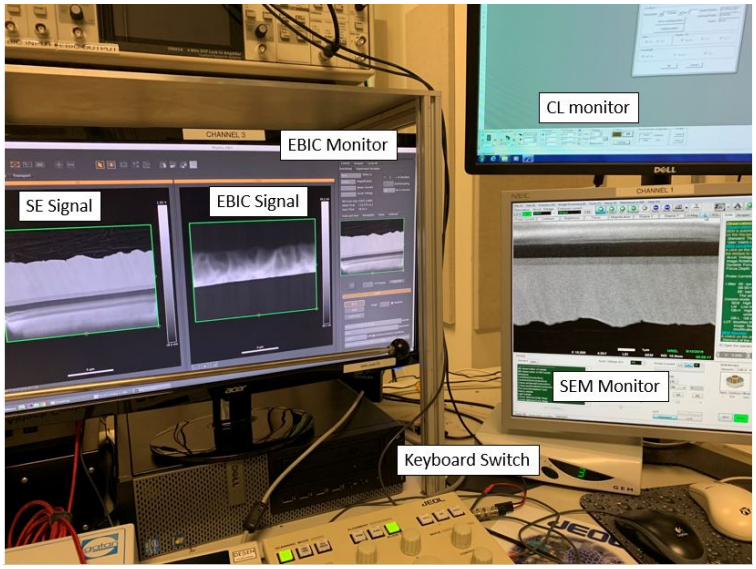

Figure 2.2 NREL EBIC setup during standard EBIC acquisition. Each monitor is connected to an independent computer. The SEM computer is used for standard SEM functions including imaging alignment. The EBIC monitor uses mightyEBIC software for simultaneous SEM and EBIC image acquisition. The CL monitor has its own independent software for only CL acquisition.

Because the project focused on the characterization of CdTe from a cross-section orientation, the optimization of sample preparation techniques was a key focus. The first step was to cleave the sample after scoring the substrate with a diamond scribe. We found that a rotating scribe worked best as the applied force was normal to the surface and thus did not encourage lateral crack propagation as much as a fixed diamond scribe. Post-scoring, a standard force applicator was used to apply a 'downward' force on either side of the score and an 'upward' force at the location of the score.

Due to the amorphous structure of the glass substrate, mechanical cleaving results in a rough cross-section imaging surface[38, 47, 48]. This is unfortunate, as cross-section EBIC requires a smooth result in order to approximate uniform generation across the device. To achieve this smooth surface there are several processes with which to polish the imaging surface, most notably mechanically polishing and ion milling. The most intuitive procedure is to mechanically polish the system using a series of increasingly fine

polishing pads as seen in Figure 2.3. Mechanical polishing may induce dislocations in the device, changing collection probabilities. This flaw is typically mitigated through the use of extremely fine grit pads and then using ion-sputtering system to remove the surface layer of the device. One downside to this technique is the mounting of samples to the paddle requires crystal bond, who's application requires the heating of the sample. Heating a sample can act as an annealing process, encouraging both defect and doping migration. As such we attempted to minimize this effect by using the alternative process: ion polishing.

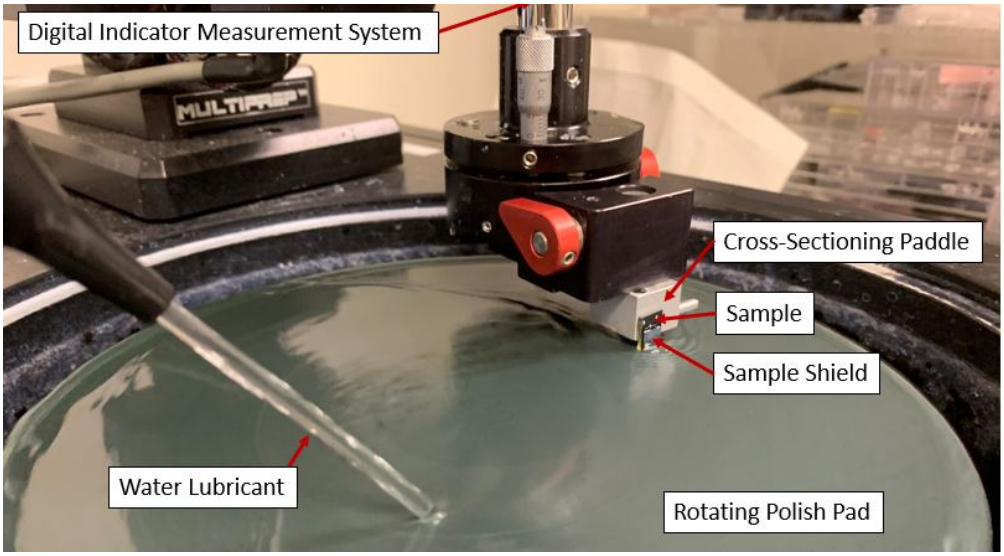

Figure 2.3 Configuration used for mechanically polishing cross section samples

The ion polishing process uses a JEOL Cross-Section Polisher to accelerate argon ions across the cleaved surface of the device, removing material[49]. An accelerating voltage of 3.5-4 kV was found to optimize surface smoothness and milling rates[28]. Increased voltage allows for faster milling, but increases the effect of non-uniformity in material mill rates. In this system accelerated ions follow a conical path from the gun to the sample with a gaussian distribution. Because of this, polishing is maximized when the region of interest is at the center of this cone and a metallic shield is required to prevent damaging the top surface of the sample. Illustration of device orientation and shield are seen in Figure 2.4. Differing materials may cause non-uniform milling which leads to surface roughness, or curtaining. This effect is mitigated by rocking the sample in the same plane as the imaging surface while keeping the region of interest near the axis of rotation. Deficits of this process are evident when dealing with samples with a non-uniform back contact such as figure 2.5. Samples were typically run for 8-12 hours in the cross-section polisher to create a large, smooth, imaging surface. One result of skipping the mechanical polishing step is an increased ion polish time and increased maintenance requirements on the Cross-section Polisher.

Material removed from the sample and shield often redeposit on the ion gun of the Cross-section polisher. This re-deposition can short the electrodes, as seen in figure 2.6.

Figure 2.4 An extreme case of in situ Ion Mill results. The ion shield acts as a sacrificial layer to prevent damage to the sample. The milled region is a roughly gaussian distribution caused both by the sputtered ion trajectories as well as the sample rocking procedure which reduces mill curtaining effects.

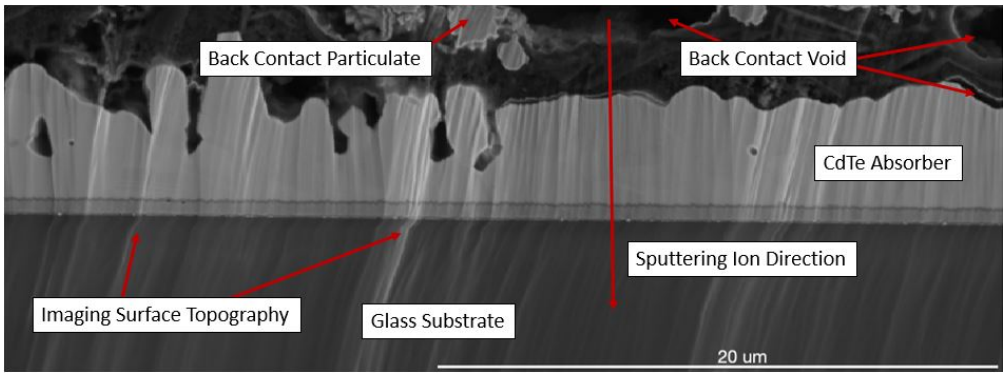

Figure 2.5 Ion Mill Through Non-Uniform Back Contact demonstrates the non-uniform milling, or curtaining of the cross-section surface. These effects can result in non-uniform generation, which in cause artifacts in the EBIC collection map.

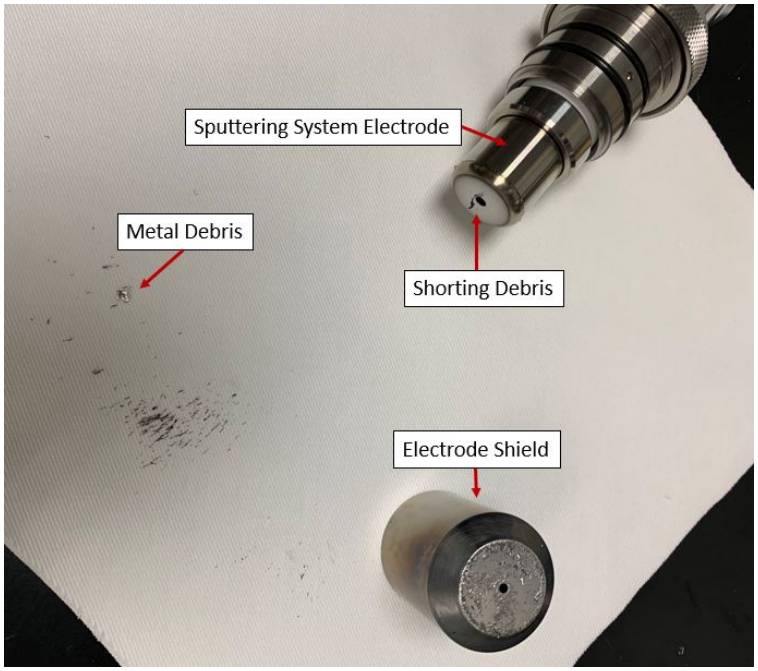

Figure 2.6 Ion Mill Electrode during cleaning. Metallic shards from the ion shields are attracted to the electric field of the electrode. The electrode operates with an electrode shield in place, however should a metallic shard fall between the electrode shield and electrode, it can short the electrode and stop the milling procedure. An example of such an arrangement is seen in the picture

A JEOL Cryo-Cross-Section Polisher was also used for ion polishing. This tool trades some tolerance in sample size for both temperature control during the milling process and the option of air-free sample preparation[10, 50]. As CdTe is a relatively stable material, we did not note significant improvements in image quality of prepared CdTe devices when using this tool over the more standard Cross-Section Polisher. Therefore the Cross-Section Polisher was the primary sample preparation tool used in these studies.

In the past other groups have used a FIB to ion mill regions of interest for EBIC purposes[50, 51]. We avoid this process because the Gallium used in this milling process can both damage and dope the imaging surface of the sample [52]. One notable work on this effect demonstrated the downside to this sample preparation method as it shifted the perceived junction position and decreased collection efficiency [51].

Next it was necessary to mount the sample and connect the mightyEBIC system to both contacts. Most previous EBIC studies have used conductive paint to attach wires to the contacts of a sample. The greatest downside to this process is that it requires that the paint be dry before imaging. If the paint is not dry, there exists a possibility of the connected wires moving or falling off the device during transfer. Non-dry paint may also off-gas while the sample is in the load-lock chamber, taxing that pump. Even quick-dry silver paint takes 24 hours to dry under standard temperature and pressure. This process can be hastened through the use of a heat-lamp, but it comes at the cost of heating the sample, which can induce

defect migration and surface oxidation in the sample. Another contact technique we attempted was through the use of a wire-bonding system. This process avoids the the drawbacks of conductive paint by ultrasonically vibrating the wire against the surface, causing local heating which partially melts the wire to the contact. This process should benefit from a much faster bond time while only heating a small area around the wire. We found that the ultrasonic vibrations frequently delaminated sections of the CdTe or CIGS devices due to low shear strength between adjacent device layers. As an alternative to these sample preparation techniques, NREL created a set of stages with which to mechanically make electrical contact with the sample without the need for paint. Key elements of the cross-section stage are illustrated in figures 2.7 and 2.8. Metallic probes are held in equilibrium between a screw and spring to maintain probe height. The addition of a bend in the probes was made to create 3 degrees of freedom: Height determined by screw tension, radial probe position, and probe angle. One major hindrance of this application came from the risk of mechanically damaging the sample by either scratching or puncturing layers of the sample with the relatively rigid probe. We mitigated the risk of mechanically damaging the sample through the use of springs, a thin probe contact, and a non-normal probe approach. The inclusion of more than 2 probes increased sample mounting complexity, but allowed for either 4-probe measurements or in-situ beam current measurements when combined with a faraday cup. Though the process is not without its challenges, it successfully provided a way to quickly mount a sample for EBIC imaging which did not heat the sample.

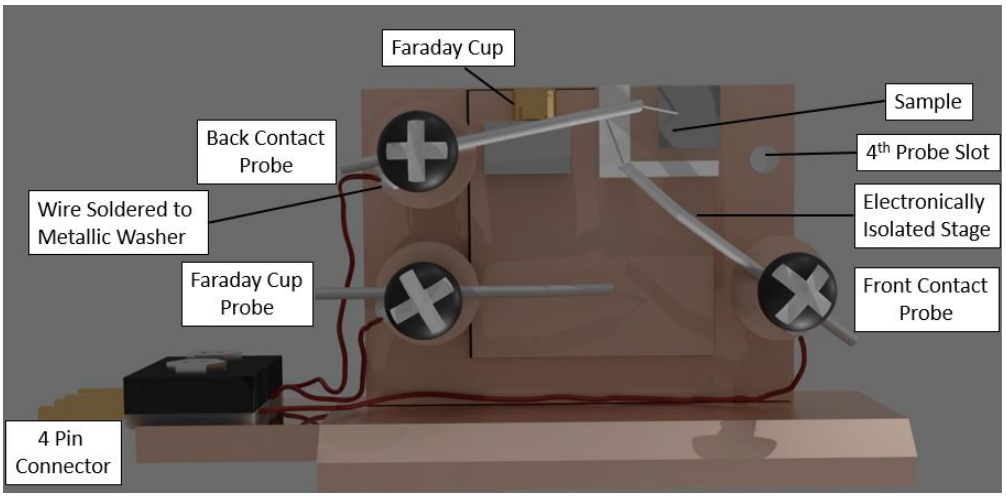

Figure 2.7 Experimental Apparatus of Mechanical EBIC Probe Configuration. This is a 3D rendered reconstruction of the apparatus created highlight features of the custom built apparatus. While 4-probe acquisition is possible with this construction, we used 3 probes for the majority of our acquisitions. 3 probes allow for a standard 2-probe EBIC acquisition which completes the photovoltaic circuit while also allowing in-situ beam current measurements without changing imaging conditions.

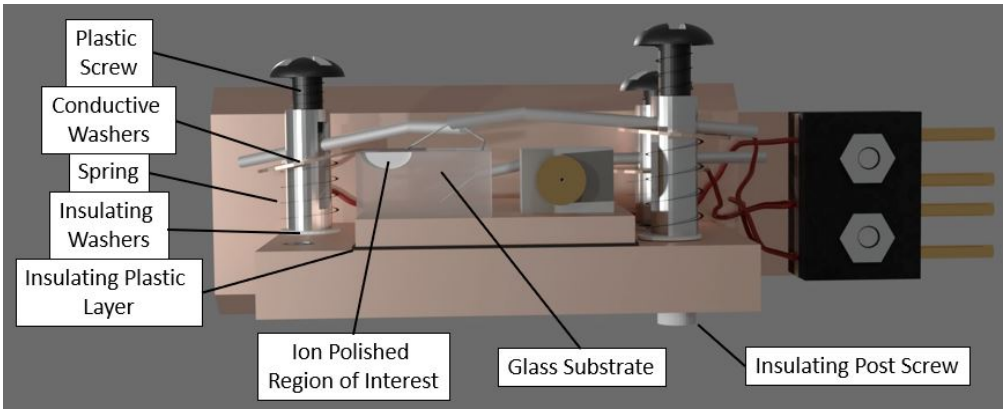

Figure 2.8 Alternate angle of Experimental Apparatus. False colors are used to accentuate the polished region of the sample because the dimensions of the polished regions are so small as to be difficult to see for most samples. The sample is mechanically fastened to the isolated stage using carbon tape. All probes were isolated from the stage with plastic screws and washers while a spring and plastic screw provided a vertical degree of freedom. The use of springs in this way increases the force tolerance of the application of a probe to the sample without causing mechanical damage and potentially shorting the device.

For voltage biased EBIC, we first attempted 4 probe analysis, but after observing high noise levels we instead turned to a two-probe arrangement where one side was subjected to a DC voltage bias while the other side was attached to the mightyEBIC measurement system.

The standard voltage-biased EBIC system configuration applies a pulsed beam blanker to the electron beam during image acquisition [43]. Current is then passed through coupled inductors before being further isolated through a lock-in amplifier. Filtered results from the lock-in amplifier are then passed to the scan controller. This process is done to isolate the EBIC signal from the voltage-induced current signal. This is necessary because the voltage-induced current scales with device area while the EBIC signal does not. The disparity in current scales typically results in a greatly reduced signal-to-noise ratio if only digital filtering is applied. Unfortunately while previous publications have demonstrated EBIC line profiles of these results, They have not presented high resolution collection maps. After we worked through this process we found that it yielded poor image resolution. To determine whether the low resolution was due to the voltage bias or the beam blanker, we imaged small devices where the voltage-induced current was of a similar magnitude to the EBIC signal. Because of these comparable currents, we were able to collect images without a beam blanker and digitally subtract the voltage-induced current. This yielded images with comparable resolution as unbiased voltage and supported the conclusion that the beam blanker setup led to low image resolution. Some factors of the beam blanker setup which we believe contribute to the low image quality is that first the coupled inductors take sinusoidal variations in collection while a beam blanker creates a square wave from the EBIC signal. Square waves result in higher frequency results which can decrease filtering efficacy.

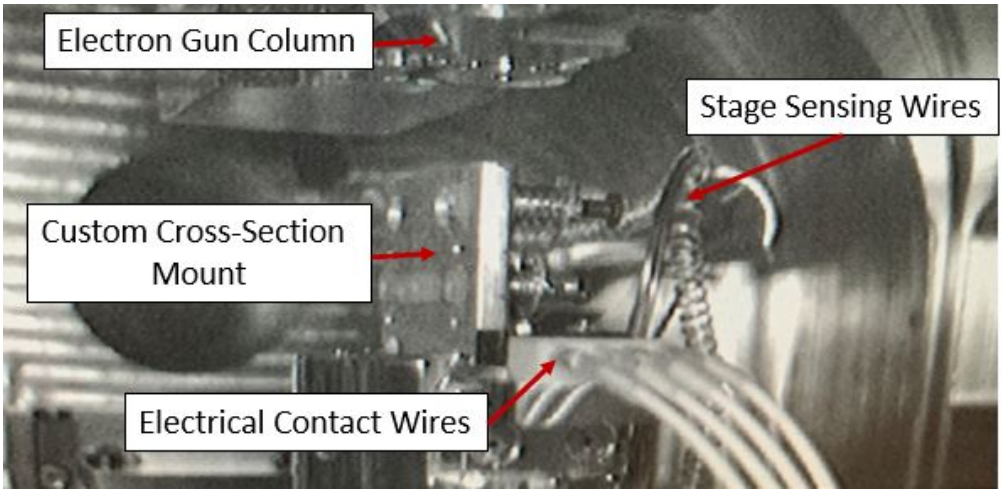

Figure 2.9 An image of the designed EBIC mount being used in the the SEM imaging chamber

Perhaps more importantly, the creation of a fluctuating illumination method changes the electrostatic field of the imaging surface of the device which changes the effective focus and stigmation. Sample-dependent charge and discharge times result in a variable field for which static imaging settings cannot compensate.

Given these shortcomings we instead looked to develop alternate EBIC techniques which did not require the beam blanker. We looked at using digital filtering and correlative pattern identification techniques with non-blanked voltage bias EBIC results. These digital processes require no additional experimental apparatuses. We also examined injection-dependent EBIC, as it's only additional experimental requirement was a faraday cup used to measure the in-situ beam current.

CHAPTER 3

EBIC FORMALISM

Table 3.1 Variable Definition Table

Variable	Name	Variable	Name
D	Diffusivity	$\vec{E}$	Electric Field
n	Carrier Density	μ	Mobility
τ	Minority Carrier Lifetime	S_c	Minority carrier recombination velocity
V_a	Applied External Voltage	V_{bi}	Built-in Potential
N_a	Active Acceptor Density	L	Absorber Thickness
G	generation	G_{crit}	Critical Generation
x_w	depletion width	R^*	Radius of Screened Region

3.1 Initial Collection Function

The collection function, ϕ, is defined as the probability that charge carriers excited at a position will be collected. Once generated, carriers must either recombine or be collected. Experimentally, EBIC is used to measure the short circuit collection probability of carriers given a generation position while CL is used to identify amount and energy of radiative recombination rates in an open-circuit condition. Because of this, the techniques are frequently seen as complementary and methods have been developed to use them together.

Under most published derivations, collection probability is assumed to be under low injection conditions [53] and valid for a point excitation. Low injection stipulates that collection is limited by minority carriers and that the collection function is injection independent [54–58]. Under these conditions, one may use green's theorem to create a continuity equation for excess minority carriers, n, at a position, r'. within a P-type region, this function takes the following form:

$$\nabla \cdot (D\nabla n + \mu n\vec{E}) - \tau^{-1}n = \delta(r - r') \tag{3.1}$$

where D and mu are the local diffusivity and mobility while E is the local electric field and τ is the effective minority carrier lifetime.

With ϕ established from these conditions, collected current is then taken from the integral of a generation function with the collection function across all space:

$$I = \int_V g(r)\phi(r)dV \tag{3.2}$$

3.2 Establishing Boundary Conditions

One may relax the ideality present in collection formalism by first assuming that carriers in the depletion region are fully depleted and that collection is limited by minority carriers for generation located at all points in the absorber. One may write the results of these assumptions as follows:

$\phi(x)$=1 for $x = x_w$ where x_w is the depletion width $-D_e \frac{d}{dx}\phi(x) = S_c\phi(x)$ where S_c is the minority carrier recombination velocity.

From this, one may solve the partial differential equation for collection efficiency for a point generation at a point x from the junction and for which $x > x_w$.

$$\phi(x) = \frac{\frac{1}{L_e}cosh(\frac{x-x_e}{L_e}) - \frac{S_C}{D_e}sinh(\frac{x-x_e}{L_e})}{\frac{S_C}{D_e}sinh(\frac{x_C-x_{scr}}{L_e}) + \frac{1}{L_e}cosh(\frac{x_c-x_{scr}}{L_e})} \tag{3.3}$$

One sticking point which is then frequently mentioned is the variability of effective diffusion length as a function of distance between a generation point and imaging surface. Because JEBIC attempts to understand bulk properties while applying an electron beam to an unpacified imaging surface, the condition of the imaging surface may play a role in all measurements.

In other words, the condition of the imaging surface changes how carrier lifetime varies as a function of distance from the imaging surface; this decreases the separability of the collection and generation function which further impairs the accuracy of low injection assumptions within EBIC imaging.

3.3 Relaxing Low Injection Assumptions

The next step in increasing model fidelity and interpret-ability was to relax the assumption of low injection imaging while attempting to quantify results. This was achieved by constructing a spherical metallic region around the beam position. In this way, the behavior of the sample is still treated using the low-injection construction of section 3.2 and effects of the high injection are instead treated as a deviation in the imaging probe.

$$J_{ph} = \mu N_a \dot{E} x dy dz = 2\pi\mu \frac{L}{1 - \frac{R^*}{L}} V_{bi} N_a \tag{3.4}$$

with a critical generation defined as the greatest generation with $R^* = 0$. This critical point is established in equation 4.5.

$$G^{3d}_{crit} = 2\pi\mu N_A V_{bi} L \tag{3.5}$$

The relation between the generation rate and screened radius is not simply a geometric relationship since one must take into account changes to both recombination and photo-current.

$$G = G_{crit}\frac{sinh(\chi)}{(1 - L_R\chi)\chi} \tag{3.6}$$

In this equation χ is the ratio of screened radius to low injection diffusion length and L_R is the ratio of low injection diffusion length to the device length. In accordance with our boundary conditions, the equation has R* asymptotically approach 0 as G approaches G_{crit} and when $G >> G_{crit}$, $R^* \approx L$.

3.4 Relaxing Short Circuit Assumptions to allow for Voltage Bias

When applying a voltage bias below crossover, the boundary conditions for the high injection derivations hold. As such, an evaluation of the photo-current is obtained through partial differentiation of the previous equation.

First we evaluate the critical generation rate, as it provides an intuitive understanding of what changes in collection may occur. Assuming a parabolic band diagram, the device length (L) and mobility (μ) should be constant with respect to an external bias. Therefore the critical generation should change in the manner illustrated in equation 3.9.

$$\left(\frac{\partial}{\partial V_a}\right)_{G,x_0} G^{3d}_{crit} = 2\pi L\mu \left(\frac{\partial}{\partial V_a}\right)_{G,x_0} (N_A V_i) \tag{3.7}$$

$$= 2\pi L\mu (N'_a(V_{bi} - V_a) + N_a) \tag{3.8}$$

$$= G^0_{crit}\left[\frac{1}{V_{bi}} + \frac{N'_a}{N_a}\left(\frac{V_{bi} - V_a}{V_{bi}}\right)\right] \tag{3.9}$$

where $N'_a = \frac{\partial N_a}{\partial V_a}$. Previous CV results have demonstrated that this value is most likely the sum of multiple error functions correlating to positions where the fermi energy levels are equal to dopant energy levels weighted by capture probability.

We can then use this change to evaluate the change in photocurrent as a function of collection. Next we evaluate the change in photocurrent under generalized conditions where injection condition and thus R* are unknown and the beam position is in a generic location in the quasi-neutral region.

$$J_{ph} = 2\pi\mu\frac{(L - x_b)^2}{L - x_b - R^*}V_i N_a \tag{3.10}$$

note that x_b is measured relative to the edge of the depletion region under low injection. as such we substitute it with a generalized position relative to the front contact, x_0, Where $x_b = x_0 - x_w$. Taking the derivative of photocurrent at constant generation rate and beam position while acknowledging injection dependence yields equations 3.11 through 3.14:

$$(\frac{\partial J_{ph}}{\partial V_a})_{G,x_0} = \tag{3.11}$$

$$= 2\pi\mu(\frac{\partial}{\partial V_a})_{G,x_0}\left(\frac{(L-(x_0-x_w))^2}{L-x_b-R^*}V_iN_a\right) \tag{3.12}$$

$$= \frac{-J^0_{ph}}{V_{bi}} + J^0_{ph}\frac{N'_a}{N_a} + J^0_{ph}\frac{2}{L-(x_0-x_w)}\frac{\partial x_w}{\partial V_a} + J^0_{ph}\frac{1}{L-(x_0-x_w)-R^*}\left(\frac{\partial R^*}{\partial V_a} - \frac{\partial x_w}{\partial V_a}\right) \tag{3.13}$$

$$= J^0_{ph}\left[\frac{-1}{V_{bi}} + \frac{N'_a}{N_a} + \left(\frac{\partial R^*}{\partial V_a}\right)\frac{1}{L-(x_0-x_w)-R^*} + \left(\frac{\partial x_w}{\partial V_a}\right)\left(\frac{L-(x_0-x_w)-2R^*}{(L-(x_0-x_w))^2-(L-(x_0-x_w))R^*}\right)\right] \tag{3.14}$$

If one then applies low injection assumptions to this equation, it yields equation 3.15.

$$(\frac{\partial J_{ph}}{\partial V_a})_{G,x_0} = J^0_{ph}\left[\left(\frac{-1}{V_{bi}} + \frac{N'_a}{N_a}\right) + \left(\frac{\partial x_w}{\partial V_a}\right)\left(\frac{1}{L-(x_0-x_w)}\right)\right] \tag{3.15}$$

The grouped position-independent terms represent a net reduction in efficiency across the entire device while the third term represents a change in collection caused by using the laboratory frame (x_0) for our generation position. The third term arises because the laboratory position references the front contact position while collection in the quasi-neutral region depends on the distance between generation position and the edge of the depletion region, x_b. This formalism has not been used in existing publications but provides key insight into the role that voltage plays on current collection in an ideal sample.

The greatest difference between equation 3.14 and 3.15 is the third term in 3.14 which acknowledges that variable voltage may impact injection condition. Under large forward biases, the effective device voltage, $V_{bi} - V_a$, decreases which should change the critical generation rate and may result shift the device into high injection conditions although injection would not change. Similarly, large reverse biases may prove an effective method to image a device with low critical generation under low-injection conditions. This is a research path which has not been explored but which is recommended for future research.

This formalism acknowledges and reduces assumptions in quantitative EBIC measurements and will be used in chapters 5 and 6 to better explain the expectations and interpretation of our results.

CHAPTER 4

APPLICATION OF PCA TO SIMULATED COLLECTION FUNCTIONS

One key advantage to applying PCA to a collection function under variable bias is the ability to identify regions which behave similarly. This is because the technique decomposes the voltage response into modes which best represent changes in the collected data. The PCA process attempts to express the image as the sum of two products:

$$I = \Sigma F_i(V_a) G_i(x_0) \tag{4.1}$$

Equation 4.1 uses i to represents a mode of change; thus $F_i(V_a)$ is the coefficient vector with length equal to the number of voltages sampled while $G_i(x_0)$ is the significance of this voltage response to each pixel located at x_0. Therefore, by comparing $G_i(x_0)$ for multiple modes, one can identify regions in which the collection function changes systematically and who's evolution can be expressed with a single $F(V_a)$. For example consider a region in which $G_1(x_0)$ is linearly proportional to $G_2(x_0)$:

$$G_2(x_0) = C_1 * [G_1(x_0) + C_2] \text{ for } x_0 \in Region \tag{4.2}$$

Then for that region, the rank 2 collection function can be summarized by the following equation:

$$\Sigma F_i(V_a) G_i(x_0) = G_1(x_0) * (F_1(V_a) + C_1 * F_2(V_a) + F_2(V_a) * C_2) \tag{4.3}$$

From this we see that the region 1 collection function evolves with voltage in a manner proportional to G_1. This analysis could be extended to an arbitrary number of regions, and if there is a linear relationship, collection function will be proportional to a single position function while the voltage function will be different for each region.

4.1 Applications to an Idealized 1D simulation

Next we consider a simplistic 1D CdTe model with a delta function excitation. Details and example code for the model are presented in appendix C. This model is idealized such that there is uniform composition in the CdTe and MZO layers as well as ohmic contacts. We excite 1e14 carriers in a delta function, and evaluate the collection at 51 voltage bias values between -1 and 1 volts. The generated carrier density is extremely low when compared to experimental EBIC and the variable was chosen since it should be in the low-injection regime and thus add to the ideality of the simulation. Figure 4.1 shows 1D EBIC solution and its evolution with voltage bias presented as a surface. With respect to this presentation

method, traditional voltage-bias EBIC results compare line profiles which sample the results at fixed voltage bias values, such as the black line highlighted. This differs from spectral JV responses, since those integrate the position-dependent collection and plot this integration as a function of voltage. Spectral JV collection then changes the integration function by changing the spectral energy, which affects the penetration depth as a function of beam energy.

If one were to approach voltage-bias EBIC in a similar manner to spectral JV measurements, they could collect JV measurements as a function of some fixed beam position. Results of this approach are seen in Figure 4.2. Figure 4.2 shows the systematic increase in shunt resistance as one excites carriers further from the front contact. This is because, in the low injection regime, collected current is dictated by minority carriers, collected at the front contact in our model.

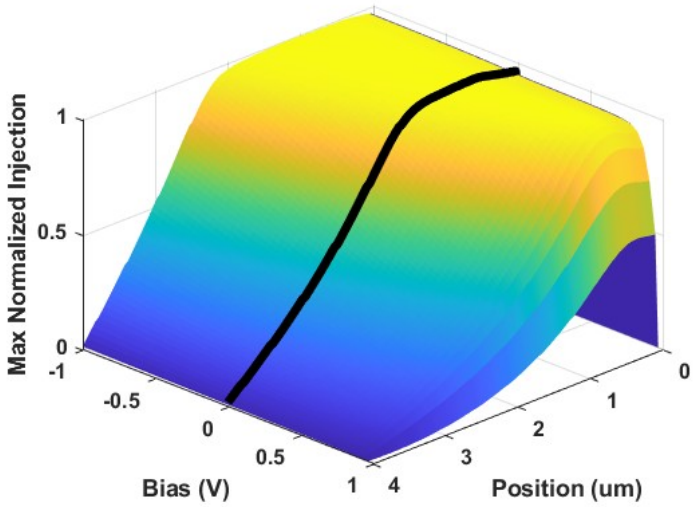

Figure 4.1 A 3D plot of the collection rate using generation position and applied bias as independent variables. A standard EBIC collection map contains the data of the black line while injection dependent or spectral photocurrent measurements integrate along the generation position, weighted by intensity, and plot this integrated photocurrent against the applied bias. Regions near the 0um position which demonstrate relatively uniform collection are frequently referred to as the depletion region, in which free charge carriers are removed by a strong electric field.

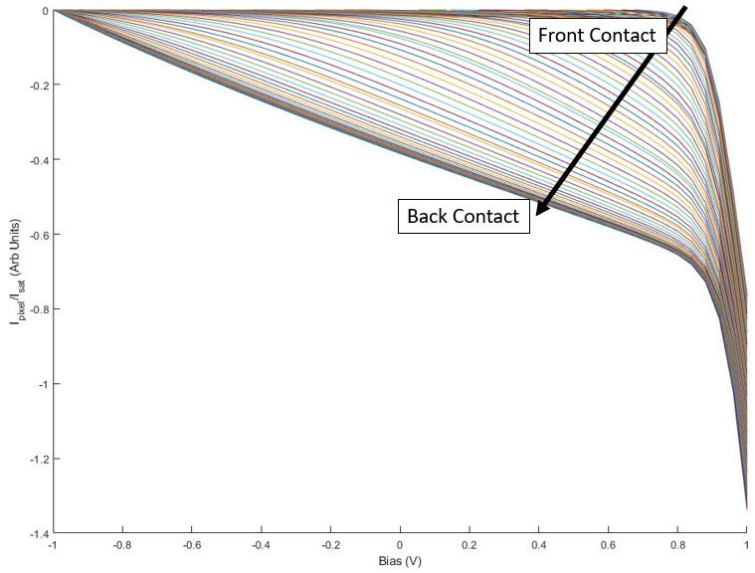

Figure 4.2 JV response of each pixel in the device. This plot is analogous to a 2D view of figure 4.2. Systematically increasing shunt resistance is due to increased minority recombination probability with increased distance from the front contact.

In contrast to the two approaches, PCA attempts to find the optimal direction with which to view the solution surface of Figure 4.1 such that the information density is maximized. Based on equation 3.15 we expect three key regions to become apparent after applying PCA analysis. First we expect the depletion region to emerge and demonstrate a voltage-independent collection efficiency. Next we expect the quasi-neutral region to be divided into two regions depending on whether the total scaling of collection efficiency exceeds the position-dependent collection change caused by a shifting depletion width. Figure 4.3 shows the position functions and voltage function of the first two modes. While trends may be identified by comparing the changes in spatial functions plotted against position, this method is not as tractable for large non-ideal data sets as a direct correlation between the two spatial function.

Figure 4.4a shows such a correlation between the first two data sets shown in figure 4.3. From this plot, four regions were identified based on systematic trends in spatial function values. The spatial locations of each of the four regions were then identified and plotted in figure 4.4b while their average voltage responses are identified in figure 4.4c. This average voltage response for each region was calculated using equation 4.4. From figure 4.4b we can identify the three predicted regions as well as an additional region associated with the edge of the depletion region. This extra region, labelled region 2, is quite interesting as it was not differentiable using our initial formalism. Region 4, near the back contact, is a region for which the shifting voltage response does not have a significant impact on changes to collection since $\Delta x_w << x_0$. While this difference was predicted, the voltage responses show the extent to which these values differed since region 4

shows a linear voltage response while region 4 contains a voltage response proportional to $\sqrt{(V_a)}$. From this variable voltage response, calculated using equation 4.4, we observe results which are consistent with the derivations of chapter 4.

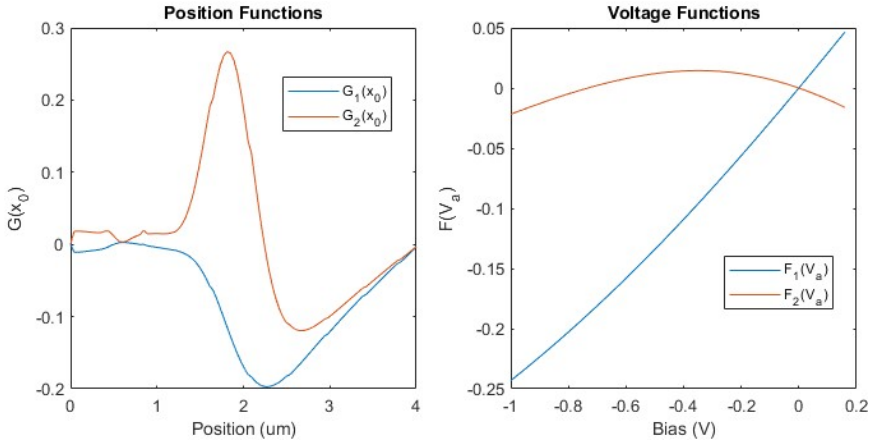

Figure 4.3 A comparison of the spatial and voltage functions of the first two modes. Regions of the spatial function with high amplitude are strongly influenced by the voltage function of the same mode.

While this analysis methodology can be used to provide valuable quantifiable characterization to such ideal data sets, its true strength lies in the characterization of more complex and less ideal samples.

$$\Delta I_i = < G_1(x_0 \in R_i) > * F_1(V) + < G_2(x_0 \in R_i) > * F_2(V) \tag{4.4}$$

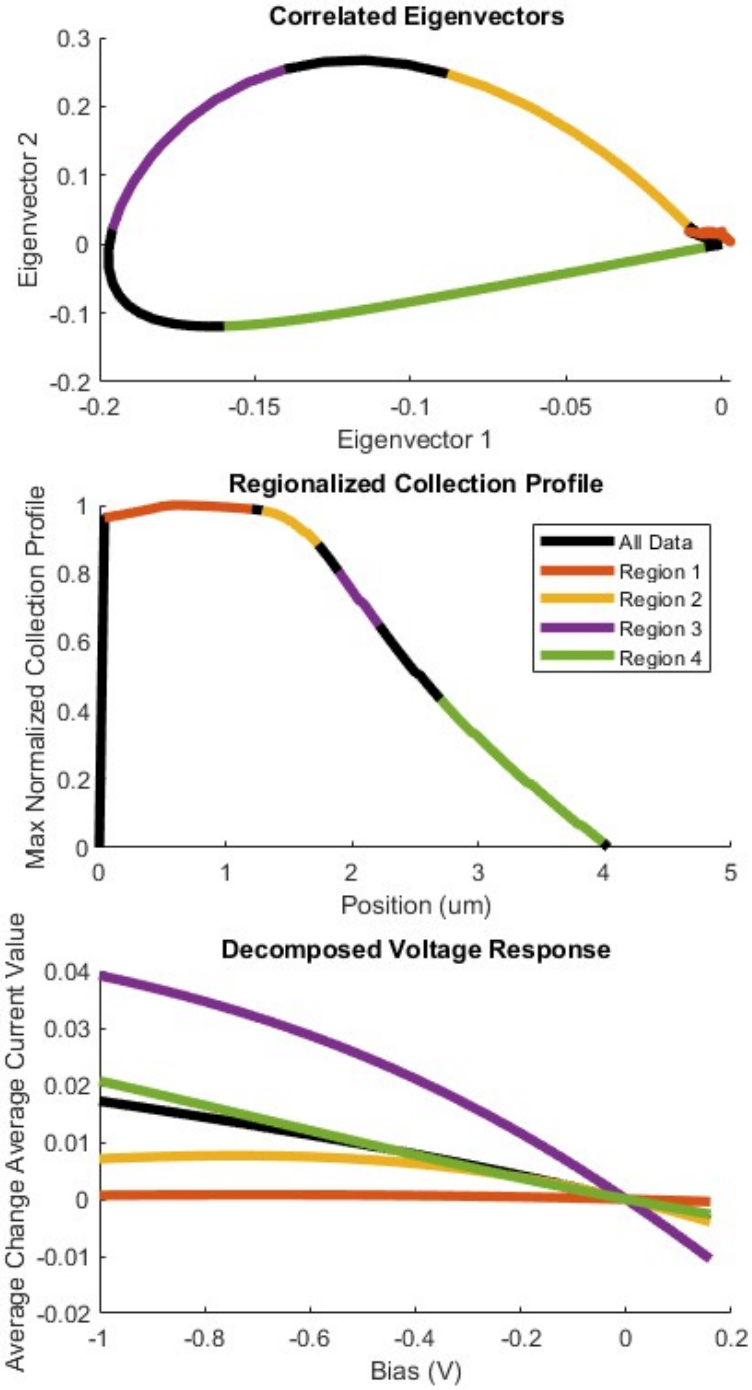

Figure 4.4 First results are grouped based on trends in correlation of the first two eigenvector values. Then these groups are superimposed on a zero bias collection bias. Then we weight the sum of the voltage function by the average collection function value for each region to create a decomposed voltage response. Note that since we primarily care about changes to voltage response with respect to the collected current at $V_A = 0$, we use that value to center our results, which is why all voltage responses intersect at the origin. The black functions in each plot represent all results regardless of region.

4.2 Applications to a 1D simulation containing a grain boundary

Next consider a more complicated device structure with an uncharged grain boundary that runs parallel to the junctions. We applied this simulation as these lateral grain boundaries have been observed in CdSeTe/CdTe devices and they have not been largely addressed in literature[34, 42, 59]. Initially following work similar to two previous publications[42, 60], we first grouped data into two distinct regions based on their location relative to the grain boundary. Region 1 is the position range between the front contact and grain boundary while region 2 is the position range between the grain boundary and back contact. Much like figure 4.2, we plotted the JV response of 100 representative pixels of the simulation in Figure 4.4 and 4.5. Figure 4.4 shows the voltage response of the whole device while figure 4.5 segregates the JV curve of regions 1 and 2. Due to the non-linear effects, these voltage responses are significantly more difficult to interpret than those of figure 4.2.

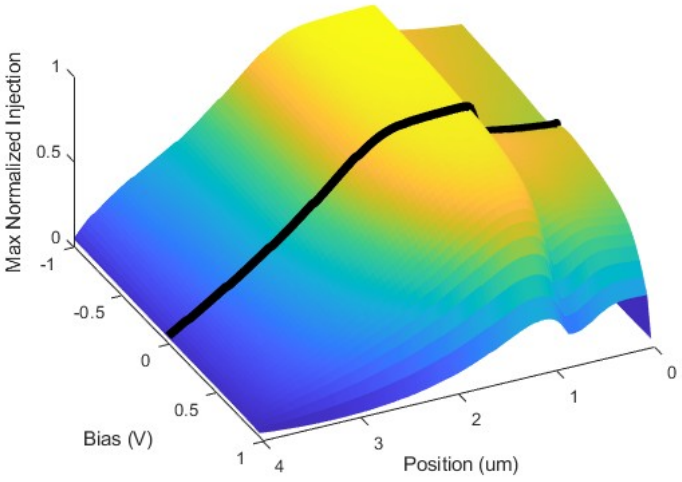

Figure 4.5 A 3D plot of the collection rate using generation position and applied bias as independent variables. A standard EBIC collection map contains the data of the black line while injection dependent or spectral photocurrent measurements integrate in the generation position while and plot along photocurrent against the applied bias. Region 1, which exists between x=0 and 1, demonstrates non-linear collection behavior.

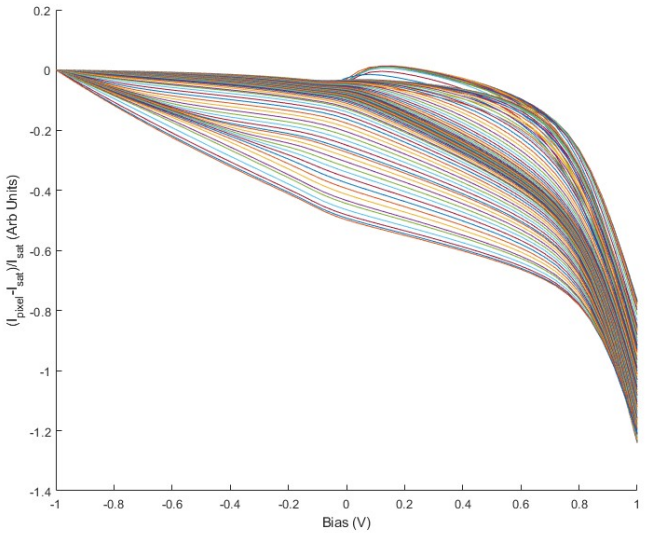

Figure 4.6 JV response of 100 representative pixels in the simulation. This demonstrates systematic changes which are more difficult to identify than those of figure 4.2.

We again decompose the collection function using PCA with biases less than 0.2V. This voltage limit was chosen since it contained the JV non-linearity in its entirety but not the max power point. Spatial function correlations are seen in figure 4.7 and clearly differentiate our two pre-defined regions. That being said, region 2 is far from homogeneous in its correlated trends. Because of this, we further subdivided region 2 into 4 additional regions labelled a-d. With this subdivision, we are able to once again compare the correlated values, EBIC efficiency, and average JV response in figure 4.10. From there, we can use these regions to decompose the data of figure 4.7 onto 5 discrete regions which each contain systematic trends of changes in collection, as is seen in figure 4.11. The systematic trends in collection mean that certain assumptions regarding variables such as injection condition, electric field strength, and collection rate apply to all elements of each region.

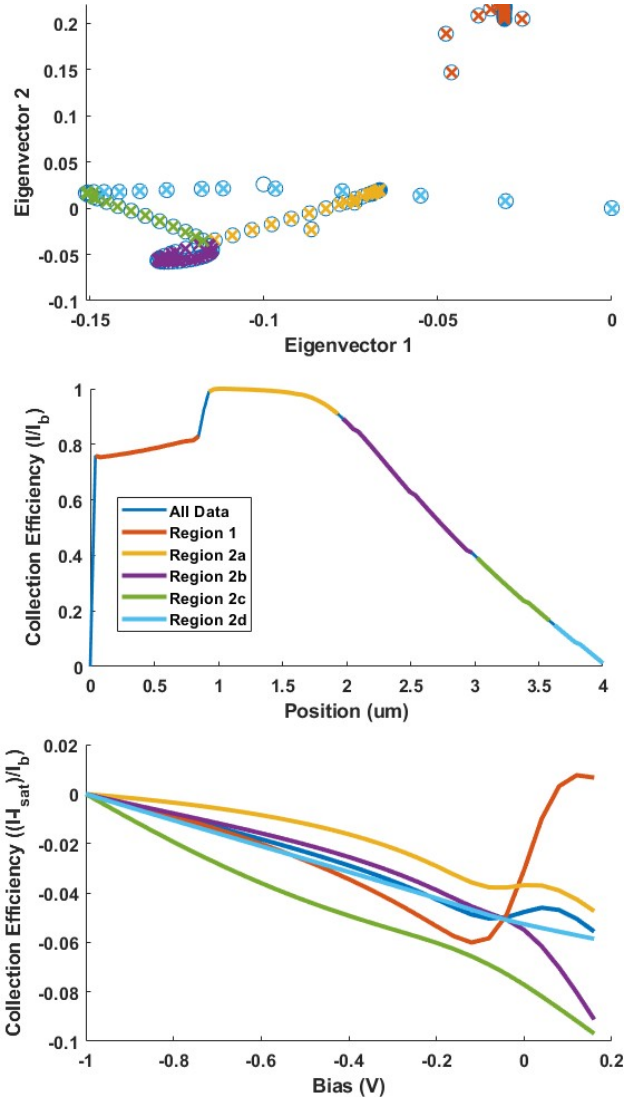

Figure 4.7 Here we demonstrate using PCA correlations to further subdivide results based on electrical properties rather than position with respect to the grain boundary. This is a corrolary to Figure 4.4 and shows non-ideal collection profiles.

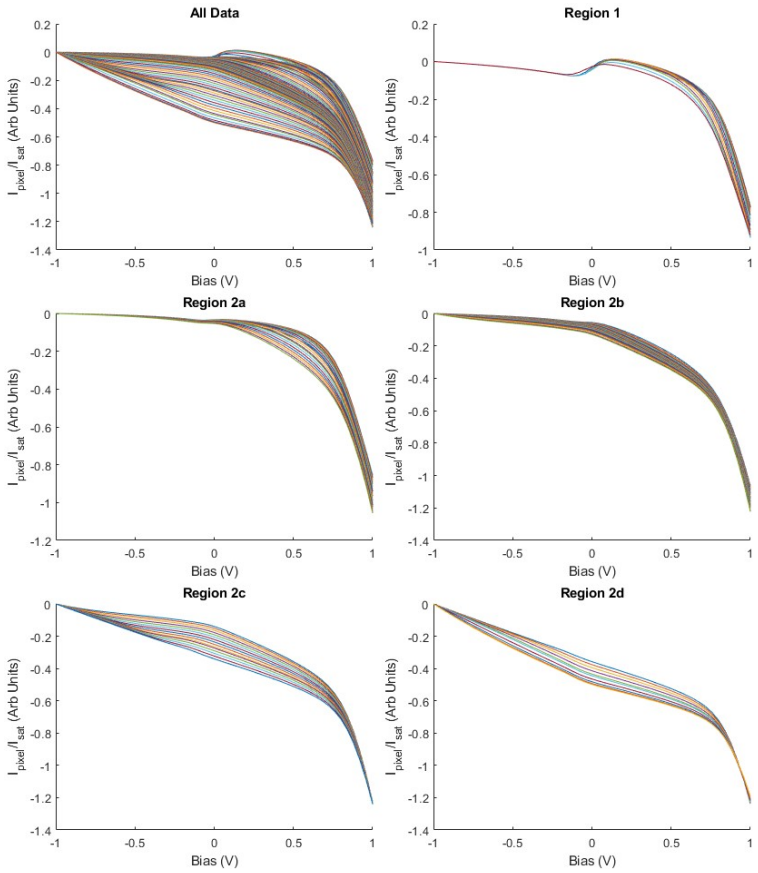

Figure 4.8 Decomposed JV response of 100 representative pixels. The 5 regions each contain non-linearities which evolve systematically, as compared to the structural decomposition of figure 4.6

One previously reported phenomenon which results in decreased fill factor in CdTe devices is the roll-over or roll-under effects. These effects are typically seen in devices with a barrier to collection near the back contact. In these cases, the barrier creates an electric field which opposes barrier collection. The key difference between roll-over and roll-under effects is the bias at which the barrier is overcome and its relation to the Voc position. Devices with such barriers to collection are typically described using a two-diode equivalent circuit. However in this simulation, the barrier to collection is located towards the center of the absorber layer. This construction still leads to a nonlinear JV behavior which decreases the fill-factor as is seen in figure 4.7, but a two-diode model is no longer applicable.

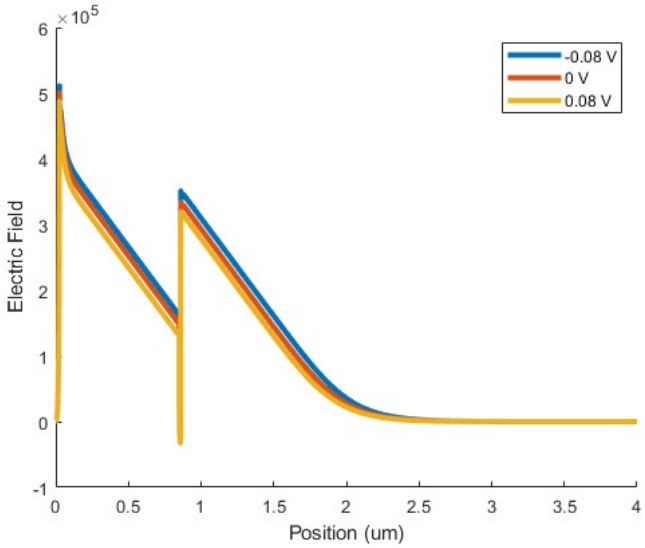

Figure 4.9 A plot of the electric field strength in the grain boundary. This plot shows two regions of strong electric field pointing in the same direction while the electric field at the grain boundary has low strength and may point in the opposite direction

Figures 4.11 and 4.12 show the electric field across the device at 3 voltage biases. This electric field measurement is similar to what is obtained through KPFM, and the profiles is similar to one such published measurement[7]. Figure 4.11 demonstrates two field peaks while figure 4.12 focuses on the field near the grain boundary. From this, we see that the JV non-linearity correlates to the development of a field which opposes the field of the p-n junction. Figure 4.13 shows how this field also correlates with a minority carrier inversion point whose position shifts with bias. The shifting field position and strength as a function of bias is one feature which has not been previously addressed in KPFM studies. KPFM measures variations in work function. In order to negate surface effects, it is common to take these measurements while the sample is under a reverse bias. While this is a valid method for minimizing characterization artifacts, it is not standard to verify the validity of bias conditions through measuring

similar potential profiles at multiple bias values.

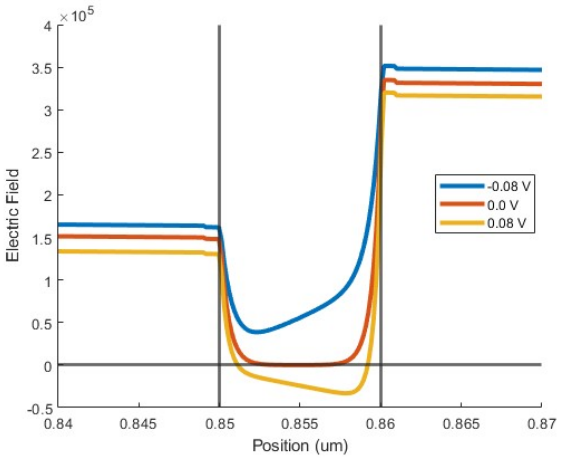

Figure 4.10 A plot of the electric field strength in the grain boundary. Positive biases contain an electric field acting against the two fields in figure 4.12, while negative biases contain a field in the same direction.

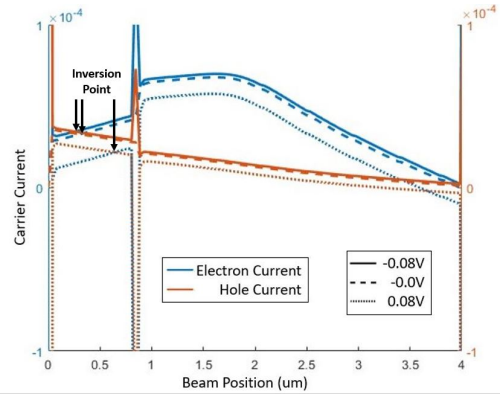

Figure 4.11 A comparison of the carrier currents near the JV inflection point of region 1. This diagram demonstrates a homojunction who's position shifts with bias within this region. At more positive biases, region 1 is primarily p-type while at more negative biases, region 1 is primarily n-type. Because the grain boundary acts as a strong collection barrier, region 1 behaves as an npn transistor while region 2 behaves more like a diode. The process of scanning region 1 with an electron beam is comparable to applying a voltage to the transistor gate, which changes the voltage response of this region during imaging.

From all of this, we contrast three equivalent circuit models in figure 4.13. First, we could express the device using three diodes oriented oppositely. This visualization best enables comparison with the more traditional two-diode method. Through this, we could express the non-linearity as a break-down in the barrier diode while the two similarly oriented diodes allow for handling non-linear spectral response caused by generation in different regions. Alternatively we could express the diode as either a diode-transistor model or a thyristor model. These models are less typically used in diodes, but highlight a key feature of

EBIC characterization. Both the transistor and thyristor models contain the assumption of a gate region within alternating npnp layers. While CdTe devices are not designed with some method to turn these gates on and off, the generation of carriers during EBIC characterization may perform a similar function. While this effect is one of the variables which make EBIC characterization more ambiguous, it also provides the opportunity for greater understanding of a sample through injection-dependent EBIC.

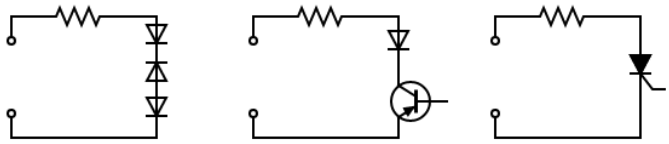

Figure 4.12 Three equivalent circuit diagrams which would result in the npnp divisions as well as the JV response observed in this simulation. The three diode model provides an accurate model for a photovoltaic device. The diode-transistor model best expresses the non-idealities of the device while allowing for injection from generation based characterization. The thyristor model provides the most abbreviated equivalent circuit model while allowing for mid-absorber generation

CHAPTER 5

EXPERIMENTAL RESULTS SMALL AREA DEVICE VOLTAGE SERIES

5.1 Applications of voltage bias to Small Area Devices

After applying PCA to simulated 1 dimensional voltage-biased EBIC models, we then expanded this form of characterization to an experimental sample with small lateral area. The small area of the device allowed for the voltage-induced current to be of a similar order of magnitude to the beam-induced current. Through this experiment we hoped to answer the question of whether the limited spatial resolution of previous voltage-biased EBIC experiments was inherent to the application of a voltage bias to the sample or whether it was caused by the methods previously used to isolate EBIC signal from the voltage induced current. In the case that the latter cause were true, we aimed to apply PCA to identify regions with similar voltage responses like we did in chapter 4. The device was grown by industrial partners to have small lateral area, and post-cleave its area was approximately $1.5mm^2$. With this device, we prepared and mounted it using the methods of chapter 2.

Under these conditions, we once again looked to correlate the eigenvector values of the first 2 eigenvectors, or spatial component functions. This time, we use a density map instead of a scatter plot due to the large number of data points in the 2D image compared to a single line profile. The density map of figure 5.1 shows 6 regions of high frequency spatial function correlation superimposed on the spatial function correlated density plot. Each region was represented by a second order polynomial in this correlation space and all pixels which fell within a distance of 1e-4 were selected to be part of the region. This selection process was highly stringent and not all pixels were represented, but it allowed for the regions to not overlap as well as decreasing uncertainty in the collection trends of each region.

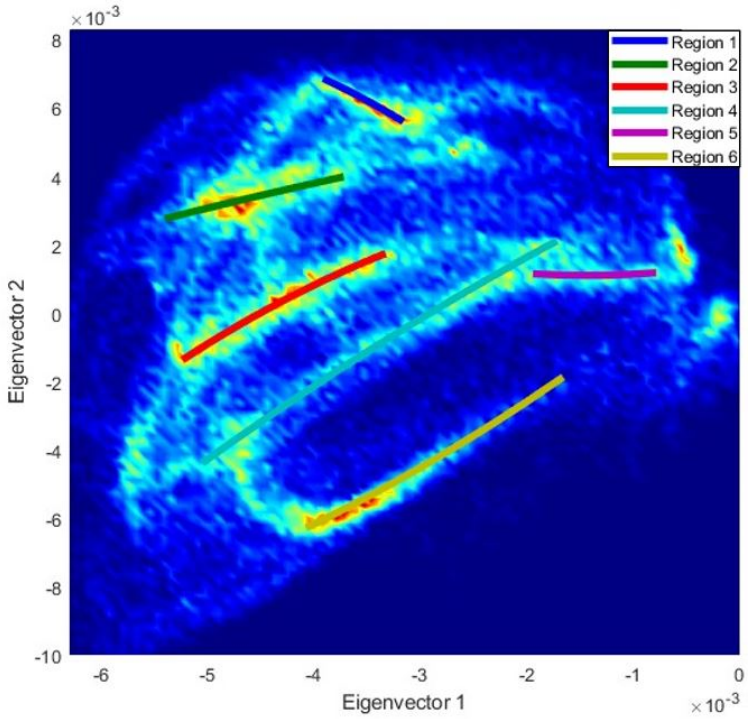

Figure 5.1 Correlated Eigenvectors with 6 regions identified. Pixels which fall within correlation value of 1e-4 of a line are considered part of that group. These groups do not contain all pixels, but were chosen to highlight systematic trends in the changes in collection.

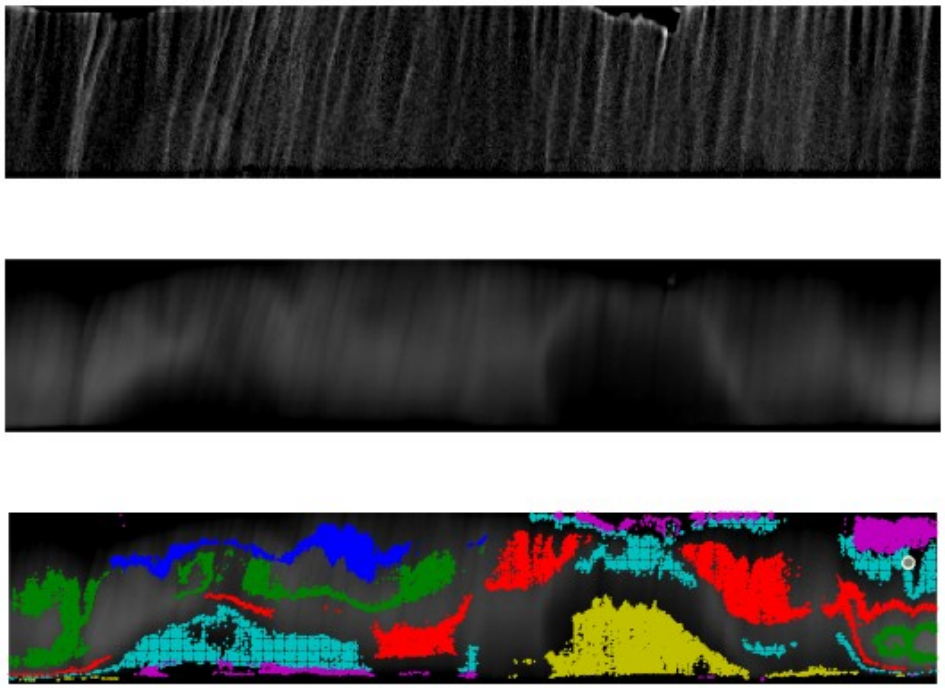

Figure 5.2 A comparison of the 0V CdTe J-EBIC collection map and secondary electron image with each of the 6 groups spatially correlated. The spatially correlated groups demonstrate some grid-like visual artifacts which are not indicative of systematically omitted results.

Next, we superimposed the spatial position of each region's elements over the unbiased EBIC image in figure 5.2. The spatial cohesion of each group suggests that this is caused by systematic changes in collection rather than random error in our collection efficiency. The highlighted regions are interesting since each population demonstrates systematic changes in collection efficiency which, in an ideal extreme, should be directly correlated with position relative to the junctions. Because of this, the lateral variation in these population positions indicate conduction pathways in the results.

Visually the regions did not appear to show strong correlation with the unbiased collection efficiency. We tested this correlation by creating a 2D violin plot in figure 5.3 which contrasts the unbiased collection efficiency distribution with each region. In this plot, the width of each group correlates to the frequency of that collection value within the group in the unbiased EBIC image. This plot demonstrates and extreme overlap in the unbiased collection of groups 1 and 3, as well as 4 and 6. The range of unbiased collection of group 1 and 6 are entirely contained in the collection range of regions 3 and 4, respectively. Then figure 5.4 demonstrates the average JV performance of each region using the procedures similar to a previous study which studied the impact of light intensity on device ideality[61]. This plot shows clear differentiation in performance of the regions whose unbiased EBIC response is otherwise indistinguishable.

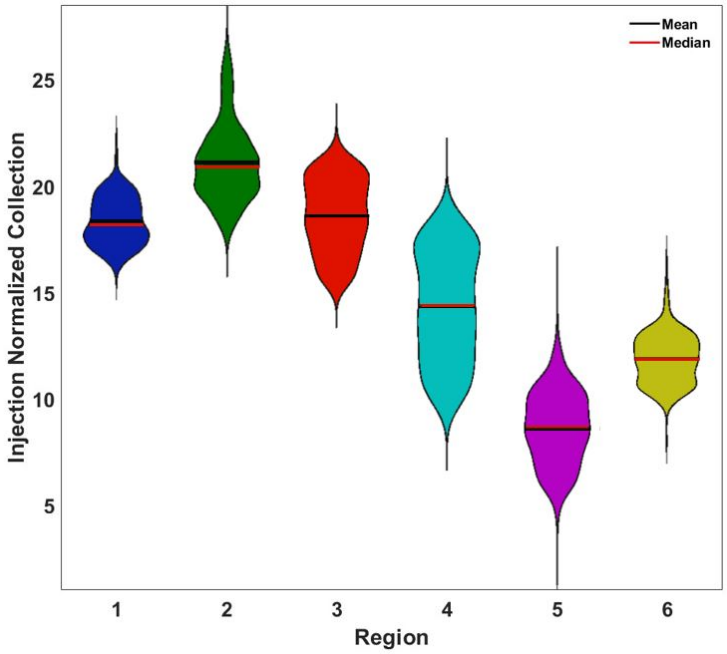

Figure 5.3 This violin plot shows the frequency of correlation between each of the six identified regions and the injection normalized collection seen in figure 5.2a. The width variation of each data set is reflective of a smoothed histogram with increased width corresponding with increased frequency of occurrence.

Figure 5.3 supports a previous simulation-based publication which bluntly stated that unbiased EBIC evaluation were not indicative of device performance[34]. While their study focused on simulations of columnar grains with boundaries running perpendicular to contacts, ours is a more generalized experimental result. We believe that a major source of this incongruity comes from non-linearities in injection conditions such as those simulated in chapter 5. Chapter 5 demonstrated a simulated example which contains a grain boundary that runs parallel to the junction that impedes carrier diffusion. On one side of the grain boundary, the element impedes majority carrier diffusion resulting in carrier accumulation and the onset of high injection while the other side of the grain boundary will impede minority carriers, not resulting in the same charge accumulation.

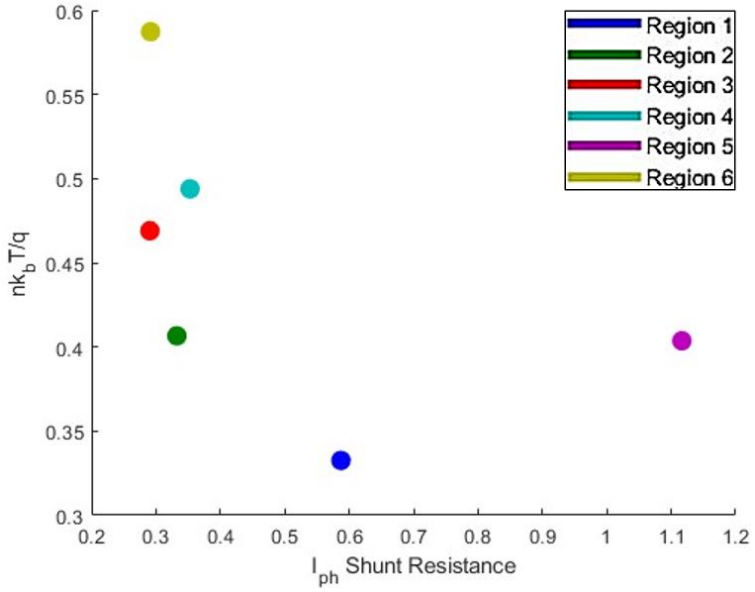

Figure 5.4 Average JV response characteristics of all 6 regions of the collection map. The y values are the inverted coefficient of the exponential voltage coefficient. These values are proportional to the ideality factor, n.

5.2 Effects of Beam Damage

While these results do provide strong evidence for the disconnection between EBIC collection and local device performance, the acquisition method begs the question of what systematic errors may exist. Given that this imaging technique requires the repeated imaging of a single region, it stands to reason that continuous exposure to high energy electrons may induce defects and change our measurements. To evaluate this effect, we imaged the sample under 0V bias at the beginning, middle, and end of our procedure while also monitoring the acquisition time of each image.

First we use figure 5.5 to show the average JV response of each region at each voltage setting. These response curves were used to create figure 5.4 and the 0V discontinuity suggests the variability in unbiased collection from the three sampling points. Response curves are divided into two subplots to reduce function crossover and increase plot legibility since the two regions in the right plot show smaller reverse bias current.

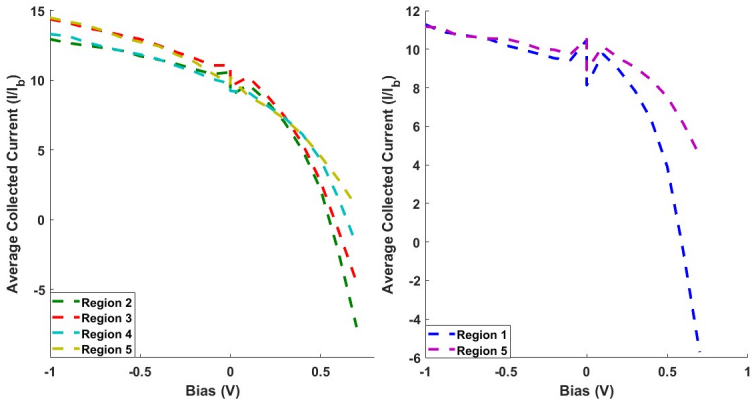

Figure 5.5 JV response of each of the 6 regions. The regions of the left plot show a systematic change to ideality. The regions in the right plot showed greatly increased shunt resistance in figure 5.4.

We further explore the impact that electron dose has on collection efficiency in Figure 5.6. Figure 5.6 contrasts the time since the first image was taken with average unbiased collection rate of each region. Acquisition took 350s for 20 images, averaging less than 20 seconds between each image acquisition. From this, we see a net decrease in collection for most groups, with the notable exception being region 6 which show a slight increase in collection efficiency as a function of beam exposure time. The decrease in collection efficiency with increased dose should result in a slight underestimate of device ideality when compared to

A decrease in collection is to be expected since the creation of defects should increase trap-assisted recombination, decreasing carrier lifetime and thus collection efficiency. By the same token, Region 6 is a large outlier because it shows a net increase in collection efficiency with additional electron dose. As this region 6 shows a low average unbiased collection efficiency, we hypothesize that there exists a barrier to this region's collection which is not present for other regions. Under these conditions, it is possible that the damage to the collection barrier from electron beam exposure resulted in an increase in collection rate that outweighed the expected decrease in collection efficiency. The mechanisms behind this collection irregularity are difficult to further probe since this behavior is highly localized and occurring over a relatively short time span. If one did wish to probe this mechanism, we would recommend repeatedly imaging the sample while under no bias and applying PCA to the imaged results. We attempted this with

another sample, but trends in collection are extremely weak when compared to imaging noise.

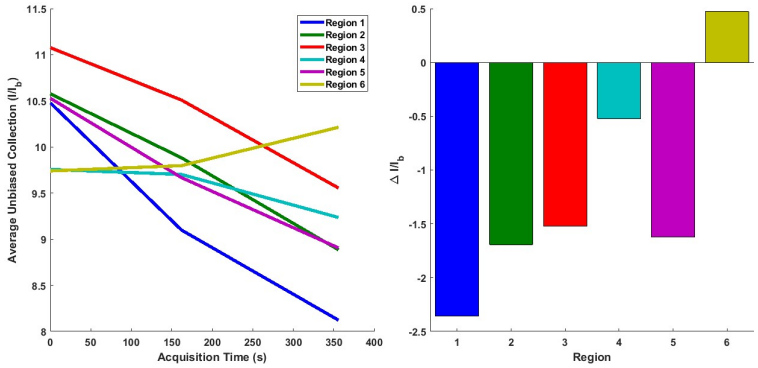

Figure 5.6 Effect of beam damage on unbiased collection efficiencies for each pre-defined region. The left plot shows the average collected values while the right plot shows the net change in each region.

CHAPTER 6
LINE PROFILE INJECTION DEPENDENCE

6.1 Introduction

A concern of existing EBIC evaluation techniques lies in injection dependence. Under ideal circumstances the collected current in an EBIC image should be proportional to the carriers generated by the Beam Current. However this assumption is not valid for many thin film devices imaged in cross section. This injection dependence may be caused by the screening of local electric fields or surface recombination effects as well as the imaging condition, but artifacts created in this way should be addressed to decrease interpretation ambiguity of EBIC analysis. In this chapter we address two previously-established methods which aim to address these artifacts through the evaluation of changes in line profiles as a function of imaging conditions. We discuss limitations of each technique while providing experimental evidence of advantages gained through this technique.

6.2 Accelerating Voltage Variation

Next consider the application of injection dependent EBIC. Injection is a parameter which is easily varied, requires no additional equipment, and is unaffected by device area. Previous studies have varied injection through the change in accelerating voltage[21, 39, 40]. This variable changes scattering probabilities of beam electrons while the sample. Figure 6.1 demonstrates how beam voltage changes the carrier excitation volume in a device. This figure uses the program CASINO to simulate electron scattering in a CdTe device in a non-deterministic matter. From this figure we see that increased beam voltage shifts the average carrier generation position further away from the incident surface. Previous publications have assumed low injection conditions and uniform composition to use variation in carrier excitation to draw conclusions as to surface recombination velocity. Unfortunately, this injection variation method has no viable method of quantification. This is because a measured collection current is equal to the probability of collecting carriers generated at any point in the generated volume multiplied by the generation rate at that point. A variation in beam voltage changes the sampled volume as well as the probability of collecting carriers generated from a given point. Even if one were to assume that the sample volume completely homogeneous, a variation of beam voltage changes the lateral resolution of the collection map which makes collection map comparison very difficult if not impossible to quantify. The problem with these changes are exacerbated when imaging a poly-crystalline material such as CdTe as seen in Figure 6.2.

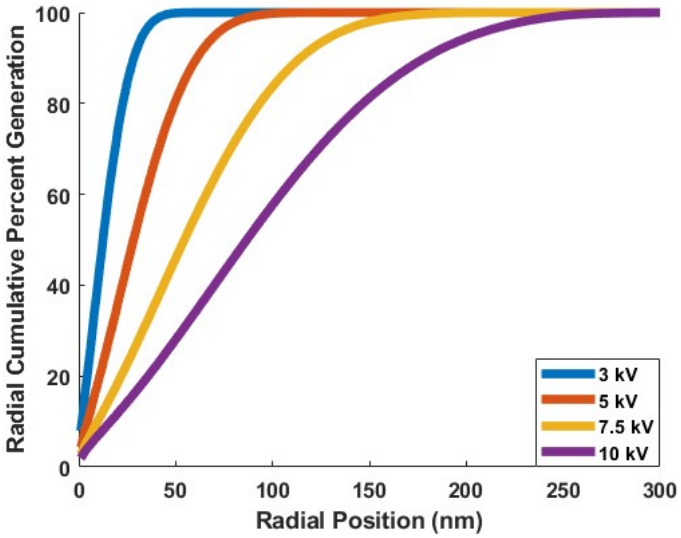

Figure 6.1 Simulated carrier scattering in CdTe as a function of beam voltage. Each line represents the lateral resolution of a given beam current through the cumulative radial energy deposition. Simulations were conducted using CASINO with 1 million simulated electron trajectories per beam setting and with the electrons interacting with a uniform CdTe volume

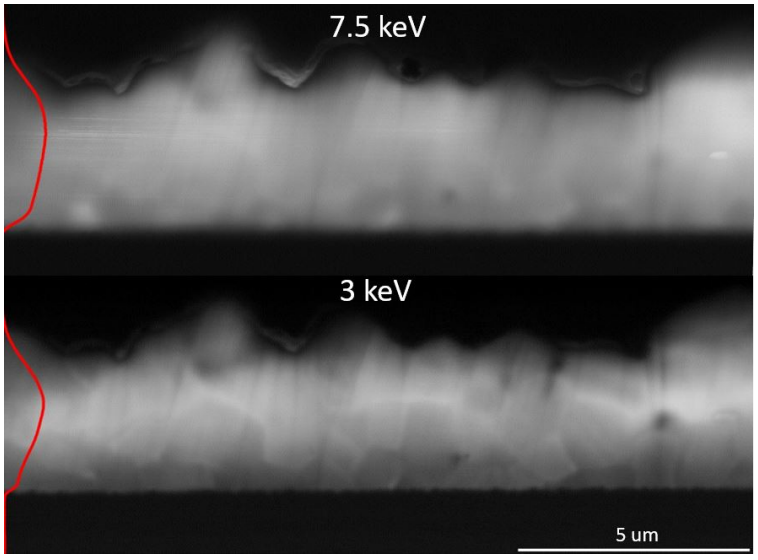

Figure 6.2 A demonstration of the decrease in lateral image resolution as a function of beam voltage. While there are changes to the average line profile seen in the left of both images, changes in lateral resolution cannot be isolated from changes in injection conditions.

6.3 Beam Current Variation

In contrast to beam voltage variation, beam current does not greatly change the generation volume of a sample. Instead beam current primarily changes the concentration of carriers at all points within the generation volume. This is because the scattering probabilities of electrons interacting with atoms in the sample only encounter a slight change due to variable valence states as the beam current is increased while beam voltage affects both interaction probabilities, and scattering trajectories.

Under high injection conditions, we expect changes in photo-current to result from changes in the effective screened radius of the high injection region as well as beam damage to the sample. According to two previous studies by the same group, [44, 45], the location of maximum collection should be at a point where the high injection region ceases to include the depletion region, and may be a quantifiable measure for the technique. This relation is best expressed in equation 6.1. [44]

$$x_0^{max} = x_{junction} + x_w + R^* = \kappa_1 + R^* \tag{6.1}$$

Where R^* is the radius of the metallic sphere approximation. We use κ to represent a change in reference frame which simplifies the equation while highlighting variable dependencies. We then use equation 6.2 to create a simplified approximation of the relationship between the screened radius and the generation rate. In this equation $\chi = \frac{R^*}{L_D}$ scales the screened radius with respect to the diffusion length and $L_R = \frac{L_D}{L}$ scales the diffusion length with respect to the device width. The approximation of equation 6.2 is reasonable since most well designed devices contain diffusion lengths which are greater than the device thickness. Under these conditions, $L_R > 1$ and so the other component of the function $(1 - L_R\chi)^{-1}$ should diverge before $\frac{sinh(\chi)}{\chi}$ represents a 17 percent change in the relationship between generation and screened radius.

$$G = G_{crit} * \frac{sinh(\chi)}{\chi(1 - L_R\chi)} \approx \frac{G_{crit}}{1 - \frac{R^*}{L}} \tag{6.2}$$

As a variation of beam current does not affect fundamental global device variables, such as active dopant concentrations, one may reasonable assume that the critical generation rate is constant for all injection variable images. We also know that the generated carriers are proportional to the beam current through equation 6.3[44].

$$G = 0.8 * \frac{V_{beam}}{3 * E_{gap}} I_{beam}(e^-/s) = \kappa_2 * I_{beam}(Amps) \tag{6.3}$$

In equation 6.3, the 0.8 coefficient accounts for the typical backscatter probability estimate and the factor of 3 incorporates other energy loss mechanisms. We again use κ to visually simplify the equation and in doing so highlight the proportionality between injected current and generation. Then we can use equation 6.3 to rewrite equation 6.1 as equation 6.4 where I_{crit} is the beam current which would yield the critical generation rate.

$$x_0^{max} = \kappa_1 + L\left(1 - \frac{I_{crit}}{I_{beam}}\right) \tag{6.4}$$

Where $I_{crit} = \frac{G_{crit}}{\kappa_2}$ is the beam current required to enter low injection conditions. I_{crit} implicitly includes factors related the backscatter coefficient, material band gap, and loss mechanisms associated with imaging a sample which may not be known in the context of the imaging process. From this equation we see that there exists an inverse relationship between the maximum collection point and beam current and that the peak position asymptotically approaches L at high beam current values. This provides an equation which should allow us to fit the evolution of collection peak as a function of beam voltage. Unfortunately, previous experimental studies have shown poor fitting results when applied to a 3D CdTe devices[44, 45].

We may also use Haney's high injection construction to qualitatively evaluate samples which do not contain the ideality required for quantification. In this context, the difference in collection at the same point with two different beam currents is proportional to the change in the potential difference across the surface of the conductive sphere as a function of screened radius. Note that electric field is not as relevant as potential drop across the surface of the sphere since this construction avoids assuming that the potential is continuously decreasing as one moves from the junction to the back contact. Avoiding this assumption allows for known device characteristics such as conduction pathways. This qualitative construction suggests that regions demonstrating high collection variability possess a large change in potential difference across the surface of the screened region while regions with small changes in collection efficiency have small changes in that same potential difference.

6.4 Injection Dependent Line Profile Evolution

We used two devices which had been used in the KPFM study [7]. This study probed the source of metastability in bilayer CdSeTe/CdTe devices grown at Colorado State University. From this study, KPFM results showed electric field peaks at the front contact, approximately 0.75um away from the front contact, and near the back contact. From this, the study obtained qualitative simulated agreement by allowing for charge accumulation at the front contact as well as a 0.1eV barrier at the back contact. Because the potential benefits as well as complexity of bilayer CdSeTe/CdTe devices, it is highly likely that further characterization will be required to optimize growth conditions.

In order to improve and simplify future characterization of this process, we performed injection-dependent EBIC characterization of the same devices used in the published study. We believed that the device structure would make traditional EBIC interpretation impossible, but evaluating the injection dependent line-profile evolution may provide a cheap and fast way to better understand the electrical properties of the device in an unbiased state. We varied beam current between 3e-11 and 1.21e-9 in a series of 6 images.

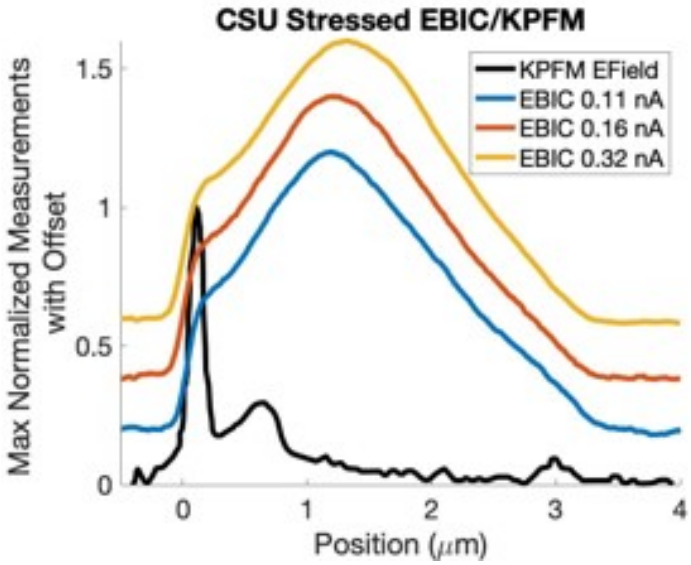

Figure 6.3 Evolution of injection dependent EBIC compared with the KPFM electric field measurements. EBIC measurements were taken with a 5kV beam voltage while KPFM measurements were taken with a sample bias of -1.5V. The peak collection position demonstrates changes consistent with imaging under high injection conditions. Under these conditions, we expect that reductions in beam current would lead the peak collection to asymptotically approach the peak field position.

First we compared an injection dependent series of three collection line profiles across the same region as KPFM was performed. This comparison is highlighted in figure 6.3 with all measurements being normalized to their maximum value and a vertical offset allowing for greater comparison. Traditional EBIC interpretation of any single one of these line profiles may suggest that the high collection near the center of the absorber indicates large carrier separation and thus a large field near that collection peak. In contrast the injection dependent measurements for even this small range of variation shows a shifting peak position which instead suggests the location of maximal electric field strength is closer to the front contact than the collection peak of the smallest beam current setting. Because of the surface passivation required for KPFM measurements prevented this region of interest from being imaged at lower beam current settings. This is because the oxide passivation layer acts as a barrier to the electron beam, reducing the effective generation rate and thus the noise level.

Next we prepared the other cleaved side of the same device for the purpose of EBIC imaging. As it is the same device, we expected a similar electric field distribution, however in this case we were able to maintain reasonable signal-to-noise ratios while imaging with beam currents as low as 0.03 nA. Results of this study are shown in figure 6.4. Figure 6.4 demonstrates a clear increase in collection efficiency with reduced beam current as well as a shift in peak collection towards the front contact with reduced current. Both of these features qualitatively agree with previous publications regarding injection dependent EBIC.

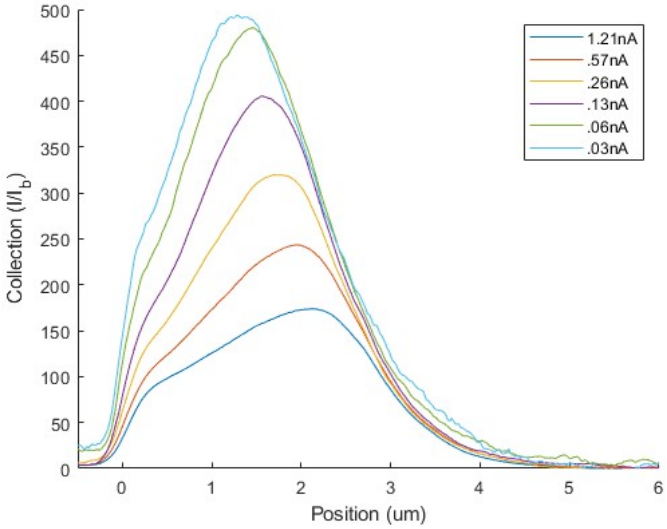

Figure 6.4 Line Profile Evolution of average collection with respect to beam current. This evolution shows an increase in collection efficiency as well as a shift in maximum electron collection as beam current is reduced. The x-axis origin is the start of the CdTe layer, as determined by the secondary electron image.

6.5 Results

Because quantitative analysis described previously in this chapter focused on changes in the collection peak position, we next plot that measurement against beam current in figure 6.5. In this figure, we include the position of the first and last pixel which demonstrate collection greater that 99 percent of the peak collection and treat these as functional error bars. Results show that the collection peak asymptotically approaches a position of 2um into the absorber as injection current increases. These results suggest that the We include a range of the first and last pixel to contain a collection current greater than 99 percent of the peak collection current for each beam current value. These results disagree with equation 6.4, however the KPFM results provide a valid explanation for the disagreement in the form of non-uniform potential changes. The derivation of equation 6.4 contains an assumption that the potential drops linearly across the device while KPFM results show that this is not true. However with this information, we may generalize

our expectations and interpretation of injection dependent EBIC using equation 6.5.

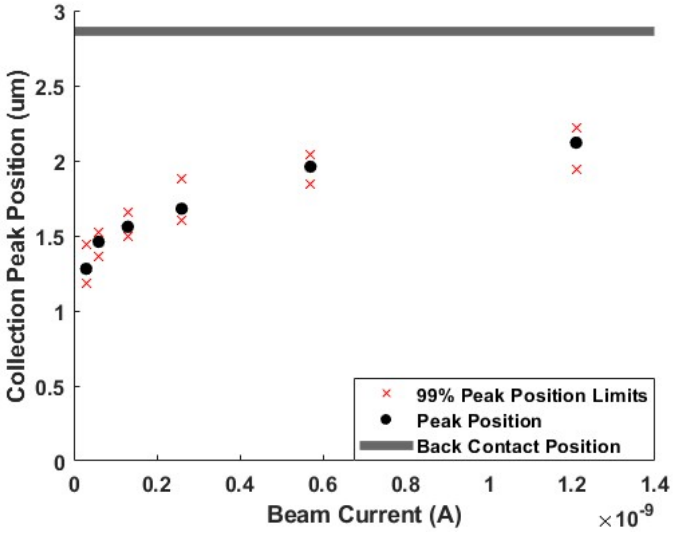

Figure 6.5 Collection peak position evolution as a function of beam current. Based on the assumption of previous publications, we expect the peak to asymptotically approach the back contact with increases to the beam current.

$$J_{ph} = \mu N_a \int \left(\vec{E} \cdot \hat{x} \right) dydz \tag{6.5}$$

The greatest interpretation guideline for high injection EBIC is that the collection peak asymptotically approaches the local minima of the potential. This is because the decrease in collection efficiency is dependent on the potential drop across the surface of the screened region.

From the first interpretation guideline, we may draw the following corollary: high injection collection peaks settle in potential minima. As the screened region increases with greater generation, the potential drop across a region with a local minima does not change at the same rate as those which don't screen the minima. In a 1D case, this may result in a net increase in collection efficiency as we completely screen a trap, however in 2 or 3D cases in which the minima is caused by features such as grain boundaries or charged back contacts, the minima region may continue to be in contact with the surface of the spherical screening region which results in little net change to collection efficiency.

These two guidelines explain the "bright" grain boundaries seen in the EBIC imaging of thin film devices. So long as the generation is enough to screen local fields from a grain interior, the collection peak will present itself at a local minima such as those seen in grain boundaries. This is a simple explanation for the disconnect between grain boundary performance and EBIC characterization of the same grain boundaries.

Also these guidelines provide a method with which to expand injection-dependent EBIC interpretation. Figure 6.5 shows peak position asymptotically approaching a position of 2um. Interpreting this to be caused by an effective reverse diode at the back contact, this characterization method identifies the local minima of a device region in an unbiased state. This does not quantitatively agree with KPFM results, however we attribute this to either changes caused by the KPFM surface passivation process or the reverse bias under which the work function was measured.

Another branch of understanding this method uncovers is the ability to qualitatively probe electric field strengths in an unbiased sample condition with 2D image resolution. Chapter 9 focuses on demonstrating this approach using PCA in order to identify regions with similar electric field strengths.

Finally we must address the sensitivity of this approach to surface recombination effects. Because the cleaved surface of most samples have a high surface energy due to numerous dangling bonds which are not representative of the devices' bulk properties. Because the electric field of the unpacified surface should be orthogonal to the $\hat{x}$ direction, we refer to equation 6.5 to hypothesize that this electric field should not affect the asymptotic behavior of the photocurrent. Haney et al. have published one paper which addresses the impact that imaging surface conditions may have on EBIC results[52]. That work suggests that improper sample preparation through post-cleave annealing or FIB-based sample preparation may create a secondary junction which would change EBIC results but that surface recombination primarily affects collection efficiency, not collection peak position. Further development of this technique should focus on addressing the role of imaging surface recombination on critical generation and the asymptotic behavior of similarly imaged devices.

6.6 Conclusion

In this chapter we evaluated the injection dependence of CdTe measurement as it compares to KPFM measurements. We established that devices with buried junctions demonstrate an expected level of injection dependence and that we were unable to reach quantification without the ability to image under low injection conditions and that asymptotic behavior of our results did not align with predictions of previous high injection conditions. This deviation could be consistent with a back contact barrier to collection which is typical for the imaged devices. This appears to be a source of information which, though too immature for quantification, may still be able to reduce interpretation ambiguity of EBIC imaging of thin film devices at no extra cost to the tool owner.

CHAPTER 7

2D PCA-ENHANCED EBIC ANALYSIS CDSE/CDTE

7.1 Introduction

Given that variations in beam current may result in changes to EBIC contrast, we next attempted to identify trends in this contrast through PCA. PCA should be able to identify trends in how contrast changes with beam current, and we expect this change to be indicative of the electric field gradient at the edge of the screened region following equation 7.1.

$$J_{ph} =_a \cdot \hat{x} dy dz \tag{7.1}$$

From this equation, we see that the change in the photocurrent as a function of distance from the junction is proportional to the electric field strength in that direction. Under high injection conditions, changes in potential are screened in a spherical volume around the beam position. Therefore, the change in collection as a function of beam current is proportional to the net change in potential at the edge of the sphere.

If our hypothesis is correct, PCA should identify discrete regions of the sample which are in the presence of a similarly changing electric field. Limitations of this approach come from low sampling rates as, unlike chapter 5, signal strength may only be feasible for approximately 5 conditions instead of 20.

7.2 CdSe/CdTe device

The first device we attempted to characterize using injection-dependent EBIC analysis was a MZO/CdS/CdTe device grown by research partners at the University of Toledo. This was part of a series to evaluate $CdCl_2$ anneal temperatures for their growth processes. Secondary Electron Imaging of our region of interest in figure 7.1 shows several grain boundaries, but no lateral mid-absorber grain boundary which is more typical of bilayer CdSeTe/CdTe devices. However, because of the triple point seen in figure 7.2, we decided to conduct an injection dependent EBIC study to better understand the role microstructure plays in the collection of large-grain polycrystalline CdSeTe devices.

The collection map seen in figure 7.2 shows the collection of the same area. From this we observe high collection near the front contact with a relatively ideal decrease in collection efficiency as the beam moves further from the pn junction. While there is collection variation which correlates with grain position seen in figure 7.1, there is collection on both sides of the grain boundary and the boundary does not appear to affect the entire imaged region.

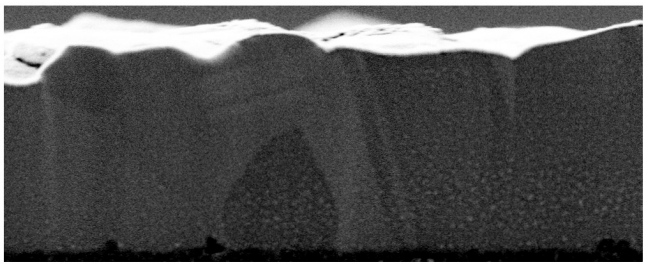

Figure 7.1 Secondary electron image of the region of interest

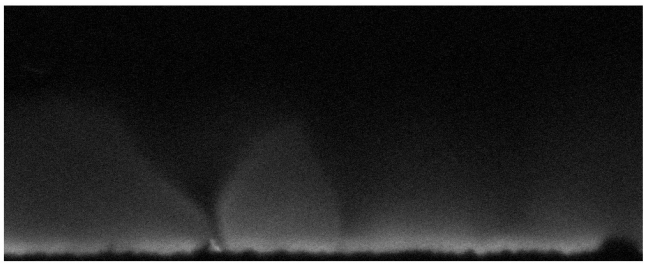

Figure 7.2 EBIC Collection Map of the Region of interest.

Figure 7.3 shows the average collection as a function of beam position relative to the TCO layer and is plotted for several beam currents between 0.1 and 8.1 nA. Collection rates are normalized to the beam currents to generate a number which is proportional to collection efficiency. From this, we observe an inverse relationship between collection efficiency and beam current, however without large shifts in collection peak position this is difficult to quantify using line profile analysis of chapter 7.

Instead of evaluating variations in line profile we followed the same PCA procedure as with voltage biased EBIC in order to spatially resolve modes of change in the collection efficiency as a function of beam current. Similar to the voltage dependent PCA procedure, we align each image, normalize collection with respect to injection, subtract the average collection rates from each pixel, and then apply PCA to identify modes of change in our data set. Results from this process are seen in figure 7.4.

Once PCA was completed, we first tried to interpret the first two eigenimages, or modes of change, seen in Figure 7.4. Eigenimage 1 shows an image similar to the average collection rate and the coefficient plot primarily serves to highlight a decrease in collection efficiency with increased collection. Eigenimage 2 shows an inverse relationship between collection near the front contact and collection near the grain boundary. The rapidly non-linear changes seen in the scatter plots are symptomatic of a complex system with relatively few data points. Despite this, there appear to be large trends in the first two eigenimages,

so we continued with the procedure established in previous chapters to use a density map of eigenvector values in order to identify distinct populations, or regions, of pixels.

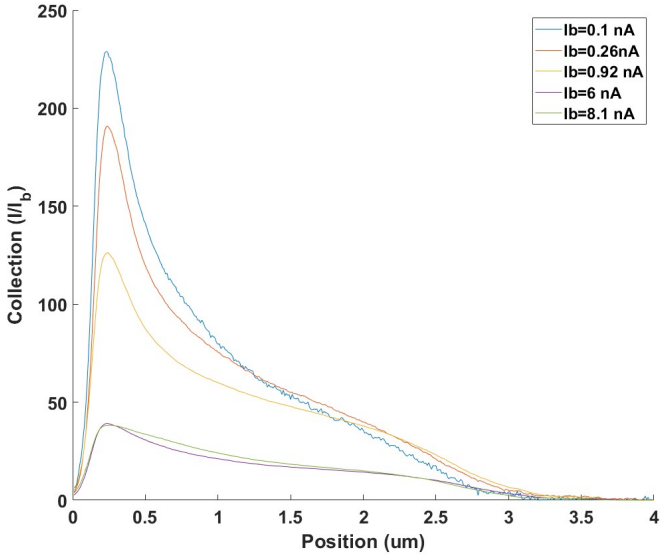

Figure 7.3 Evolution of average collection vs position from the junction as a function of injection. Decreased collection efficiency is expected as the internal fields are screened, however this sample does not show the same shifting maximum collection position as we saw in chapter 6.

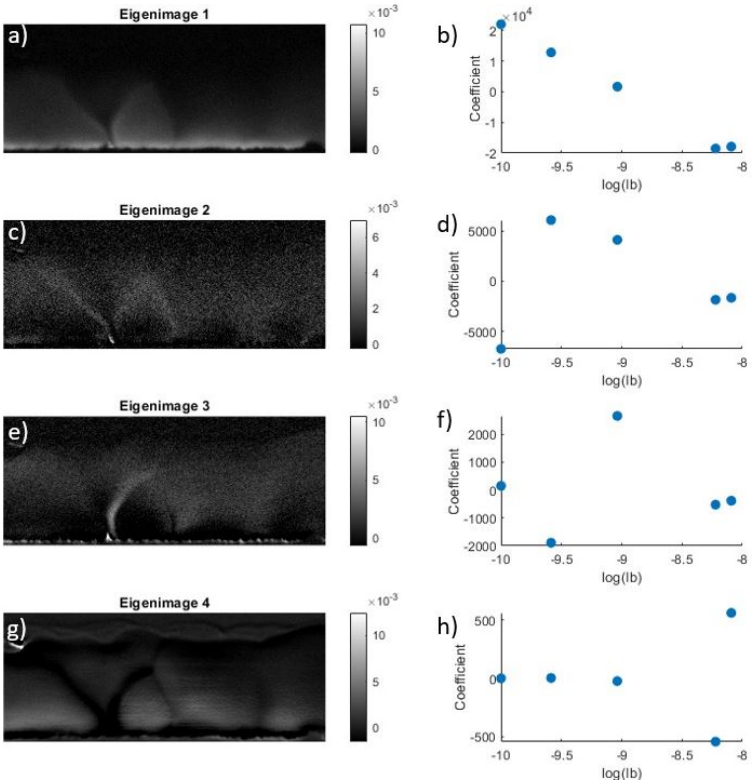

Figure 7.4 Eigenvectors, F(x_b), and coefficients, G(I_b), for the first 4 modes of change in the injection series. This shows strong contrast near the grain boundary which is visible in the secondary electron image of figure 7.1. The first mode shows average change in collection across the device while other modes show deviations to this change.

Results of this procedure, shown in figures 7.5-7.7, identified three regions with distinct behavior. Each region was identified using eigenvalue correlations in figure 7.5. Lines were created to represent the core of each region and each pixel with an region specific eigenvector cutoff distance from these cores were included as part of the region. Then the spatial positions of each region were overlaid on an EBIC image in Figure 7.6. This overlay demonstrated very little spatial mixing between the regions which supported their treatment as distinct populations. Figure 7.7 shows that each region also demonstrates an unambiguously unique response to changes in beam voltage, as 1 σ error bars contained no overlap.

With these populations established, we were able to then work to interpret them. Comparison of Figure 7.6 to 7.1 shows that region 1 primarily correlates to the rastered beam position being off the sample, either past the back contact or still on the glass substrate. This region was therefore identified as a control where the generation was 0. This interpretation is supported by a lack of collection seen in the region in figure 7.7. As was previously established, the rate of change in collection is related to the change in electric field across the surface of our spherical construction. The application of that understanding applied to the

results of figure 7.7 suggests that carriers generated in region 3 experience a greater electric field than those in region 2. This interpretation agrees with conventional knowledge regarding the spatial location of these two groups [29], since region 2 largely exists far into the quasi-neutral region while region 3 strongly correlates with the regions of maximum collection. One unexpected element of this analysis is that there exists a population of generation positions which belong to Region 2 yet seem to appear between Region 3 and the TCO. Furthermore, this population is continuous, even encompassing the portion of the absorber adjacent to an inclusion near the contact on the right side of the image.

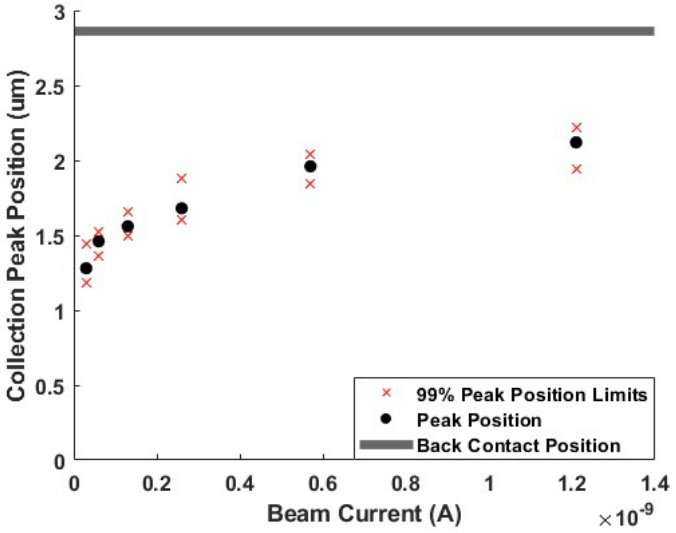

Figure 7.5 Three regions identified from changes in collection contrast with respect to injection. These regions are superimposed on a density map correlating the first two eigenimages. Intensity is placed on a logarithmic scale.

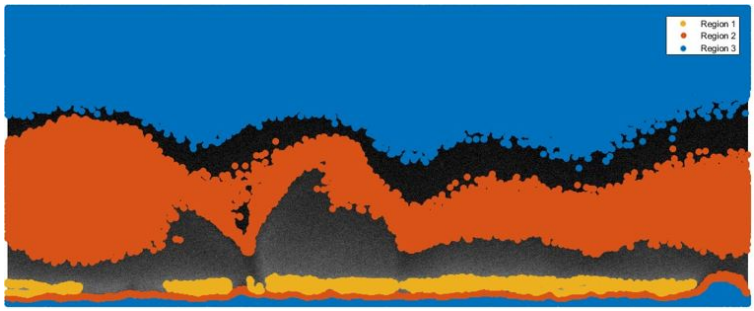

Figure 7.6 The spatial positions of 3 PCA-identified regions overlayed onto the EBIC collection map seen in Figure 7.2. These regions are spatially isolated which supports the selection criteria of Figure 7.5.

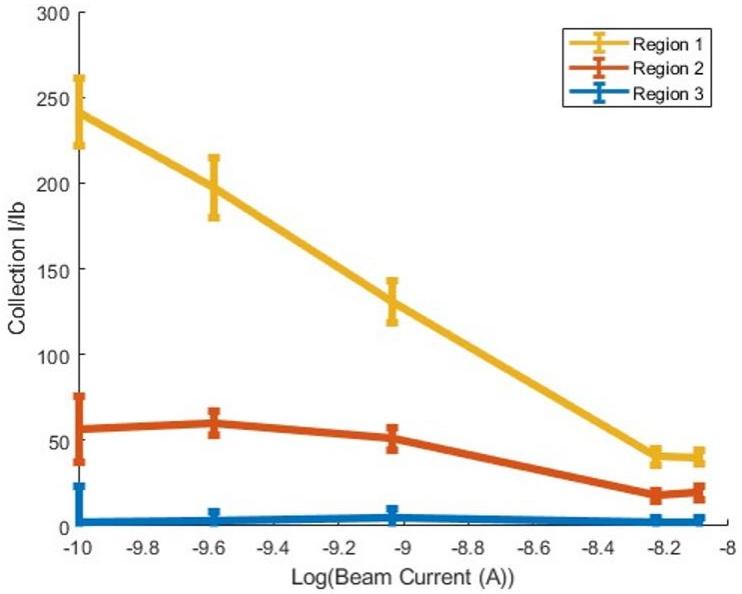

Figure 7.7 Average collection efficiency in each region as a function of beam current. From this, we can see large variation in the collection in region 3, lower collection variation in region 2, and no discern-able change in collection for region 1. Region 1 appears to represent pixels where the electron beam was not in contact with the absorber, which acts as a proof of the null hypothesis. Region 1 appears near the low beam current collection peak and is presumed to be at or near the junction. Most of the pixels representing region 2 are deep in the absorber and appear to be strongly influenced by the presence of a grain boundary. There is also a population of pixels in region 2 which appear beneath pixels of region 1 and may indicate a barrier to collection near the front contact.

This subset of region 2 near the TCO could be indicative of a key barrier to collection, which is normally observed less directly, however it could also be associated with the Se concentration gradient. We hoped to gain greater insight into the interpretation of region 2. With these three groups identified, we next tried to refine the analysis by correlating eigenvectors 3 and 4. Because there was less distinction between groups than the groups selected from region 7.5, we chose circular regions of 5 groups and plotted them in addition to the previously defined region 1. The results of this are seen in figure 7.8. Figure 7.8b shows the identification of 5 circular regions in the eigenvector 3-4 correlation plot. All generation points within the circular outlines are considered part of each region, and the regions are contrasted with similar correlations of region 1. As region 1 was defined using correlations in eigenvector 3 and 4, the population is less well defined in this new basis. The spatial overlay seen in 7.8a shows less spatial isolation between groups which is matched by the low differentiation of collection behavior seen in figure 7.8c. One new group which does differentiate itself both spatially and through its collection behavior is region 7. Region 7 shows a relatively high collection efficiency with a large change in collection with increased beam current. Based on figures 7.1 and 7.2, region 7 correlates to grain interiors, but provides clear separation between the grain interior and boundary. This separation between the regimes of a grain boundary and grain

interior is typically difficult to identify through a single EBIC image as collection follows a continuous trend and the range of impact of a grain boundary on collection depends on a number of factors[34, 62]. Regions 5 and 8 appear to subdivide region 3 seen in figure 7.6 with their division primarily defined by the location of the absorber. Near the back contact, region 5 directly correlates to populations of beam positions off the absorber while region 8 correlates to beam positions on the absorber. Both regions correlate to negligible collection in the line profiles of Figure 7.3, yet this technique is able to differentiate the negligible collection of region 8 from the noise-level collection of region 5.

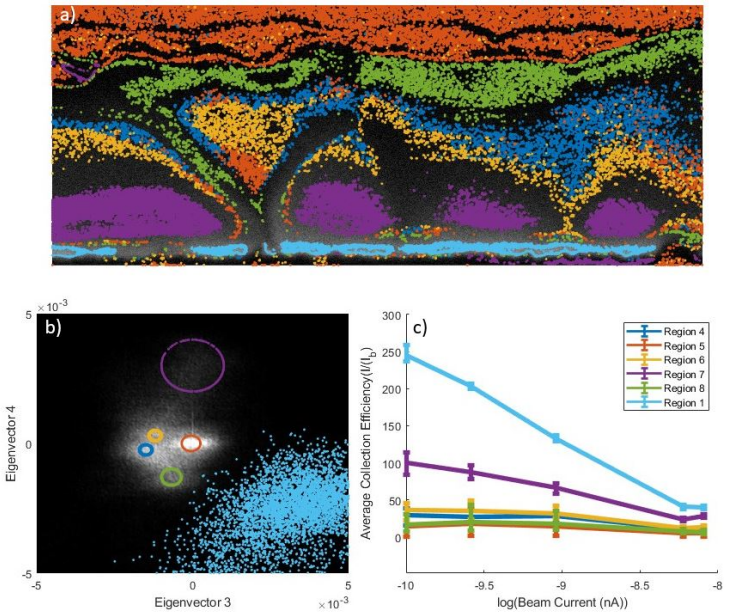

Figure 7.8 This process uses higher order eigenvectors to identify populations which exhibit similar responses to varying injection. (a) shows the spatial location of each pixel which was found through the eigenvector correlation plot seen in (b). The response of each population to varied beam current is then shown in figure (c) with 1 σ bars included. Five regions were identified using correlations between eigenvector 3 and 4. These five regions were contrasted with the previously defined region 1 from figure 7.6.

The differentiation of these regions yields fascinating results near the triple point on the left side of the image. Based on our results, the asymmetry of region 5 in the central grain is indicative of an asymmetry in the role that the two grain boundaries play in collection. This is further emphasized by the left grain boundary being represented by region 8 while the right grain boundary does not belong to any PCA-defined groups. We know that this sample was from an experiment designed to optimize $CdCl_2$ treatment for this growth process. Because of that, we believe that region 8 may indicate high concentrations of $CdCl_2$ and are waiting for Cl results to verify this interpretation. Regardless, the correlation of these regions with the proximity to a grain boundary strongly supports the interpretation in which these grain boundaries are detrimental to collection within the imaged device [34, 62].

7.3 Conclusion

We have successfully identified discrete regions of the sample which have collection efficiencies similarly affected by changes in imaging beam current using PCA. These regions may be further subdivided through the use of additional basis elements, increasing the image gained from a series of EBIC images. This process differentiated regions of the image where the beam was not incident to the absorber from regions of the image where the beam was incident to the absorber but which demonstrated otherwise negligible collection efficiency. This is a direct evidence of reductions in collection ambiguity through this method using pattern correlations of only 5 images.

CHAPTER 8

2D PCA-ENHANCED ANALYSIS OF BILAYER CDSETE DEVICES

8.1 Introduction

Finally 2D PCA enhanced analysis was applied to an injection dependent EBIC data set to better understand bilayer CdSeTe/CdTe devices. This device architecture offers greater experimental control over growth conditions when compared to CdSe/CdTe devices, yet record efficiency CdSeTe devices have come from the latter structure [63]. We chose a series of bilayer MZO/CdSeTe/CdTe devices where the composition of the CdSeTe layer of the absorber was systematically changed between 0 and 40 percent Se to try to understand the impact Se content has on collection rates of bilayer devices. Figure 8.1 shows the average collection efficiency across the device with the MZO/CdSeTe interface being located at x=0 and the CdSeTe layer thickness being nominally 1.5um. From this figure, we see the collection profile exhibits a local maxima, or peak collection efficiency, which appears to move from the MZO/CdSeTe interface to the CdSeTe/CdTe interface as selenium concentration was increased. Figure 8.2 shows the images from which collection was averaged to make Figure 8.1. These images showed that the changing collection peak position was correlated with increased contrast across a large lateral grain boundary in the center of the absorber.

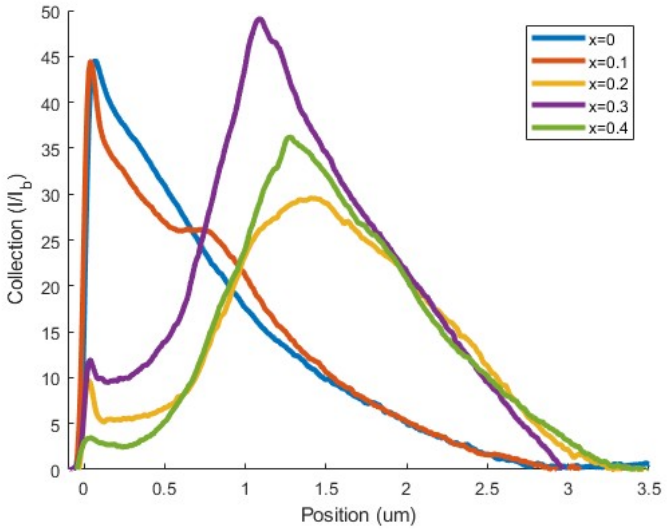

Figure 8.1 Line profile evolution of $CdSe_xTe_{1-x}$ as a function of Se content. Data was collected at 5kV beam voltage with beam currents of 0.43 $\pm$ 0.03 nA.

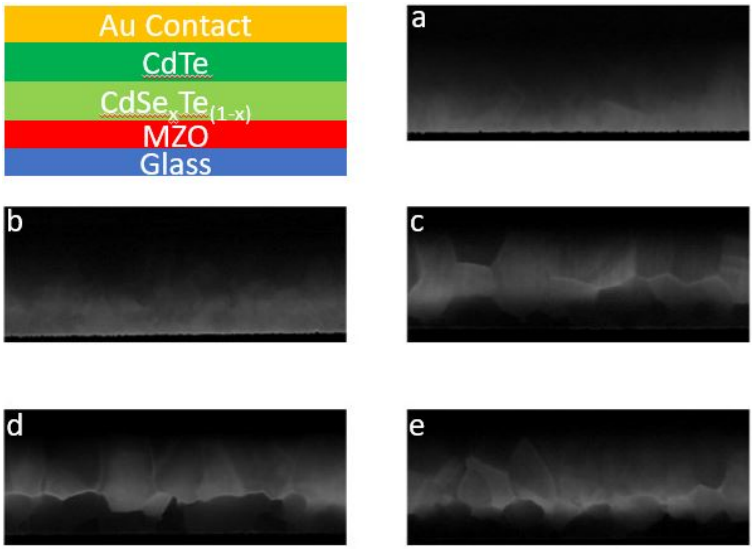

Figure 8.2 Effect of Se content on EBIC contrast for devices with the illustrated bilayer structure. The five samples contain 0 (a), 10 (b), 20 (c), 30 (d), and 40(e) percent selenium in each image. Images were collected with electron beam currents of 0.43 ± 0.03 nA and accelerating voltages of 5kV

8.2 Experiment

The correlation between the increase in mid-absorber grain contrast and the shift of the mid-absorber peak suggests that the two features are related much like the second simulation in chapter 4. In this interpretation the grain boundary caused band-bending which created a transistor-like behavior in the middle of the absorber, thus decreasing collection efficiency in the CdSeTe layer. With this interpretation, the strength of band bending was dependent on the selenium content.

To test this interpretation, we conducted an injection dependent EBIC study on the sample with greatest contrast between layers. This sample was bilayer $MZO/CdSe_{0.4}Te_{0.6}/CdTe$ with nominal layer thicknesses of 10nm, 1.5um, and 1.5um, respectively. Growth processes match those detailed in a prior publication [4].

Injection dependent EBIC procedures matched those of previous chapter: following image acquisition images were aligned, cropped, and normalized before PCA was applied to the data set. Figures 8.3 and 8.4 show the initial results of this region. While EBIC contrast appeared to be strongly dependent on microstructure, the beam current dependencies were not. Irrespective of grain boundary position, the first two eigenvectors identified two distinct regions with a small gap between them. Region two demonstrates high collection efficiency as well as a large change in collection over time while region one demonstrates consistently low collection efficiencies[here].

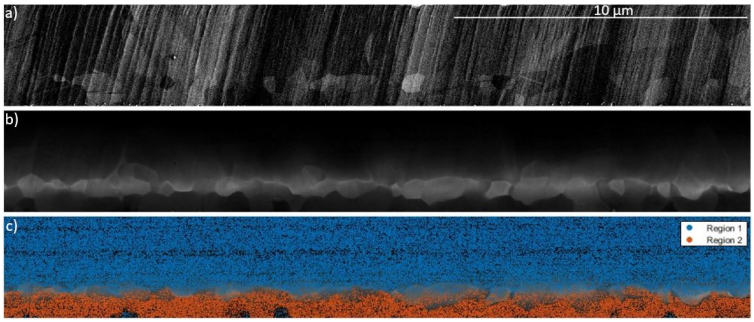

Figure 8.3 Comparison of the Secondary Electron (a), EBIC (b), and PCA identified region representations (c) of the region of interest. This demonstrates a region of interest with some curtaining, an atypical collection map with microstructure dependencies, and two identified regions of pixels obtained using PCA.

The average response of region 2 seen in 8.4c did not appear to reflect the two populations of grains seen in the associated regions of figure 8.3b. Because of this discrepancy we were concerned that the results may have been affected by noise, especially since we only had a 4 image data-set. We tried expanding to higher eigenimages to observe other dependencies much like chapter 7. We also attempted noise reduction techniques such as the application of a 2D median filter and 2D wavelet denoising algorithm, with similarly little effect. Despite this, we still failed to correlate the microstructure-based EBIC results with the microstructural correlations seen in individual EBIC images such as 8.3b.

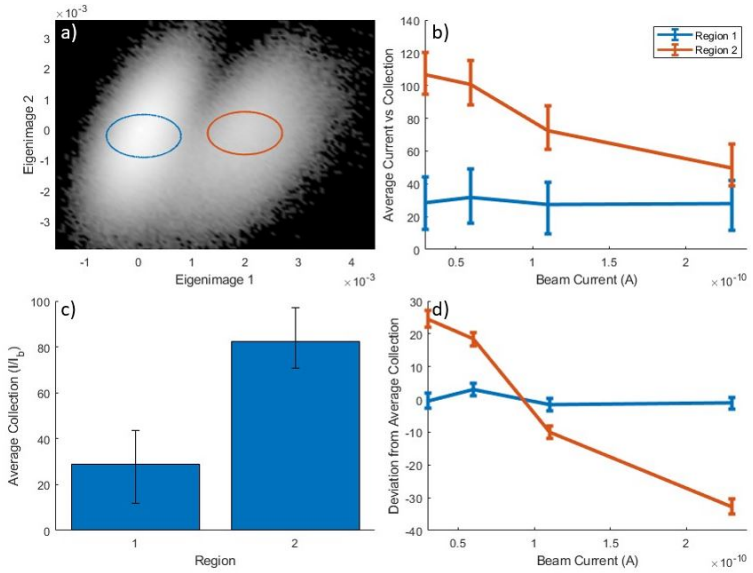

Figure 8.4 Differentiating factors of the first two regions. The regions were first identified using the density map in (a). From there we can show their change in collection as a function of beam current (b) which can be further divided into a difference in average collection across all beam currents (c), and the deviations with respect to that average threshold (d). 1 standard deviation error bars are included in figures b-d.

Our next step was to instead create additional data for PCA to deconstruct in addition to our experimental data. On one hand, an increased data set allows for an increased number of basis vectors which may provide higher sensitivity to changes in collection. On the other hand the expansion of data-set must be done carefully; the addition of pure noise may obfuscate any collection trends while simply duplicating images will result in the additional eigenimages to be empty as no additional information has been added to the data set. As we wanted to understand the relationship between microstructure and collection dependence, we chose to add 4 additional "uniform" images. The collection of each pixel in a "uniform" image was equal to the average collection of all pixels in one of the original EBIC images. This process pushes the algorithm to treat local variation in collection and change in average collection as different features, while expanding the basis to 8 eigenimages. Because trends are calculated using a complete basis, the addition of "uniform" images to the analyzed data set will not result in any loss of fidelity.

Figure 8.5 shows the results of this approach in a manner which can be directly contrasted with Figure 8.3. Figure 8.5 shows 5 distinct regions with high spatial correlation. Comparing figure 8.5c with figures 8.5 a and b, we see that the identified regions closely mirror grain boundaries and sources of collection contrast in individual EBIC images. For instance, the border between regions 6 and 7 closely mirrors a lateral grain boundary seen in the SE image of 8.5a. Figure 8.6c shows that this regional identification

draws a distinction between areas which otherwise demonstrate similar collection efficiencies, such as regions 5 and 6. The distinction between regions 5 and 6 is especially interesting as figure 8.5c shows that they are adjacent and within the same lateral grain structure. figure 8.6b better elucidates the difference in regions as both regions 6 and 7 demonstrate a much greater dependency on injection conditions than regions 4 and 5.

Based on this deconstruction and the discussion of injection dependent imaging of chapter 6, it is apparent that the grain boundary which separates regions 6 and 7 and which appears to cause a significant change in collection efficiency does not result in a large change in injection dependence when compared to the otherwise invisible feature which divides region 5 and 6. From the discussion of chapter 6, its likely that the electric field strength of regions 6 and 7 are significantly higher than those of regions 3-5.

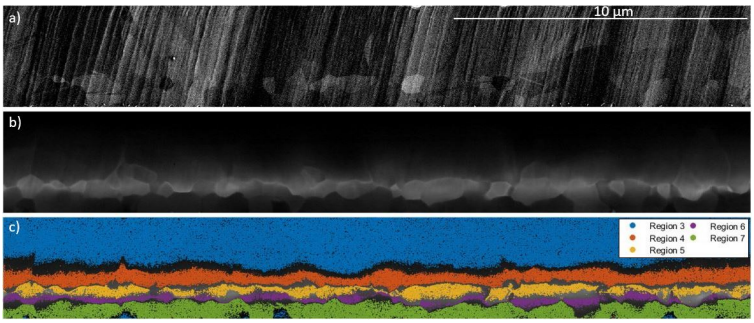

Figure 8.5 Comparison of the Secondary Electron (a), EBIC (b), and PCA identified regional representations (c) of the region of interest.

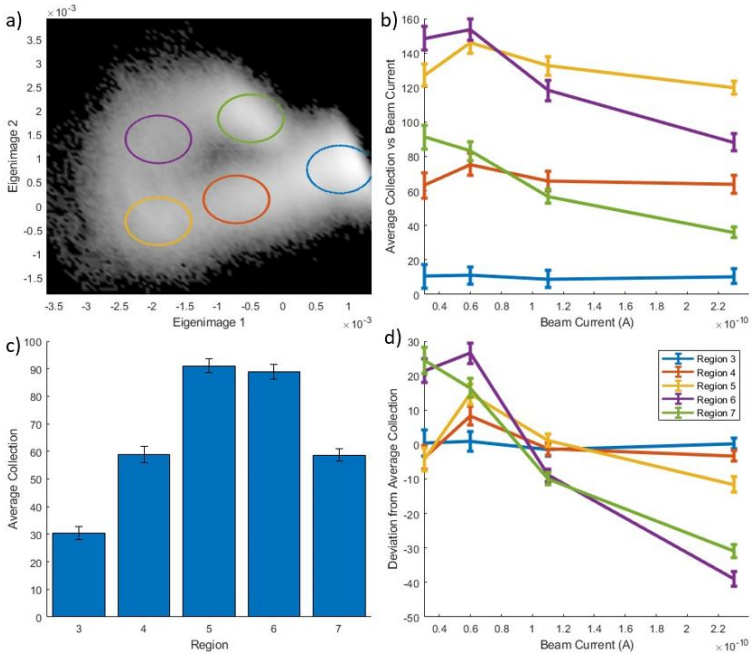

Figure 8.6 Deconstruction of 5 identified regions using the modified PCA procedure. The regions were identified through high density regions outlined in the eigenvector correlation density map of (a). From there we show their change in collection as a function of beam current (b) which can be further divided into a difference in average collection across all beam currents (c), and the deviations with respect to that average threshold (d). 1 standard deviation error bars are included in figures b-d.

To better understand the source of this division between regions with high injection dependence and low injection dependence, a correlative study between Scanning Transmission Microscope-based Energy Dispersive Spectroscopy (STEM-EDS) and EBIC analysis of a bilayer $CdSe_{0.3}Te_{0.7}/CdTe$ grown under the same conditions as part of the same dataset as the previous sample. The results of this correlation, presented in figure 8.7, show that the peak collection position is not fixed but its measurements strongly correlate with the Selenium gradient between both absorber layers. These results are consistent with previously published band structures of bilayer devices in which it was stated that the selenium content resulted in both an electron affinity gradient and a band gap gradient across the device which caused greater electric fields in the CdSeTe region when compared to the CdTe region of the same absorber [4, 7].

8.3 Conclusion

Modifying the previously established PCA procedures [64] allowed for the decoupling of EBIC injection response to beam current changes and the average EBIC collection across all beam current values. This process highlighted that the dominant changes in collection were not associated with average collection or location relative to microstructure, but instead with the selenium gradient.

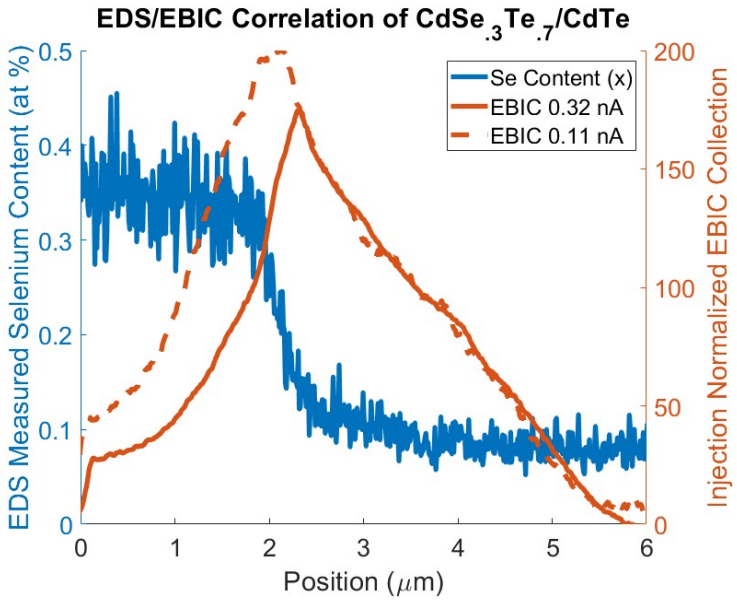

Figure 8.7 Correlation between STEM-EDS measurements. From this, we see strong correlation between the EBIC peak-position and the EDS selenium gradient.

From these results, it is likely that the source of decreased EBIC collection in the CdSeTe layer is caused by imaging CdSeTe under the high injection regime. The abrupt transition from region 5 to region 6 suggests that the onset of high injection may be correlated with the selenium composition gradient. There are three key methods by which the creation of a selenium-induced band gap gradient may affect injection conditions: band gap decrease, space charge region expansion, and lifetime increases. First, Selenium is known to reduce the band gap of CdTe with from 1.5eV to 1.41eV with a 35% occupancy of Te sites [3]. This 6% reduction in band-gap may result in a proportional increase to carriers generated with the same beam current. More importantly, the band gap gradient may create a p-i-n junction in which the built-in potential is dispersed over a larger area than an abrupt junction[7]. As the critical generation relates the carrier generation rate to a devices' ability to disperse charge carriers, p-i-n junctions have lower local electric fields than abrupt p-n junctions with the same built-in potential. Therefore, the critical generation rate may be decreased through the creation of a p-i-n junction. Finally we know that the accumulation of charge carriers is proportional to the lifetime of those carriers. Zheng et al showed through both spectral CL and TRPL that $CdSe_{0.08}Te_{0.92}$ demonstrated greater minority carrier lifetimes than CdTe while attributing this to the passivation of bulk defects [4]. This feature may further exacerbate the impact of Se on EBIC characterization

Because EBIC characterization images at generation rates several orders of magnitude greater than the those of a photovoltaic device under standard operations, the impact of decreases to critical generation to

device performance has not yet been found for CdSeTe devices. This work demonstrates how new analysis methods to a small 4 image data set reduces ambiguity in EBIC characterization as to the role that the lateral grain boundary microstructure plays on device performance.

CHAPTER 9

CONCLUSION

This dissertation focuses on how to gain the most information from an EBIC experiment and its methodologies should be widely applicable. The techniques described may be applied to any cross correlation technique, but the most surprising result is how much information it provides when comparing a single technique under multiple imaging conditions. This process allows for a more robust characterization interpretation at no additional operational cost outside of the time required to collect more images. We chose to focus on EBIC characterization of II-VI polycrystalline thin film photovoltaic devices since it a well established technique which has traditionally shown difficulty providing readily interpret-able data on the subject devices.

We first validated the application of this technique to voltage biased EBIC characterization by using both an ideal and non-ideal 1D simulations. Through these simulations we demonstrated some of the effects grain boundaries may cause on local voltage response and how PCA may be used to better understand this process. We established that injection condition may not be uniform within a polycrystalline device and that bias may result in a shifting buried junction position.

Then we applied the technique to voltage biased EBIC results of a small area device. Through this we were able to identify sample regions which experienced systematic changes in collection with respect to applied voltage while also quantifying these voltage responses. We continued this investigation to experimentally demonstrate a lack of correlation between the voltage response and short circuit collection efficiency of each of the regions of the absorber. We contrast these results with previous EBIC studies and demonstrate the advantage that a large data set and PCA bring with respect to interpretation ambiguity. While this lack of correlation has been previously simulated, this is the first time these results have been experimentally demonstrated.

Next we applied a previously established high-injection framework to complex CdSeTe/CdTe devices. We demonstrated that the process can reduce ambiguity in line profile evaluation and help identify potential minima locations within a thin film device. We also showed that line-profile evaluation of injection dependent EBIC is limited, and not a good technique to cross correlate with KPFM. Quantification limitations arise from our inability to reach low-injection conditions in any observed bilayer CdSeTe/CdTe devices. Cross correlation difficulties arise both from the difference in sample preparation requirements as well as the difference in imaging voltage bias requirements of the two techniques.

After this we applied PCA to an injection dependent EBIC image series of a MZO/CdSe/CdTe device. Using only 5 beam current values, we identified 8 populations of generation positions in the data set which show distinct injection dependent collection efficiencies. This process demonstrated that the technique may be applied to 2D images of an injection dependent series and provides additional information as to the source of EBIC contrast with even a small data set.

Finally we applied the technique of PCA enhanced Injection Dependent EBIC to a bilayer MZO/CdSeTe/CdTe device which showed unusual collection behavior. We found that artificially inflating the data set allowed for average changes in collection to be decoupled from the average collection. From this we were able to conclude that the primary source of the irregular collection was most likely imaging under high injection conditions, and that the critical generation is strongly dependent on selenium content in the bilayer devices.

Each of these studies were designed to gain greater insight into EBIC analysis techniques as they apply to CdSeTe devices. The techniques contrast with existing literature both in terms of approach and results. We demonstrate methods to evaluate collection maps in a more statistically robust method than what has been used in previous publication. Our results decrease ambiguity with regards to the source of collection contrast and our techniques were chosen to minimize experimental cost and time.

We recommend three directions for future work in this area: PCA development, combined bias EBIC, and cross correlation. The application of PCA to EBIC may be improved upon through the use of robust PCA. This technique allows for the creation of a sparse matrix in addition to standard eigenvectors [**?**]. Initial results suggest that this process enables the technique to be more robust to noise and may enable the digital removal of systematic "streaking" noise we have seen in low signal EBIC applications [65]. Another path of future research, the combined bias approach to EBIC, would attempt to use a reverse bias applied across device contacts to change EBIC injection conditions in accordance to equation 3.14. Finally we would recommend using spectral CL in a cross-correlation study with injection-dependent EBIC in order to better understand the populations identified by PCA.

REFERENCES

[1] Igor Sankin and Dmitry Krasikov. Kinetic Simulations of Cu Doping in Chlorinated CdSeTe PV Absorbers. *physica status solidi (a)*, 216(15):1800887, 2019. ISSN 1862-6319. doi: https://doi.org/10.1002/pssa.201800887. URL https://onlinelibrary.wiley.com/doi/abs/10.1002/pssa.201800887. _eprint: https://onlinelibrary.wiley.com/doi/pdf/10.1002/pssa.201800887.

[2] Naba Raj Paudel, Chuanxiao Xiao, and Yanfa Yan. CdS/CdTe thin-film solar cells with Cu-free transition metal oxide/Au back contacts. *Progress in Photovoltaics: Research and Applications*, 23(4): 437–442, 2015. ISSN 1099-159X. doi: 10.1002/pip.2446. URL https://onlinelibrary.wiley.com/doi/abs/10.1002/pip.2446. _eprint: https://onlinelibrary.wiley.com/doi/pdf/10.1002/pip.2446.

[3] Drew E. Swanson, James R. Sites, and Walajabad S. Sampath. Co-sublimation of CdSexTe1x layers for CdTe solar cells. *Solar Energy Materials and Solar Cells*, 159:389–394, January 2017. ISSN 0927-0248. doi: 10.1016/j.solmat.2016.09.025. URL https://www.sciencedirect.com/science/article/pii/S0927024816303634.

[4] X. Zheng, D. Kuciauskas, J. Moseley, E. Colegrove, D. S. Albin, H. Moutinho, J. N. Duenow, T. Ablekim, S. P. Harvey, A. Ferguson, and W. K. Metzger. Recombination and bandgap engineering in CdSeTe/CdTe solar cells. *APL Materials*, 7(7):071112, July 2019. doi: 10.1063/1.5098459. URL https://aip.scitation.org/doi/full/10.1063/1.5098459. Publisher: American Institute of Physics.

[5] Alexandra M. Bothwell, Jennifer A. Drayton, Pascal Jundt, and James R. Sites. CdMgTe as an Electron Reflector for MgZnO/CdSeTe/CdTe Solar Cells. In *2019 IEEE 46th Photovoltaic Specialists Conference (PVSC)*, pages 0149–0154, June 2019. doi: 10.1109/PVSC40753.2019.8980651. ISSN: 0160-8371.

[6] Tursun Ablekim, Craig Perkins, Xin Zheng, Carey Reich, Drew Swanson, Eric Colegrove, Joel N. Duenow, David Albin, Sanjini Nanayakkara, Matthew O. Reese, Tushar Shimpi, Walajabad Sampath, and Wyatt K. Metzger. Tailoring MgZnO/CdSeTe Interfaces for Photovoltaics. *IEEE Journal of Photovoltaics*, 9(3):888–892, May 2019. ISSN 2156-3403. doi: 10.1109/JPHOTOV.2018.2877982. Conference Name: IEEE Journal of Photovoltaics.

[7] C. S. Jiang, D. Albin, M. Nardone, K. J. Howard, A. Danielson, A. Munshi, T. Shimpi, C. Xiao, H. R. Moutinho, M. M. Al-Jassim, G. Teeter, and W. Sampath. Electrical potential investigation of reversible metastability and irreversible degradation of CdTe solar cells. *Solar Energy Materials and Solar Cells*, 238:111610, May 2022. ISSN 0927-0248. doi: 10.1016/j.solmat.2022.111610. URL https://www.sciencedirect.com/science/article/pii/S0927024822000344.

[8] Naba Paudel, Jonathan Poplawsky, Karren Moore, and Yanfa Yan. Current Enhancement of CdTe-Based Solar Cells. *Photovoltaics, IEEE Journal of*, 5:1492–1496, September 2015. doi: 10.1109/JPHOTOV.2015.2458040.

[9] X. Zheng, E. Colegrove, J. N. Duenow, J. Moseley, and W. K. Metzger. Roles of bandgrading, lifetime, band alignment, and carrier concentration in high-efficiency CdSeTe solar cells. *Journal of Applied Physics*, 128(5):053102, August 2020. ISSN 0021-8979. doi: 10.1063/5.0013726. URL https://aip.scitation.org/doi/10.1063/5.0013726. Publisher: American Institute of Physics.

[10] Jonathan D. Poplawsky, Chen Li, Naba R. Paudel, Wei Guo, Yanfa Yan, and Stephen J. Pennycook. Nanoscale doping profiles within CdTe grain boundaries and at the CdS/CdTe interface revealed by atom probe tomography and STEM EBIC. *Solar Energy Materials and Solar Cells*, 150:95–101, June 2016. ISSN 0927-0248. doi: 10.1016/j.solmat.2016.02.004. URL https://www.sciencedirect.com/science/article/pii/S0927024816000660.

[11] James E. Moore, Sourabh Dongaonkar, Raghu Vamsi Krishna Chavali, Muhammad Ashraful Alam, and Mark S. Lundstrom. Correlation of Built-In Potential and I–V Crossover in Thin-Film Solar Cells. *IEEE Journal of Photovoltaics*, 4(4):1138–1148, July 2014. ISSN 2156-3403. doi: 10.1109/JPHOTOV.2014.2316364. Conference Name: IEEE Journal of Photovoltaics.

[12] J. R. Sites. Characterization and Analysis of CIGS and CdTE Solar Cells: December 2004 - July 2008. Technical Report NREL/SR-520-44811, 947438, January 2009. URL http://www.osti.gov/servlets/purl/947438-xm3JLs/.

[13] Darius Kuciauskas, Jian V. Li, Ana Kanevce, Harvey Guthrey, Miguel Contreras, Joel Pankow, Pat Dippo, and Kannan Ramanathan. Charge-carrier dynamics in polycrystalline thin-film CuIn1xGaxSe2 photovoltaic devices after pulsed laser excitation: Interface and space-charge region analysis. *Journal of Applied Physics*, 117(18):185102, May 2015. ISSN 0021-8979. doi: 10.1063/1.4921011. URL http://aip.scitation.org/doi/full/10.1063/1.4921011. Publisher: American Institute of Physics.

[14] Darius Kuciauskas, Joel N. Duenow, Ana Kanevce, Jian V. Li, Matthew R. Young, Pat Dippo, and Dean H. Levi. Optical-fiber-based, time-resolved photoluminescence spectrometer for thin-film absorber characterization and analysis of TRPL data for CdS/CdTe interface. In *2012 38th IEEE Photovoltaic Specialists Conference*, pages 001721–001726, June 2012. doi: 10.1109/PVSC.2012.6317927. ISSN: 0160-8371.

[15] Jason M. Kephart, Anna Kindvall, Desiree Williams, Darius Kuciauskas, Pat Dippo, Amit Munshi, and W. S. Sampath. Sputter-Deposited Oxides for Interface Passivation of CdTe Photovoltaics. *IEEE Journal of Photovoltaics*, 8(2):587–593, March 2018. ISSN 2156-3403. doi: 10.1109/JPHOTOV.2017.2787021. Conference Name: IEEE Journal of Photovoltaics.

[16] Steve Johnston, Katherine Zaunbrecher, Richard Ahrenkiel, Darius Kuciauskas, David Albin, and Wyatt Metzger. Simultaneous Measurement of Minority-Carrier Lifetime in Single-Crystal CdTe Using Three Transient Decay Techniques. *IEEE Journal of Photovoltaics*, 4(5):1295–1300, September 2014. ISSN 2156-3403. doi: 10.1109/JPHOTOV.2014.2339491. Conference Name: IEEE Journal of Photovoltaics.

[17] J. M. Burst, J. N. Duenow, D. S. Albin, E. Colegrove, M. O. Reese, J. A. Aguiar, C.-S. Jiang, M. K. Patel, M. M. Al-Jassim, D. Kuciauskas, S. Swain, T. Ablekim, K. G. Lynn, and W. K. Metzger. CdTe solar cells with open-circuit voltage breaking the 1 V barrier. *Nature Energy*, 1(3):1–8, February 2016. ISSN 2058-7546. doi: 10.1038/nenergy.2016.15. URL https://www.nature.com/articles/nenergy201615. Number: 3 Publisher: Nature Publishing Group.

[18] Xun Li, Kai Shen, Qiang Li, Yi Deng, Peng Zhu, and Deliang Wang. Roll-over behavior in current-voltage curve introduced by an energy barrier at the front contact in thin film CdTe solar cell. *Solar Energy*, 165:27–34, May 2018. doi: 10.1016/j.solener.2018.02.075.

[19] S. H. Demtsu and J. R. Sites. Effect of back-contact barrier on thin-film CdTe solar cells. *Thin Solid Films*, 510(1):320–324, July 2006. ISSN 0040-6090. doi: 10.1016/j.tsf.2006.01.004. URL https://www.sciencedirect.com/science/article/pii/S0040609006000472.

[20] Jonathan D. Poplawsky, Wei Guo, Naba Paudel, Amy Ng, Karren More, Donovan Leonard, and Yanfa Yan. Structural and compositional dependence of the CdTexSe1-x alloy layer photoactivity in CdTe-based solar cells. *Nature Communications*, 7:12537, July 2016. ISSN 2041-1723. doi: 10.1038/ncomms12537.

[21] Jonathan D. Poplawsky, Naba R. Paudel, Chen Li, Chad M. Parish, Donovan Leonard, Yanfa Yan, and Stephen J. Pennycook. Direct Imaging of Cl- and Cu-Induced Short-Circuit Efficiency Changes in CdTe Solar Cells. *Advanced Energy Materials*, 4(15):1400454, 2014. ISSN 1614-6840. doi: 10.1002/aenm.201400454. URL https://onlinelibrary.wiley.com/doi/abs/10.1002/aenm.201400454. _eprint: https://onlinelibrary.wiley.com/doi/pdf/10.1002/aenm.201400454.

[22] C. Xiao, C. Jiang, J. Moseley, J. Simon, K. Schulte, A. J. Ptak, S. Johnston, B. Gorman, M. Al-Jassim, N. M. Haegel, and H. Moutinho. Near-field transport imaging application of photovoltaic materials. In *2017 IEEE 44th Photovoltaic Specialist Conference (PVSC)*, pages 62–65, June 2017. doi: 10.1109/PVSC.2017.8366352.

[23] K. Durose, D. Boyle, A. Abken, C.j. Ottley, P. Nollet, S. Degrave, M. Burgelman, R. Wendt, J. Beier, and D. Bonnet. Key Aspects of CdTe/CdS Solar Cells. *physica status solidi (b)*, 229(2):1055–1064, 2002. ISSN 1521-3951. doi: 10.1002/1521-3951(200201)229:2⟨1055::AID-PSSB1055⟩3.0.CO;2-W. URL http://onlinelibrary.wiley.com/doi/abs/10.1002/1521-3951%28200201%29229%3A2%3C1055%3A%3AAID-PSSB1055%3E3.0.CO%3B2-W. _eprint: https://onlinelibrary.wiley.com/doi/pdf/10.1002/1521-3951%28200201%29229%3A2%3C1055%3A%3AAID-PSSB1055%3E3.0.CO%3B2-W.

[24] Amit H. Munshi, Jason M. Kephart, Ali Abbas, Adam Danielson, Guillaume Glinas, Jean-Nicolas Beaudry, Kurt L. Barth, John M. Walls, and Walajabad S. Sampath. Effect of CdCl2 passivation treatment on microstructure and performance of CdSeTe/CdTe thin-film photovoltaic devices. *Solar Energy Materials and Solar Cells*, 186:259–265, November 2018. ISSN 09270248. doi: 10.1016/j.solmat.2018.06.016. URL https://linkinghub.elsevier.com/retrieve/pii/S0927024818303039.

[25] Baptiste Gault, Ann Chiaramonti, Oana Cojocaru-Mirédin, Patrick Stender, Renelle Dubosq, Christoph Freysoldt, Surendra Kumar Makineni, Tong Li, Michael Moody, and Julie M. Cairney. Atom probe tomography. *Nature Reviews Methods Primers*, 1(1):1–30, July 2021. ISSN 2662-8449. doi: 10.1038/s43586-021-00047-w. URL https://www.nature.com/articles/s43586-021-00047-w. Number: 1 Publisher: Nature Publishing Group.

[26] Wilhelm Melitz, Jian Shen, Andrew C. Kummel, and Sangyeob Lee. Kelvin probe force microscopy and its application. *Surface Science Reports*, 66(1):1–27, January 2011. ISSN 0167-5729. doi: 10.1016/j.surfrep.2010.10.001. URL https://www.sciencedirect.com/science/article/pii/S0167572910000841.

[27] Joseph J. Kopanski. Capacitive Probe Microscopy. In *Encyclopedia of Imaging Science and Technology*. John Wiley & Sons, Ltd, 2002. ISBN 978-0-471-44339-1. doi: 10.1002/0471443395.img003. URL https://onlinelibrary.wiley.com/doi/abs/10.1002/0471443395.img003. _eprint: https://onlinelibrary.wiley.com/doi/pdf/10.1002/0471443395.img003.

[28] C. S. Jiang, J. Moseley, C. Xiao, S. Harvey, S. Farrell, E. Colegrove, W. K. Metzger, and M. M. Al-Jassim. Imaging hole-density inhomogeneity in arsenic-doped CdTe thin films by scanning capacitance microscopy. *Solar Energy Materials and Solar Cells*, 209:110468, June 2020. ISSN 0927-0248. doi: 10.1016/j.solmat.2020.110468. URL https://www.sciencedirect.com/science/article/pii/S092702482030074X.

[29] Daniel Abou-Ras and Thomas Kirchartz. Electron-Beam-Induced Current Measurements of Thin-Film Solar Cells. *ACS Applied Energy Materials*, 2(9):6127–6139, September 2019. ISSN 2574-0962, 2574-0962. doi: 10.1021/acsaem.9b01172. URL https://pubs.acs.org/doi/10.1021/acsaem.9b01172.

[30] Harvey Guthrey and John Moseley. A Review and Perspective on Cathodoluminescence Analysis of Halide Perovskites. *Advanced Energy Materials*, 10(26):1903840, 2020. ISSN 1614-6840. doi: 10.1002/aenm.201903840. URL https://onlinelibrary.wiley.com/doi/abs/10.1002/aenm.201903840. _eprint: https://onlinelibrary.wiley.com/doi/pdf/10.1002/aenm.201903840.

[31] T. Coenen and N. M. Haegel. Cathodoluminescence for the 21st century: Learning more from light. *Applied Physics Reviews*, 4(3):031103, September 2017. doi: 10.1063/1.4985767. URL https://aip.scitation.org/doi/10.1063/1.4985767. Publisher: American Institute of Physics.

[32] Harvey Guthrey, Sean Jones, John Moseley, Brian Gorman, and Mowafak Al-Jassim. Revealing micro-scale doping variations in thin-films via simultaneous luminescence and current collection measurements. In *Physics, Simulation, and Photonic Engineering of Photovoltaic Devices X*, volume 11681, pages 35–42. SPIE, March 2021. doi: 10.1117/12.2578418. URL https://www.spiedigitallibrary.org/conference-proceedings-of-spie/11681/116810E/Revealing-micro-scale-doping-variations-in-thin-films-via-simultaneous/10.1117/12.2578418.full.

[33] M. Kittler, W. Seifert, and V. Higgs. Recombination Activity of Misfit Dislocations in Silicon. *physica status solidi (a)*, 137(2):327–335, 1993. ISSN 1521-396X. doi: 10.1002/pssa.2211370206. URL http://onlinelibrary.wiley.com/doi/abs/10.1002/pssa.2211370206. _eprint: https://onlinelibrary.wiley.com/doi/pdf/10.1002/pssa.2211370206.

[34] Yu Jin and Scott T. Dunham. The Impact of Charged Grain Boundaries on CdTe Solar Cell: EBIC Measurements Not Predictive of Device Performance. *IEEE Journal of Photovoltaics*, 7(1):329–334, January 2017. ISSN 2156-3403. doi: 10.1109/JPHOTOV.2016.2631298. Conference Name: IEEE Journal of Photovoltaics.

[35] Jonathan D. Major. Grain boundaries in CdTe thin film solar cells: a review. *Semiconductor Science and Technology*, 31(9):093001, July 2016. ISSN 0268-1242. doi: 10.1088/0268-1242/31/9/093001. URL https://doi.org/10.1088/0268-1242/31/9/093001. Publisher: IOP Publishing.

[36] J. Palm. Local investigation of recombination at grain boundaries in silicon by grain boundary-electron beam induced current. *Journal of Applied Physics*, 74(2):1169–1178, July 1993. ISSN 0021-8979, 1089-7550. doi: 10.1063/1.354917. URL http://aip.scitation.org/doi/10.1063/1.354917.

[37] J.-L. Maurice and Y. Marfaing. THEORETICAL STUDY OF HIGH INJECTION EFFECTS IN EBIC MEASUREMENTS OF GRAIN BOUNDARY RECOMBINATION VELOCITY IN SILICON. *Le Journal de Physique IV*, 01(C6):C6–77–C6–82, December 1991. ISSN 1155-4339. doi: 10.1051/jp4:1991614. URL http://www.edpsciences.org/10.1051/jp4:1991614.

[38] R J Matson. Junction Electron-Beam-Induced Current Techniques for the Analysis of Photovoltaic Devices. page 8.

[39] P R Edwards, S A Galloway, and K Durose. EBIC and luminescence mapping of CdTe/CdS solar cells. *Thin Solid Films*, page 7, 2000.

[40] S.A. Galloway, P.R. Edwards, and K. Durose. Characterisation of thin film CdS/CdTe solar cells using electron and optical beam induced current. *Solar Energy Materials and Solar Cells*, 57(1):61–74, February 1999. ISSN 09270248. doi: 10.1016/S0927-0248(98)00168-8. URL https://linkinghub.elsevier.com/retrieve/pii/S0927024898001688.

[41] Abhijit S. Kale, William Nemeth, Sanjini U. Nanayakkara, Harvey Guthrey, Matthew Page, Mowafak Al-Jassim, Sumit Agarwal, and Paul Stradins. Tunneling or Pinholes: Understanding the Transport Mechanisms in SiOx Based Passivated Contacts for High-Efficiency Silicon Solar Cells. In *2018 IEEE 7th World Conference on Photovoltaic Energy Conversion (WCPEC) (A Joint Conference of 45th IEEE PVSC, 28th PVSEC & 34th EU PVSEC)*, pages 3473–3476, June 2018. doi: 10.1109/PVSC.2018.8547211. ISSN: 0160-8371.

[42] Heayoung P. Yoon, Paul M. Haney, Dmitry Ruzmetov, Hua Xu, Marina S. Leite, Behrang H. Hamadani, A. Alec Talin, and Nikolai B. Zhitenev. Local electrical characterization of cadmium telluride solar cells using low-energy electron beam. *Solar Energy Materials and Solar Cells*, 117: 499–504, October 2013. ISSN 0927-0248. doi: 10.1016/j.solmat.2013.07.024. URL https://www.sciencedirect.com/science/article/pii/S092702481300370X.

[43] D. Abou-Ras, N. Schäfer, N. Baldaz, S. Brunken, and C. Boit. Electron-beam-induced current measurements with applied bias provide insight to locally resolved acceptor concentrations at p-n junctions. *AIP Advances*, 5(7):077191, July 2015. doi: 10.1063/1.4928097. URL http://aip.scitation.org/doi/full/10.1063/1.4928097. Publisher: American Institute of Physics.

[44] Paul M. Haney, Heayoung P. Yoon, Prakash Koirala, Robert W. Collins, and Nikolai B. Zhitenev. Electron beam induced current in the high injection regime. *Nanotechnology*, 26(29):295401, July 2015. ISSN 0957-4484. doi: 10.1088/0957-4484/26/29/295401. URL https://doi.org/10.1088/0957-4484/26/29/295401. Publisher: IOP Publishing.

[45] Paul M. Haney, Heayoung P. Yoon, Prakash Koirala, Robert W. Collins, and Nikolai B. Zhitenev. Models for low energy electron beam induced current experiments in polycrystalline thin film photovoltaics. In *2015 IEEE 42nd Photovoltaic Specialist Conference (PVSC)*, pages 1–4, June 2015. doi: 10.1109/PVSC.2015.7356035.

[46] Y. Y. Loginov, P. D. Brown, and N. Thompson. A TEM study of the interaction of sub-threshold electron beam induced defects in II–VI compounds. *physica status solidi (a)*, 127(1):75–86, 1991. ISSN 1521-396X. doi: 10.1002/pssa.2211270108. URL https://onlinelibrary.wiley.com/doi/abs/10.1002/pssa.2211270108. _eprint: https://onlinelibrary.wiley.com/doi/pdf/10.1002/pssa.2211270108.

[47] Melanie Nichterwitz, Raquel Caballero, Christian A. Kaufmann, Hans-Werner Schock, and Thomas Unold. Generation-dependent charge carrier transport in Cu(In,Ga)Se $_2$ /CdS/ZnO thin-film solar-cells. *Journal of Applied Physics*, 113(4):044515, January 2013. ISSN 0021-8979, 1089-7550. doi: 10.1063/1.4788827. URL http://aip.scitation.org/doi/10.1063/1.4788827.

[48] Eran Edri, Saar Kirmayer, Sabyasachi Mukhopadhyay, Konstantin Gartsman, Gary Hodes, and David Cahen. Elucidating the charge carrier separation and working mechanism of CH3NH3PbI3xClx perovskite solar cells. *Nature Communications*, 5(1):3461, May 2014. ISSN 2041-1723. doi: 10.1038/ncomms4461. URL http://www.nature.com/articles/ncomms4461.

[49] J. R. Michael and P. G. Kotula. Low Energy Ga+ and Ar+ Ion Milling for Improved EBSD Sample Preparation. *Microscopy and Microanalysis*, 14(S2):976–977, August 2008. ISSN 1435-8115, 1431-9276. doi: 10.1017/S1431927608081294. URL https://www.cambridge.org/core/journals/microscopy-and-microanalysis/article/abs/low-energy-ga-and-ar-ion-milling-for-improved-ebsd-sample-preparation/4247F32D008FB6F7FE207ECE061B09E6. Publisher: Cambridge University Press.

[50] Jonathan Douglas Major, Leon Bowen, Robert Treharne, and Ken Durose. Assessment of photovoltaic junction position using combined focused ion beam and electron beam-induced current analysis of close space sublimation deposited CdTe solar cells. *Progress in Photovoltaics: Research and Applications*, 22(10):1096–1104, 2014. ISSN 1099-159X. doi: 10.1002/pip.2507. URL http://onlinelibrary.wiley.com/doi/abs/10.1002/pip.2507. _eprint: https://onlinelibrary.wiley.com/doi/pdf/10.1002/pip.2507.

[51] Heayoung P. Yoon, Paul M. Haney, Joshua Schumacher, Kerry Siebein, Yohan Yoon, and Nikolai B. Zhitenev. Effects of Focused-Ion-Beam Processing on Local Electrical Measurements of Inorganic Solar Cells. *Microscopy and Microanalysis*, 20(S3):544–545, August 2014. ISSN 1431-9276, 1435-8115. doi: 10.1017/S1431927614004449. URL https://www.cambridge.org/core/journals/microscopy-and-microanalysis/article/effects-of-focusedionbeam-processing-on-local-electrical-measurements-of-inorganic-solar-cells/761E8F82BF5C1B39184E1A3F6C9117E6. Publisher: Cambridge University Press.

[52] Paul M. Haney, Heayoung P. Yoon, Benoit Gaury, and Nikolai B. Zhitenev. Depletion region surface effects in electron beam induced current measurements. *Journal of Applied Physics*, 120(9):095702, September 2016. ISSN 0021-8979, 1089-7550. doi: 10.1063/1.4962016. URL http://aip.scitation.org/doi/10.1063/1.4962016.

[53] Martin A. Green. Generalized relationship between dark carrier distribution and photocarrier collection in solar cells. *Journal of Applied Physics*, 81(1):268–271, January 1997. ISSN 0021-8979, 1089-7550. doi: 10.1063/1.364108. URL http://aip.scitation.org/doi/10.1063/1.364108.

[54] C. Donolato. Evaluation of diffusion lengths and surface recombination velocities from electron beam induced current scans. *Applied Physics Letters*, 43(1):120–122, July 1983. ISSN 0003-6951, 1077-3118. doi: 10.1063/1.94139. URL http://aip.scitation.org/doi/10.1063/1.94139.

[55] K. Misiakos and F. A. Lindholm. Generalized reciprocity theorem for semiconductor devices. *Journal of Applied Physics*, 58(12):4743–4744, December 1985. ISSN 0021-8979, 1089-7550. doi: 10.1063/1.336226. URL http://aip.scitation.org/doi/10.1063/1.336226.

[56] C. Donolato. A reciprocity theorem for charge collection. *Applied Physics Letters*, 46(3):270–272, February 1985. ISSN 0003-6951, 1077-3118. doi: 10.1063/1.95654. URL http://aip.scitation.org/doi/10.1063/1.95654.

[57] C. Donolato. An alternative proof of the generalized reciprocity theorem for charge collection. *Journal of Applied Physics*, 66(9):4524–4525, November 1989. ISSN 0021-8979, 1089-7550. doi: 10.1063/1.343932. URL http://aip.scitation.org/doi/10.1063/1.343932.

[58] Uwe Rau and Rolf Brendel. The detailed balance principle and the reciprocity theorem between photocarrier collection and dark carrier distribution in solar cells. *Journal of Applied Physics*, 84(11): 6412–6418, December 1998. ISSN 0021-8979, 1089-7550. doi: 10.1063/1.368968. URL http://aip.scitation.org/doi/10.1063/1.368968.

[59] W. K. Metzger and M. Gloeckler. The impact of charged grain boundaries on thin-film solar cells and characterization. *Journal of Applied Physics*, 98(6):063701, September 2005. ISSN 0021-8979, 1089-7550. doi: 10.1063/1.2042530. URL http://aip.scitation.org/doi/10.1063/1.2042530.

[60] Daniel Abou-Ras, Norbert Schäfer, Thorsten Rissom, Madeleine N. Kelly, Jakob Haarstrich, Carsten Ronning, Gregory S. Rohrer, and Anthony D. Rollett. Grain-boundary character distribution and correlations with electrical and optoelectronic properties of CuInSe2 thin films. *Acta Materialia*, 118: 244–252, October 2016. ISSN 13596454. doi: 10.1016/j.actamat.2016.07.042. URL https://linkinghub.elsevier.com/retrieve/pii/S1359645416305511.

[61] Zhitao Wang, Zimeng Cheng, Alan E. Delahoy, and Ken K. Chin. A Study of Light-Sensitive Ideality Factor and Voltage-Dependent Carrier Collection of CdTe Solar Cells in Forward Bias. *IEEE Journal of Photovoltaics*, 3(2):843–851, April 2013. ISSN 2156-3403. doi: 10.1109/JPHOTOV.2013.2247095. Conference Name: IEEE Journal of Photovoltaics.

[62] John Moseley, Wyatt K. Metzger, Helio R. Moutinho, Naba Paudel, Harvey L. Guthrey, Yanfa Yan, Richard K. Ahrenkiel, and Mowafak M. Al-Jassim. Recombination by grain-boundary type in CdTe. *Journal of Applied Physics*, 118(2):025702, July 2015. ISSN 0021-8979. doi: 10.1063/1.4926726. URL http://aip.scitation.org/doi/full/10.1063/1.4926726. Publisher: American Institute of Physics.

[63] Tursun Ablekim, Joel N. Duenow, Xin Zheng, Helio Moutinho, John Moseley, Craig L. Perkins, Steven W. Johnston, Patrick O'Keefe, Eric Colegrove, David S. Albin, Matthew O. Reese, and Wyatt K. Metzger. Thin-Film Solar Cells with 19% Efficiency by Thermal Evaporation of CdSe and CdTe. *ACS Energy Letters*, 5(3):892–896, March 2020. ISSN 2380-8195, 2380-8195. doi: 10.1021/acsenergylett.9b02836. URL https://pubs.acs.org/doi/10.1021/acsenergylett.9b02836.

[64] *Brunton, S. L. (Steven L., and J. N. Kutz, 2019, Data-driven science and engineering: machine learning, dynamical systems, and control : Cambridge, United Kingdom;, Cambridge University Press.* .

[65] Best Research-Cell Efficiency Chart, . URL https://www.nrel.gov/pv/cell-efficiency.html.

APPENDIX A

PRINCIPAL COMPONENT ANALYSIS

One method with which to analyze data and better understand trends in collection is through principal component analysis (PCA). PCA is a linear algebra technique which identifies correlative trends in a data set.

Consider a matrix [A] with dimensions MxN. This matrix may be decomposed into matrices representing eigenvectors and eigenvalues with the following relationship:

$$\begin{bmatrix} A_{11} & \dots & A_{1N} \\ \vdots & \ddots & \vdots \\ A_{M1} & \dots & A_{MN} \end{bmatrix} = [U][S][V] \tag{A.1}$$

Where U is an MxM matrix containing eigenvectors which represent trends in the columns of matrix A, V is an MxN matrix containing eigenvectors which represent trends in the rows of matrix I, and S is a MxM diagonal matrix composed of eigenvalues which weight the normalized eigenvector matrices.

With PCA, one constructs the initial matrix such that each column of A contains the same measurement from multiple data sets and each row contains all measurements of a single dataset. By construction, PCA focuses on the eigenmatrix U which shows trends in variation of each measurement. PCA also consolidates the product of [S] and [V] into an MxN matrix of coefficients C such that a given element $C_{i,j}$ highlights the importance of variation i to dataset j.

The construction of the eigenmatrix is such that the product of the first eigenvector and the associated coefficient minimizes the residual between the matrix of images and this product. In other words the sum of the first n eigenimages, weighted by the appropriate coefficients is the optimal n rank approximation of the dataset.

A.1 Application of PCA to Images

One core principle which allows PCA to be applied to image datasets, such as EBIC images, is the principle that all digital images are matrices. Each matrix element is a single pixel value and for EBIC these values are the collected current for a given beam position.

While one could imagine stacking multiple images to create a 3D matrix of images at different imaging conditions, PCA is optimized for dealing with 2D matrices. As such, it is common practice to flatten each image, creating a row of pixel values which can then be combined into an MxN matrix where M is the number of images being compared and N is the number of pixels in each image.

Combining this construction with the prior explanation of PCA, one can arrive to the conclusion that we then compare trends in how each pixel changes with respect to imaging conditions. Therefore, it is vital to align and crop images such that each pixel represents the same measurement in each image and all pixels contain valid measurements.

Once PCA has been performed, one may reshape the eigenvectors of U back to the shape of the images being analyzed and in doing so create eigenimages. This reshaping allows for better comparison between the results and initial images.

APPENDIX B

MODEL DETAILS

Material Properties											
	Nc	Nv	Eg	epsilon	μ_e	μ_h	τ_e	τ_h	affinity	Acceptor	Donor
CdTe	8e17	1.9e19	1.5	9.4	320	40	3e-9	3e-9	3.9	1e18	0
CdS	2.2e18	1.8e19	2.4	10	100	25	1e-8	1e-13	4	0	4e14

Grain Boundary Properties				
Left Edge Position	Boundary Width	ρ	S	Defect Energy
0.85 μm	10 nm	1e11	1e-16	0

Model Properties

Properties	CdS	CdTe
Region Left Edge	0	25nm
Layer Thickness	25 nm	4 um
Donor density	1e18	0
Acceptor Density	0	4e14
N_c	2.2e18	8e17
N_v	1.8e19	1.8e19
E_{gap}	2.4	1.5
$\varepsilon/\varepsilon_0$	10	9.4
μ_e	100	320
μ_h	25	40
τ_e	1e-8	3e-9
τ_h	1e-13	3e-9
affinity	4	3.9

Properties	Grain Boundary
Defect Energy Level	0
Left edge position	0.85 um
Boundary Width	10 nm
Defect Density	1e11
Recombination Velocity	1e-16

Model Structure

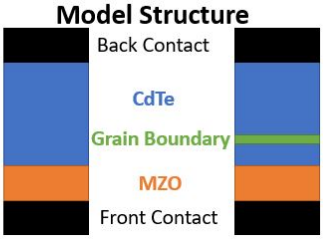

Figure B.1 Model Property Summary Page

APPENDIX C

SESAME 1D IDEALIZED SIMULATION-PYTHON

```
This code is a modification of the sesame default example 2,
downloaded from https://pages.nist.gov/sesame/

import sesame
import numpy as np
import scipy.io
from scipy.io import savemat
import matplotlib.pyplot as plt
import os
import time
GB1=0.85e-4
GB2=0.86e-4
t1 = 25*1e-7    # thickness of CdS
t2 = 4*1e-4     # thickness of CdTe
dd = 1e-7   # 2*dd is the distance over which mesh is refined
#require dense mesh near the interface

# Define the mesh
x = np.concatenate((np.linspace(0, dd, 100, endpoint=False),
                    np.linspace(dd, t1-dd, 200, endpoint=False),
                    np.linspace(t1 - dd, t1+dd,10,endpoint=False),
            np.linspace(t1+dd,GB1-dd,75,endpoint=False),
            np.linspace(GB1-dd, GB2+dd,75,endpoint=False),
            np.linspace(GB2+dd, (t1+t2) - dd,150, endpoint=False),
                    np.linspace((t1+t2) - dd, (t1+t2), 10)))

# Build system
```

```
sys = sesame.Builder(x)

# CdS material dictionary
CdS = {'Nc': 2.2e18, 'Nv':1.8e19, 'Eg':2.4, 'epsilon':10, 'Et': 0,
        'mu_e':100, 'mu_h':25, 'tau_e':1e-8, 'tau_h':1e-13,
        'affinity': 4.}
# CdTe material dictionary
CdTe = {'Nc': 8e17, 'Nv': 1.8e19, 'Eg':1.5, 'epsilon':9.4, 'Et': 0,
        'mu_e':320, 'mu_h':40, 'tau_e':3e-9, 'tau_h':3e-9,
        'affinity': 3.9}



# CdS region
CdS_region = lambda x: x<=t1
# CdTe region
CdTe_region = lambda x: x>t1

# Add the material to the system
sys.add_material(CdS, CdS_region)     # adding CdS
sys.add_material(CdTe, CdTe_region)   # adding CdTe

rho_GB = 1e11
S_GB = 1e-16
E_GB = 0

p1 = (GB1, 0)
p2 = (GB2,0)

#sys.add_defects([p1, p2],rho_GB,S_GB,E=E_GB, transition=(1,0))

#sys.add_defects([p1, p2], rho_GB, S_GB, E=E_GB, transition=(0,-1))

# Add the donors
```

```
nD = 1e18  # donor density [cm^-3]
sys.add_donor(nD, CdS_region)
# Add the acceptors
nA = 4e14  # acceptor density [cm^-3]
sys.add_acceptor(nA, CdTe_region)

# Define contacts: CdS contact is Ohmic, CdTe contact is Schottky
Lcontact_type, Rcontact_type = 'Ohmic', 'Ohmic'
Lcontact_workFcn, Rcontact_workFcn = 0, 0.0   # ohmic
# Add the contacts
sys.contact_type(Lcontact_type, Rcontact_type, Lcontact_workFcn, Rcontact_workFcn)

# Define the surface recombination velocities for electrons and holes [m/s]
Scontact = 1.16e7  # [cm/s]
# non-selective contacts
Sn_left, Sp_left, Sn_right, Sp_right = Scontact, Scontact, Scontact, Scontact
# This function specifies the simulation contact recombination velocity
sys.contact_S(Sn_left, Sp_left, Sn_right, Sp_right)
I_ramp=[18,19,20,21,22];
voltages = np.linspace(-1,1,51)
j = sesame.IVcurve(sys, voltages, 'reference',verbose=False)
j = j * sys.scaling.current;
result_a = {'v':voltages, 'j':j}
new=0;
for i in range(550,len(x)):
    print(i)
    for jj in range(len(I_ramp)):
        out_name=['1dhetero_V_test0'+str(i)+'00'+str(jj)]
        out_name2=''.join(['IV'+str(i)+'00'+str(jj)+'.mat'])
        #if new>0:
        #    sys2, result_a=sesame.load_sim(''.join(in_name))
        #    #os.system(''.join(['mv *.mat Results/']))
        #    #os.system(''.join(['mv *.gzip Results/']))
```

```
        #else:
        #    sys2, result_a=sesame.load_sim('reference_0.gzip')
        # Add illumination
        phi0 = pow(10,I_ramp[jj])     # incoming flux [1/(cm^2 sec)]
        alpha = 1   # absorbtion coefficient [1/cm]
        x0=x[i];

        f = lambda x: phi0 if x==x0 else 0
        # This function adds generation to the simulation
        sys.generation(f)

        # Specify the applied voltage values

        # Perform I-V calculation
        #j = sesame.IVcurve(sys, voltages, ''.join(out_name),guess=result_a,verbose=False)
        j = sesame.IVcurve(sys, voltages, ''.join(out_name),verbose=False)

        j = j * sys.scaling.current

        result = {'v':voltages, 'j':j}
        savemat(out_name2,result)
        #np.save(out_name2, result)
        in_name=[''.join(out_name)+'_0.gzip'];
        old_out_name=''.join(out_name);
        #del result_a, sys2, result, j
        new=1;
        #time.sleep(0.5)

# plot I-V curve
#try:
#    import matplotlib.pyplot as plt
#    #plt.plot(voltages, qqj,'-')
#    plt.plot(voltages, j,'-')
```

```
#    plt.xlabel('Voltage [V]')
#    plt.ylabel('Current [A/cm^2]')
#    plt.grid()     # add grid
#    plt.show()     # show the plot on the screen
#    plt.title('CdTe J-V curve')
# no matplotlib installed
#except ImportError:
#    print("Matplotlib not installed, can't make plot")
```

C.1 Sesame 1D Lateral Grain Boundary Simulation-Python

```
This work is a modification of the sesame default example 2,
downloaded from https://pages.nist.gov/sesame/

import sesame
import numpy as np
import scipy.io
from scipy.io import savemat
import matplotlib.pyplot as plt
import os
import time
GB1=0.85e-4
GB2=0.86e-4
t1 = 25*1e-7    # thickness of CdS
t2 = 4*1e-4     # thickness of CdTe
dd = 1e-7   # 2*dd is the distance over which mesh is refined
#require dense mesh near the interface

# Define the mesh
x = np.concatenate((np.linspace(0, dd, 100, endpoint=False),
                    np.linspace(dd, t1-dd, 200, endpoint=False),
                    np.linspace(t1 - dd, t1+dd,10,endpoint=False),
            np.linspace(t1+dd,GB1-dd,75,endpoint=False),
```

```
            np.linspace(GB1-dd, GB2+dd,75,endpoint=False),
            np.linspace(GB2+dd, (t1+t2) - dd,150, endpoint=False),
                    np.linspace((t1+t2) - dd, (t1+t2), 10)))

# Build system
sys = sesame.Builder(x)

# CdS material dictionary
CdS = {'Nc': 2.2e18, 'Nv':1.8e19, 'Eg':2.4, 'epsilon':10, 'Et': 0,
        'mu_e':100, 'mu_h':25, 'tau_e':1e-8, 'tau_h':1e-13,
        'affinity': 4.}
# CdTe material dictionary
CdTe = {'Nc': 8e17, 'Nv': 1.8e19, 'Eg':1.5, 'epsilon':9.4, 'Et': 0,
        'mu_e':320, 'mu_h':40, 'tau_e':3e-9, 'tau_h':3e-9,
        'affinity': 3.9}



# CdS region
CdS_region = lambda x: x<=t1
# CdTe region
CdTe_region = lambda x: x>t1

# Add the material to the system
sys.add_material(CdS, CdS_region)     # adding CdS
sys.add_material(CdTe, CdTe_region)     # adding CdTe

rho_GB = 1e11
S_GB = 1e-16
E_GB = 0

p1 = (GB1, 0)
p2 = (GB2,0)
```

```
sys.add_defects([p1, p2],rho_GB,S_GB,E=E_GB, transition=(1,0))

sys.add_defects([p1, p2], rho_GB, S_GB, E=E_GB, transition=(0,-1))

# Add the donors
nD = 1e18  # donor density [cm^-3]
sys.add_donor(nD, CdS_region)
# Add the acceptors
nA = 4e14  # acceptor density [cm^-3]
sys.add_acceptor(nA, CdTe_region)

# Define contacts: CdS contact is Ohmic, CdTe contact is Schottky
Lcontact_type, Rcontact_type = 'Ohmic', 'Ohmic'
Lcontact_workFcn, Rcontact_workFcn = 0, 0.0   # Ohmic
# Add the contacts
sys.contact_type(Lcontact_type, Rcontact_type, Lcontact_workFcn, Rcontact_workFcn)

# Define the surface recombination velocities for electrons and holes [m/s]
Scontact = 1.16e7  # [cm/s]
# non-selective contacts
Sn_left, Sp_left, Sn_right, Sp_right = Scontact, Scontact, Scontact, Scontact
# This function specifies the simulation contact recombination velocity
sys.contact_S(Sn_left, Sp_left, Sn_right, Sp_right)
I_ramp=[18];
voltages = np.linspace(-1,1,51)
j = sesame.IVcurve(sys, voltages, 'reference',verbose=False)
j = j * sys.scaling.current;
result_a = {'v':voltages, 'j':j}
new=0;
for i in range(len(x)):
    print(i)
    for jj in range(len(I_ramp)):
        out_name=['1dhetero_V_test0'+str(i)+'00'+str(jj)]
```

```
out_name2=''.join(['IV'+str(i)+'00'+str(jj)+'.mat'])
#if new>0:
#    sys2, result_a=sesame.load_sim(''.join(in_name))
#    #os.system(''.join(['mv *.mat Results/']))
#    #os.system(''.join(['mv *.gzip Results/']))
#else:
#    sys2, result_a=sesame.load_sim('reference_0.gzip')
# Add illumination
phi0 = pow(10,I_ramp[jj])     # incoming flux [1/(cm^2 sec)]
alpha = 1   # absorbtion coefficient [1/cm]
x0=x[i];

f = lambda x: phi0 if x==x0 else 0
# This function adds generation to the simulation
sys.generation(f)

# Specify the applied voltage values

# Perform I-V calculation
#j = sesame.IVcurve(sys, voltages, ''.join(out_name),guess=result_a,verbose=False)
j = sesame.IVcurve(sys, voltages, ''.join(out_name),verbose=False)

j = j * sys.scaling.current

result = {'v':voltages, 'j':j}
savemat(out_name2,result)
#np.save(out_name2, result)
in_name=[''.join(out_name)+'_0.gzip'];
old_out_name=''.join(out_name);
#del result_a, sys2, result, j
new=1;
#time.sleep(0.5)
```

```
# plot I-V curve
#try:
#    import matplotlib.pyplot as plt
#    #plt.plot(voltages, qqj,'-')
#    plt.plot(voltages, j,'-')
#    plt.xlabel('Voltage [V]')
#    plt.ylabel('Current [A/cm^2]')
#    plt.grid()     # add grid
#    plt.show()     # show the plot on the screen
#    plt.title('CdTe J-V curve')
# no matplotlib installed
#except ImportError:
#    print("Matplotlib not installed, can't make plot")
```

C.2 Matlab Import Code

```
%iter establishes the simulation iteration number
iter=132;
fname=['cd ../test' num2str(iter) 'd/'];
evalc(fname)
jj=1;

%identify the number of position values
for i=1:10000
try
in_name=['IV',num2str(i-1),'00',num2str(jj-1),'.mat'];
temp=load(in_name);
catch
num_xpts=i-1;
break
end
end
i=1;
```

```
%identify the number of beam current settings used in the simulation
for jj=1:10000
try
in_name=['IV',num2str(i-1),'00',num2str(jj-1),'.mat'];
temp=load(in_name);
catch
num_Ib=jj-1;
break
end
end

%currents variable creates a JV curve for a given excitation position
eval_currents=['Test' num2str(iter) 'd_Currents2{i,jj}=temp.j'];
name_currents=['Test' num2str(iter) 'd_Currents2'];
for i=1:num_xpts
for jj=1:num_Ib
in_name=['IV',num2str(i-1),'00',num2str(jj-1),'.mat'];
temp=load(in_name);
evalc(eval_currents);
end
end
temp_currents=eval(name_currents);

%map variables convert the currents variable into an EBIC map
%for each beam current (j) and voltage (k)
eval_map=['Test' num2str(iter) 'd_map2{k,j}(i)=temp_currents{i,j}(k)'];
name_map=['Test' num2str(iter) 'd_map2'];
for i=1:num_xpts
for j=1:num_Ib
for k=1:51
evalc(eval_map);
end
```

```
end
end
temp_map=evalc(name_map);
```

C.3 Matlab Analysis Code

```
%First we manually recreate the mesh position values from the python file

x=[linspace(0,1e-7,101),linspace(1e-7,24e-7,201),linspace(24e-7,26e-7,11),...
linspace(26e-7,.85e-4-1e-7,76),linspace(.85e-4-1e-7,.86e-4+1e-7,76),...
linspace(.86e-4+1e-7,4e-4+24e-7,151),linspace(4e-4+24e-7,4e-4+25e-7,201)];

%Remove overlap points caused by a lack of endpoint=False in matlab
for i=1:1000
try
if x(i)==x(i+1)
x(i+1)=[];
end
catch
break
end
end
x(end)=[];

%Next we convert the EBIC map into 100 equally spaced points.
%This prevents weighting of evaluation data
r1=linspace(min(x),max(x),101);
%clearing common variables
clear temp* y y2 big* u bb
%This example only contained one injection setting (k)
for k=1:1
for i=1:51
big_image{k}(:,i)=(Test132d_map2{i,k}-Test132d_map2{i,k}(end))./(gradient(x));
end
```

```
for i=1:51
temp=big_image{k}(:,i);
y{k}(1,i)=temp(1);
y{k}(101,i)=temp(end);
for j=2:100
a=find(abs(r1(j)-x)==min(abs(r1(j)-x)));
y{k}(j,i)=mean(temp(a-1:a+1));
end
end

%Finally we perform voltage-bias PCA analysis resulting in the position functions, u,
%the voltage function, bb, and the 101 point EBIC line profiles of the simulation,y.

y2{k}=y{k}-mean(y{k}')';
[u{k},~,~]=svd(y2{k},'econ');
for j=1:51
for i=1:51
bb{k}(i,j)=u{k}(:,j)'*y2{k}(:,i);
end
end
end
y32=y;
bb32=bb;
u32=u
```